"IONIC RADII AND MAGNETIC MOMENT DEPENDENT STRUCTURAL, MAGNETIC AND CATALYTIC PROPERTIES OF MIXED METAL OXIDE SYSTEMS"

A thesis submitted in partial fulfillment of the requirement for

The degree of ***Doctor of Philosophy*** *in the subject of* ***Chemistry***

Under the faculty of ***Science***

By

Mr. Amol Murlidhar Pachpinde

M. Sc.

Under the guidance of

Dr. K. S. Lohar

HEAD,
CHEMISTRY DEPARTMENT,
SHRIKRISHNA MAHAVIDYALAYA, GUNJOTI
TQ. OMERGA, DIST. OSMANABAD. (MS)

DR. BABASAHEB AMBEDKAR MARATHWADA UNIVERSITY,
AURANGABAD - 431 004

March -2016

Dedicated to My Parents

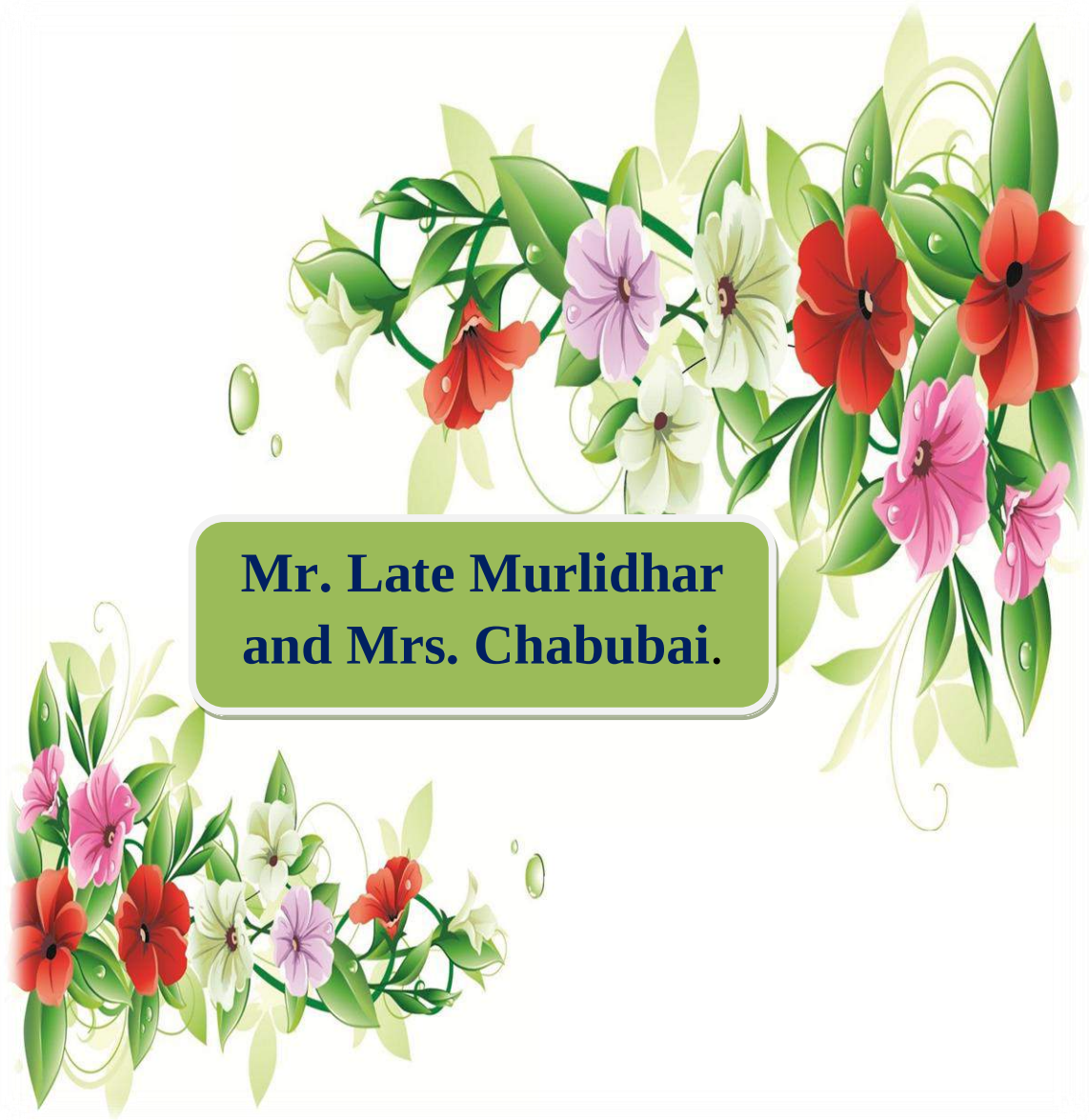

॥ न हि ज्ञानेन सदृशं पवित्रमिह विद्यते ॥
Shrikrishna Shikshan Sanstha's
Shrikrishna Mahavidyalaya,Gunjoti.
Tq.Omerga,Dist.Osmanabad 413 606
ISO 9001:2008
QMS/JAS-C2140/0536
e - mail: kslohar@rediffmail.com
dr.kslohar@gmail.com
Contact. 09421354721
Office / Fax 02475 250091
Resi. 02475 253222
Dr.K.S. Lohar
Head,Dept.Chemistry

This is to certify that work embodied in the thesis entitled, **"Ionic Radii and Magnetic Moment Dependent Structural, Magnetic and Catalytic Properties of Mixed Metal Oxide Systems",** being submitted by ***Mr. Amol Muralidhar Pachpinde*** to the Dr. Babasaheb Ambedkar Marathwada university, Aurangabad for the award of degree of Doctor of Philosophy in **Chemistry** is a record of bonafide research work carried out by his under my guidance and supervision, and has fulfilled the requirements for the submission of this thesis to my knowledge, has reached requisite standard. The results contained in this thesis have not been submitted in part or in full, to any other University or institute for the award of any degree or diploma.

Place: Aurangabad.

Date:

Research Guide

Dr. K.S.Lohar.

ABSTRACT

Nanotechnology entails the application of fields of science as diverse as surface science, organic chemistry, molecular biology, semiconductor physics, microfabrication, etc. To fabricate magnetic materials iron and its alloys were used to serve the need of the electrical industry for long time. This realization stimulated a renewed interest in "magnetic Insulators" as first reported by S. Hilpert in Germany in 1909. It was readily understood that if the high electrical resistivity of oxides could be combined with desired magnetic characteristics, a magnetic material would result that was particularly well suited for high frequency operation.

Among these magnetic materials, spinel cobalt ferrites have been intensively studied recently owing to the excellent characteristics and their potential applications such as superior chemical stability, powerful corrosion, good mechanical hardness, high level of signal to noise ratio, high resistance, microwave devices, high-density magnetic recording, electronic devices and medicine large single axis anisotropy, large coercivity and magnetic energy product and highest performance to price ratio. These materials have good mechanical, chemical and thermal stability. Rare earth substituted ferrites are nowadays under extensive investigations in order to enhance the saturation magnetization, permittivity and permeability.

The objective of this thesis is to contribute to the understanding of the correlation between the structural, morphological, infrared, magnetic properties and some catalytic applications of rare earth substituted cobalt ferrite materials. The chapter 1 deals the relevance and important concepts of nanomaterials, magnetism, ferrites which are selected for the present investigation. This Chapter reviews the basic concepts of permanent magnetic materials and importance on spinel ferrites particularly cobalt ferrite permanent magnets. It briefly presents the review of the work carried out in the field of nano ferrites, the objectives of this research work. The samples investigated in this study were obtained sol-gel auto-combustion technique. A detailed description of the

experimental methods is given in Chapter 2. This chapter introduces important aspects concerning the different synthesis methods of the nanocrystalline ferrite systems. Chapters 3 give the theoretical background of characterization techniques employed. Chapters 4 and 5 deals with the findings of the work carried out. Lastly chapter 6 deals with applications of synthesized ferrite systems as a catalyst for some chemical reactions. The following section provides a glimpse of the conclusions drawn from the present study and the scope for work.

Firstly, chapter 4 highlights the investigations on structural and magnetic properties of technologically important Ho^{3+}substituted $CoFe_2O_4$, $Ho_xCoFe_{2-x}O_4$ (x=0.0, 0.025, 0.05, 0.075, 0.1.) ferrite nanoparticles were prepared by sol-gel auto-combustion technique. The structural properties were investigated by using X-ray diffraction technique. Fourier Transform Infrared IR spectroscopy technique for the confirmation of crystal structure is outlined. Details of the imaging technique used (SEM) is also presented. Vibrating Sample Magnetometry (VSM) for the magnetic characterization of the samples has been discussed.

The different physical parameters such as lattice constants, X-ray density, cell volume, porosity, particle size were measured and show strong variation subject to Ho^{3+}substitution. It was observed that the XRD pattern of $x \geq 0.075$ sample consists of superposition of the cubic spinel and ortho-ferrite patterns indicating the two-phase coexisting region. With the addition of Ho^{3+}contents for Fe^{3+}in $Ho_xCoFe_{2-x}O_4$ compound grain size decreased with the substitution degree of Ho^{3+}. Which may be due to larger bond energy of Ho^{3+}–O^{2-} as compared to Fe^{3+}–O^{2-}, more energy is needed to force Ho^{3+}ions enter into the lattices and form the bond of Ho^{3+}–O^2 .Thus the rare earth element holmium acts as a grain growth inhibitor. The knowledge of phase formation and surface morphology was understood by scanning electron microscopy technique. It is observed from SEM that uniform distribution of particles with better grain boundaries for initial Ho^{3+} concentration. Grain size is strongly affected due to the incorporation of Ho^{3+}ions. The TEM micrograph of the synthesized Ho^{3+} substituted $CoFe_2O_4$ ferrite nanoparticles shows almost homogeneous and uniform distribution of the particles in this powder sample. The particles are consisted of some regular and irregular polyhedrons with mean sizes of about 34 nm (x= 0.0) and 41 nm(x= 0.075) much larger than the size

obtained from XRD data. The SAED patterns indicate that the samples are crystallized and their nature is polycrystalline. The Infrared spectroscopy results show the shifting of v_1 and v_2 absorption bands with Ho^{3+} substitution. The effect of rare earth element Ho^{3+}substitution on the magnetic properties of the material is in general a positive one. With the substitution of Ho^{3+}ions in $CoFe_2O_4$, saturation magnetization increased from 61.06 to74.05 emu/g, remanent magnetization increased from 28.5 to34.6 emu/g, this may be probably due to the larger magnetic moment of Ho^{3+}ions and enhanced exchange interaction. Coercivity of $CoFe_2O_4$ increased from 1269 to 1591 Oe with Ho^{3+}substitution.

In Chapter 5 the investigation of Pr^{3+} doped $CoFe_2O_4$, $Pr_xCoFe_{2-x}O_4$. (x=0.0, 0.025, 0.05, 0.075, 0.1) magnetic materials is presented. The samples were produced by sol-gel auto combustion technique. These efforts were towards synthesizing nanocrystalline rare earth Pr^{3+} doped $CoFe_2O_4$ and understanding chemistry and physics of these materials. The structural properties were investigated by using X-ray diffraction technique. The imaging technique SEM and TEM is used. Fourier Transform Infrared (FTIR) spectroscopy technique for the confirmation of crystal structure is outlined. The vibration of magnetization as a function of applied magnetic field at room temperature was studied Vibrating Sample Magnetometry (VSM).

It is observed that the increase in the Pr^{3+} content causes the change in the intensity of the XRD characteristic peaks of $Pr_xCoFe_{2-x}O_4$. (x=0.0, 0.025, 0.05, 0.075, 0.1). Lattice constant ‘a’ increased with the increase in Pr^{3+}substitution. It is observed that the cubic spinel phase coexists with some amount of $PrFeO_3$ phase in $x \geq 0.05$. As $CoFe_2O_4$ is nearly inverse spinel Pr^{3+}substitution also affects the other structural parameters such as density and porosity of $Pr_xCoFe_{2-x}O_4$ nanoparticles. Scanning electron microscopy images shows that the grain size and morphology is strongly affected due to the Pr^{3+} substitution. The SEM images of the synthesized pure cobalt ferrite and Pr^{3+}substituted cobalt ferrite, it is expected that the average grain size decreases with increase in Pr^{3+}substitution. TEM images of the samples show that the particles are aggregated and the average value of the nanocrystalline samples are is consistent with the result from XRD according to the Scherrer formula. It also demonstrates that the nanoparticles are not in spherical shape but in square slice shape with small thickness.

The selected area electronic diffraction (SAED) pattern of the nanoparticles shows poly crystalline nature. IR spectrum of the synthesized samples displayed two absorption bands characteristic of the spinel ferrites at 707–757 and 454–477 cm^{-1}. The higher frequency band (v_1) is appeared due to the stretching vibration of tetrahedral metal oxygen bond and the lower frequency band (v_2) is due to octahedral metal oxygen bond. Substitution of Pr^{3+} ions into the cobalt ferrite system can be utilized for enhancement of saturation magnetization (Ms) from 54.7emu/g to 64.2emu/g up to $x \geq 0.75$ and decrease for x=0.1. And coercive field (Hc) increases from 644 Oe to 1013 Oe. Substitution of Pr^{3+}ions in the spin-down states (4e, 4f1 and 4f2) may lead to an increase in the net magnetization. Pr^{3+}substituted cobalt ferrite samples exhibit higher coercivities than that of pure cobalt ferrite due to higher magnetocrystalline anisotropy.

Lastly in chapter 6 deals with catalytic activity of synthesized $Ho_xCoFe_{2-x}O_4$ and $Pr_xCoFe_{2-x}O_4$ nanoparticles for multi component reactions. Ho^{3+}doped $CoFe_2O_4$ nanoparticles were used for one-pot three-component synthesis of 2,4,5-triaryl-1H-imidazole derivatives from benzil or benzoin, aromatic aldehydes and ammonium acetate in ethanol. The three $Ho_xCoFe_{2-x}O_4$ (x = 0.0, 0.05, and 0.1) nanoparticles were screened to find out best ferrite composition for synthesis of 2,4,5-triphenyl-1H-imidazole as model reaction. It is observed that the reaction proceeds in shorter time period with good efficiency in the presence of $Ho_xCoFe_{2-x}O_4$(x= 0.05) nanoparticles. The catalyst was consecutively reused five times without any noticeable loss of its catalytic activity. Being a heterogeneous and highly magnetic, catalyst can be easily and almost completely separated by an external magnet which is of a great advantage. Hence the method overcomes the earlier disadvantages and therefore will be of general use and interest to synthetic chemists. Pr^{3+} doped $CoFe_2O_4$ nanoparticles were used as a catalyst for one-pot –four component synthesis of multisubstituted pyrrole derivatives via reaction of amines, aldehydes, acetylacetone and nitromethane in solvent free condition at 90 ^oC. The three $Pr_xCoFe_{2-x}O_4$ (x = 0.0, 0.05, and 0.1) nanoparticles were screened to find out best ferrite composition for synthesis of 2-methyl-1,4-diphenyl-3-acetyl-1H-pyrrole as model reaction. It is observed that the reaction proceeds in shorter time period with good efficiency in the presence of $Pr_xCoFe_{2-x}O_4$ (x= 0.05) nanoparticles. The catalyst is easily recoverable using magnet and could be reused without significant loss of catalytic

activity. Even after five runs for the reaction, the catalytic activity of Pr^{3+} doped $CoFe_2O_4$ was almost the same as that of the freshly used catalyst. The proposed method is advantageous and showing good potential for industrial application due to its little catalyst loading, short reaction time, catalyst reusability, and excellent yields.

KEYWORDS: Ferrite materials, Sol–gel growth, Electron microscopy, Infrared spectroscopy, Magnetic properties, Ho^{3+}doped $CoFe_2O_4$ nanoparticles; One-pot three-component reaction, Pr^{3+} doped $CoFe_2O_4$, Recoverable using magnet, Catalyst reusability.

DECLARATION

Ihereby declare that the work included in this thesis entitled, **"Ionic Radii and Magnetic Moment Dependent Structural, Magnetic and Catalytic Properties of Mixed Metal OxideSystems",** is carried out by meunder the guidance of **Dr. K. S. Lohar**, **AssociateProfessor and Head, ChemistryDepartment,ShrikrishnaMahavidyalaya, Gunjoti, Tq. Omerga Dist. Osmanabad.** The work is original and has notbeen submitted in part or in full to any other university or institute for award of anyresearch degree. The extent of information derived from the existing literature hasbeen indicated in the body of the thesis at appropriate places giving the references.

Place: Aurangabad
Date:

Mr. Amol M. Pachpinde

ACKNOWLEDGEMENT

Iam happy to express my deep indebtedness and gratitude to ***Dr. K. S. Lohar,****Asso.Professor and Head, Department of Chemistry, ShrikrishnaMahavidyalaya, Gunjoti Dist. Osmanabad, under whose scholarly guidance and co-operative nature, this thesis was completed. He encouraged me to do my research work and achieve the aim of my life.*

It's a very proud feeling for me to extend my gratitude to ***Hon. S. N.AlureGuruji****, Secretary of our institution whose blessings are always with me and inspired me to do my work. I am thankful to Principal* ***Dr. Anita Mudkanna*** *for providing Laboratory facilities and supported me always to finish my research work.*

I am grateful to ***Dr. D. R. Mane*** *(Director of Higher Edu.,Maharashtra),* ***Dr. Ashok Mohekar*** *(Former Dean, faculty of science),* ***Dr. S. N. Thore****(Ex Chairman, Bos, chemistry),* ***Prof. AnjaliRajbhoj,****(HOD. Chemistry, Dr. BAMU Aurangabad),* ***Prof. SureshGaikwad,Dr. Lande,Dr. Shankarwar,Dr.MazaharFarki****(Womans college, Aurangabad) and the administrative staff as well as the library section of Dr. BAMU, Aurangabad.*

I am thankful to dept. of physics, SavitribaiPhuleuniversity, Pune. IIT Mumbai, TIFR Trombay,Laxai-Avanti lab Hydrabad,for providing laboratory facility. I am very much thankful ***to Dr. SomnathAkuskar,*** *Principal ShriMadhavraoPatilMahavidhyalya, Murum,* ***Dr. SuhasPeshwe,*** *Principal ASC College, Naldurg for providing me laboratory facilities during my research work.*

I realize that no research work is possible without the collective endeavor. So it's my moral duty to express my gratitude to ***Dr.Shirsath S. E,*** *whose encouragement and co-operation cannot be expressed in words. I specially express my deep gratitude to* ***Dr. JaiprakashSangshetti****, for his valuable guidance and cooperation during research work.I am very much thankful to head, department of* ***chemistry Dr. Langade M. M,*** *who inspired and helped me always whenever I need his support. I am so much thankful to* ***Dr. Ram Kadam****,* ***Dr. A. B. Kadam****,* ***Dr. Rajmane S.V,Dr. Mahesh Mane****,* ***Dr. Patange S.M,Prof. Wahule V. W****and my departmental colleagues* ***Dr. D. N. Gattlewar, Dr.V.G. Mane,Shri. S. B. Shaiwale,Shri P. R. Bhure*** *and* ***Shri D. R. Chavan*** *for having moral support.*

*I wish to record my tributes to my dearest father****Late.MurlidharPachpinde (Dada)****.This work could not be completed without moral support and inspiration from my uncle and aunt,****Eknath,Swati,Damodar, Sunita,****my mother****Chabubai,****brothers, sisters, other family members and all my friends. I am grateful to my uncle* ***Machindra and aunt Sangita****who have always been the part of my encouragement.*

*I want to thank to the most important person in my life, my wife****Mrs. Avanti*** *for giving me the most unconditional love and always trusted me no matter what, and supported me when I mostly needed it. All the triumph I have made in my life I owe it to her. I am really grateful to my lovely daughter* ***Sphurti****and son****Kanishka*** *who missed me very much whenever they wanted me with them; actually their sacrifices are far above my words.*

TABLE OF CONTENT

List of Tables

List of Figures

List of Abbreviations

Abbreviation	Full Name
RE	Rare Earth
Ms	Saturation Magnetization
HC	Coercivity
Mr	Remanence magnetization
NMR	Nuclear Magnetic Resonance
T	Tesla
XRD	X-ray diffraction
VSM	Vibrating Sample Magnetometry
SEM	Scanning Electron Microscopy
IR	Infrared Spectroscopy
AR	Analytical Reagent
FWHM	Full Width at Half Maximum
MCR	Multi component reaction
TLC	Thin layer chromatography
DMSO	Dimethyl sulphur oxide
MS	Mass spectra

Chapter # 1

Introduction to Ferrites

1.1 Introduction

1.1.1. Magnetic nanoparticles

Today, research on, and the manufacturing of, magnetic particles with sizes from a few nanometers up to micrometers have been introduced into many different applications including information carriers in biotechnology and medicine. Magnetic nanoparticles, for example, magnetite or maghemite (common iron oxides used in different biomedical applications and in data-storage systems) with diameters less than about 50 nm are single domains. Magnetic nanoparticles can be divided into particles that are superparamagnetic or thermally blocked. Superparamagnetic particles have magnetic relaxation times that are shorter than the typical time scale of the measurement. Thermally blocked particles have magnetic relaxation times that are longer than a typical time scale of measurement being used to study the particle system.

Magnetic nanoparticles show remarkable new phenomena such as superparamagnetism, high field irreversibility, high saturation field, extra anisotropy contributions or shifted loops after field cooling. These phenomena arise from finite size and surface effects that dominate the magnetic behaviour of individual nanoparticles. A particle of ferromagnetic material, below a critical particle size (<15 nm for the common materials), would consist of a single magnetic domain, i.e. a particle in a state of uniform magnetization at any field [1,2].The magnetization behaviour of these particles above a certain temperature, i.e. the blocking temperature, is identical to that of atomic paramagnets (super paramagnetism) except that an extremely large moment and thus, large

susceptibilities are involved. Magnetic nanoparticles of ferrites are of great interest in fundamental science, especially for addressing the fundamental relationships between magnetic properties and their crystal chemistry and structure.

In present scenario of condensed matter physics rare earth ions are playing an active role in magnetic oxides and results in various novel properties in perovskites and pyrochlores [3,4].The spinel oxides with formula unit AB_2O_4 [5] represent another most important and interesting class of magnetic oxides. Where magnetic disorder and exchange frustration, introduced by size mismatch of cations and competition between super exchange interactions amongst A and B site moments, gives rise to various kind of magnetic order [6]. In spite of enormous works on substitution in spinel oxides [5,7], less attention has been paid for the substitution of rare earth (RE) ions in spinel oxides. More experimental investigation of RE substitution may provide fundamental theoretical understanding of coupling effect between 3d–4f spins in spinel oxides. For example, the vector mean field-model (Heisenberg) [8] predicts the appearance of re-entrant phase in disorder magnet [7,9] where the ferrimagnetic order of longitudinal spin components coexists with the spin glass order of transverse spin components. According to the Heisenberg spin glass model a spin can rotate along any direction with respect to the applied magnetic field. However, for a strong anisotropic magnetic material, such as rare earth substituted materials, the rotation of the spin is largely controlled by the crystalline field effect of rare earth (RE) ions. If the anisotropy field is strong enough, the spin is forced to be aligned along the local anisotropy axis. The preference of the spin alignment may add amazing character to the associated spin-cluster. Consequently, critical phenomena like magnetic transitions with AT (de Almeida–Thouless) and GT (Gabay–Toulouse) lines in rare earth containing disorder magnets will be different in comparison with isotropic (Heisenberg) spin glass behaviour of transition metal ions [10]. Therefore, systematic and detailed investigations of rare earth substitution over a wide range of spinel oxides are of renewed interest and relevance. In most of the earlier known cases, rare earth (RE) ions were substituted in a long range ferrimagnetic spinels like Ni–Zn ferrite, Co^{2+} containing ferrites [11,12]. The lack of sufficient experimental reports, dealing with the rare earth substitution in a frustrated and magnetically (one sub-lattice) diluted spinel oxides, motivated us to

study the effects of rare earth (Ho and Pr) ions in cobalt ferrite spinel oxide. The cation distribution

$$[Fe^{3+}_{1-x}Co^{2+}_{x}]_A\ [Fe^{3+}_{1+x}Co^{2+}_{1-x}]_B$$

Where A: tetrahedral or A sites, B: Octahedral or B sites. This cation distribution indicates that A site is highly magnetic diluted (magnetic moment concentration ~0.2 due to Fe^{3+} is below the percolation limit ~0.33 for the occurrence of long range ferrimagnetic order in spinel oxide). The B site moments form finite clusters and the spins inside the clusters are canted due to comparable or even weaker inter-sub lattice superexchange (J_{AB}) interactions than B sub lattice (J_{BB}) superexchange interactions [13]. If RE^{3+} ions are introduced in this system, the B site Fe^{3+} ions will be replaced due to strong B site occupancy of RE ions, and we expect that some of the clusters will contain RE^{3+} ions [14].

1.1.2. Ferrites

Ferrites are iron based oxides with technologically fascinating magnetic properties, making them a prominent category in magnetic materials. The ferrite particles in nano-regime with significant change of physical properties provide more advantages over the bulk ferrites [15]. With regards to the rapidly mounting field of nanotechnology, ferrite nanoparticles have been the core of extensive research pertaining to their widespread applications, be it biomedical, techno-logical or industrial. Nanocrystalline particles of magnetic materials show substantially enhanced magnetic properties.

The unit cell of the spinel ferrite is formed by doubling the face centered cubic oxygen sub-lattice along each of the three dimensions. In this arrangement 64 tetrahedral or A-sites and 32 octahedral or B-sites are created in the unit cell. In stoichiometric spinels only 8 A-sites and 16 B-sites are filled by divalent transition-metal ions. The spinel compounds belong to the space group Fd3m (F41/d32/m, No. 227 in the International Tables for X-ray Crystallography) with lattice parameter 8.5 Å. In mixed spinel ferrites the concentrations of ferrous, ferric and substituted metal ions and their distribution over tetrahedral and octahedral sites play a vital role in determining their magnetic and electrical properties. In normal spinels, all the A-sites are occupied by divalent transition metal ions while

in inverse spinels; the divalent ions occupy B-sites. In disordered spinels the divalent ions are present on both A and B-sites. The normal and inverse spinels are two extremes between which the cation distribution may vary. When the origin of the unit cell is taken at the centers of symmetry $\bar{4}3m$ and $\bar{3}$ m, then oxygen positional parameter '*u'* (the distance between the oxygen ion and the face of the cube edge along the cube diagonal of the spinel sub-cell has ideal values 0.375 (3/8) and 0.250 (1/4) respectively, for a perfect cubic close-packed arrangement of oxygen ions. In this case the octahedral cation–anion distance or bond length is 1.155 times larger than the tetrahedral bond length. A deviation from the ideal structure occurs when oxygen is displaced along (111) direction to accommodate the constituent cations, the tetrahedral site with smaller volume enlarges at the expense of the octahedral site and then 'u' value greater than 0.375. In order to control the domain of ferrite's applications, the investigation of cation distribution on A and B sites and oxygen positional parameter 'u' is most important [16, 17].

1.1.3. *Applications of ferrites*

The field of spinel ferrites is well cultivated because of their various potential applications and the interesting physics involved in it. Even after more than half of the century the scientist, researchers, technologist, and engineers are still excited in various types of bulk as well as nanocrystalline ferrite materials. The recent trend is focused on the doped ferrites prepared using various synthesis techniques with different cation concentrations which in turn affects the various properties like, electrical, dielectric, and magnetic behavior. Ferrite materials are important magnetic materials, which have various applications in power conditioning and conversion. Due to their distinct magnetic properties, ferrite materials have been widely used to prepare many electromagnetic devices such as inductors, converters, phase shifters and electromagnetic wave absorbers [18-19].

Industrial applications of magnetic nanoparticles cover a broad spectrum such as magnetic seals in motors, magnetic inks for bank cards, magnetic recording media and biomedical applications such as magnetic resonance contrast media and therapeutic agents in cancer treatment [1,20-23]. Each potential application

requires the magnetic nanoparticles to have different properties. For example, in data storage applications, the particles need to have a stable, switchable magnetic state to represent bits of information, a state that is not affected by temperature fluctuations.

Inductors. Ferrites are primarily used as inductive components in a large variety of electronic circuits such as low noise amplifiers, filters, voltage-controlled oscillators, impedance matching networks etc. Their recent applications as inductors, obey among other tendencies, to the general trend of miniaturization and integration as ferrite multilayer for passive functional electronic devices. The multilayer technology has become a key technology for mass production of integrated devices; multilayer allows a high degree of integration density. Multilayer capacitors penetrated the market a few decades ago, while inductors started in the 1980s., the basic components to product.

High Frequency. There has been an increasing demand of magnetic materials for high-frequency applications such as telecommunications and radar systems, as microwave technology requires higher frequencies and bandwidths up to100 GHz. Ferrites are non conducting oxides and therefore allow total penetration of electromagnetic fields, in contrast with metals, where the skin effect severely limits the penetration of high-frequency fields [24].

Power. Power applications of ferrites are dominated by the power supplies for a large variety of devices such as computers, all kinds of peripherals, TV and video systems, and all types of small and medium instruments. The main application is in the systems known as switched-mode power supplies (SMPSs). In this application, the mains power signal is first rectified it is then switched as regular pulses (typically rectangular) at a high frequency to feed into a ferrite transformer, and finally it is rectified again to provide the required power to the instrument. An increase in power delivery and efficiency can be obtained by increasing the working frequency of the transformer.

Electromagnetic Interference (EMI) Suppression. The significant increase in the amount of electronic equipment such as high-speed digital interfaces in notebooks and computers, digital cameras, scanners, and so forth, in small areas, has seriously enhanced the possibility of disturbing each other by electromagnetic interference

(EMI). In particular, the fast development of wireless communications has led to interference induced by electric and magnetic fields. Electromagnetic interference can be defined as the degradation in performance of an electronic system caused by an electromagnetic disturbance [25]. The noise from electric devices is usually produced at frequencies higher than circuit signals. To avoid, or at least reduce EMI, suppressors should work as low-pass filters, i.e. circuits that block signals with frequencies higher than a given frequency value. There are several approaches to build EMI suppressors: soft ferrites [26], ferromagnetic metals [27], ferromagnetic metal/hexaferrite composites [29], encapsulated magnetic particles [29], and carbon nanotube composites [30].

High-density write-once optical recording: Thin films of defect spinel ferrites can be used as write-once read-many media working with blue wavelengths. In fact, because these non-stoichiometric ferrites are metastable, they can be transformed into corundum phases at moderate temperatures by a laser spot. The transformed regions have different optical indices from the starting ferrite film, making the readout process possible.

Magnetic sensors: These are used for temperature control and these can be made using ferrite with sharp and definite Curie temperature. Position and rotational angle sensors (proximity switches) have also been designed using ferrites.

Magnetic shielding: A radar absorbing paint containing ferrite has been developed to render an aircraft of submarine invisible to radar.

Pollution control: There are several Japanese installations which use precipitation of ferrite precursors to scavenge pollutant materials such as mercury from waste streams. The ferrites produced subsequently can be separated magnetically along with the pollutant.

Ferrite electrodes: Because of their high corrosion resistance, ferrites having the appropriate conductivities have been used as electrode in applications such as chromium plating.

Entertainment ferrites: Ferrites are widely used in radio and television circuits. Typically applications include deflection Yokes, fly back transformers and SMPS transformer for power applications.

1.2 Literature review and aim of the present work

A recent literature survey on the structural and dielectric properties of various spinel nanocrystalline ferrites are discussed herein brief. Many researchers have studied the influence of various rare earth doping atoms on the properties of, Li–Ni, Mn–Zn, Mg–Cu, Cu–Zn ferrites, etc. [31–34]. The results of these researches show that different rare-earth ions behave differently in spinel ferrite. In general, the permeability of ferrite (e.g. Ni–Zn) was reported to decrease with the substitution of R_2O_3. An increase of about 60% relative permeability in Sm-doped Cu–Zn ferrite is reported by Sattar et al. [35]. Jalli et al. [36] report on the Samarium (Sm) doped M-type strontium ferrite single crystals. Dwevedi et al. [37] report on the structural, electrical and magnetoreactance of Dy, Gd and Nd-doped Ni ferrites. Some literature reports the decrease in relative density of ferrites with rare earth addition. On the other hand, others report on its increase. It has been accepted that the rare-earth ions commonly reside at octahedral sites and have limited solubility in the spinel lattice due to their large ionic radii. Nevertheless, the precise value of their solubility in the spinel lattice is not well known [38, 39]. Fayek et al. [40] have reported effect of Zn substitution on dielectric properties of $Cu_{1-x}Zn_xGa_{0.5}Fe_{1.5}O_4$ ferrite prepared by solid state method. Their results of frequency dependent dielectric loss (tan ı) behavior show relaxation spectra.Where the authors determine relaxation time and the maximum frequency for the hopping mechanism. Sivakumar et al. [41] have concluded that the real part of the dielectric constant (ε′) is found to be around 100 for milled $MgFe_2O_4$ which are two orders of magnitude smaller than that of the bulk $MgFe_2O_4$. The authors also observe anomalous behavior of dielectric constant (ε′), which has been explained based on the presence of both n-type and p-type charge carriers. Kaiser [42] has investigated the effect of Ni substitution on various properties of $(Cu_{0.8-x}Zn_{0.2}Ni_x)$ Fe_2O_4 ferrites. Their electrical measurements at various compositions were investigated from room temperature up to 650K in the frequency range (10^2–10^5 Hz).They conclude that the transition temperature (Tc) of $(Cu_{0.8-x}Zn_{0.2}Ni_x)$ Fe_2O_4 increases with an increasing Ni concentration. Reddy et al. [43] studied the influence of copper substitution on structural and electrical properties of Mg-Cu-Zn ferrites prepared by microwave sintering method. Their reported results reflect that, the lattice

parameter 'a' slowly increases, whereas the density sharply increases with increasing concentration of Cu ions in the MgCuZn ferrite. Ahmed et al. [44] and Ata-Allah and Fayek [45] have reported Cu substituted Ni, Zn, and Mn ferrites. Their results show strong influence of concentration of Cu substitution on frequency and temperature dependence dielectric properties like dielectric constant (ε′) and dielectric loss (tanδ) [46]. Structural, electrical and magnetic properties of Co-Cu ferrite nanoparticles have also been studied by various workers [47]. M.A. Gabal studied structural and magnetic properties of nano-sized Cu–Cr ferrites prepared through a simple method using egg white [48]. In the recent years; there has been an increased interest in the application of Ni-Cu-Zn ferrite for the production of MLCI components. The applications of the chip inductors include [49-51]. The investigations showed an improved densification in Ni-Zn [52] and increased permeability in Cu-Zn ferrite [53] by Sm substitution. La substitutions showed an improved resistivity in Ni-Zn ferrites [54]. Similarly, these substitutions may improve the electromagnetic properties in Ni-Cu-Zn ferrites. Rare earth ions can improve densification and increase permeability and resistivity in $(Ni_{1-x-y}Zn_xCu_y)$ $RE_zFe_{2-z}O_4$ ferrites where, RE enters into the 'B' sites by displacing a proportionate number of Fe^{3+} from B to A sites. Previous studies suggest that the inhomogeneous magnetic spin structure can be effectively suppressed by La doping [55-58].

The cubic $CoFe_2O_4$ has large magnetocrystalline anisotropy energy with positive anisotropy constant. It has six easy directions along the cube edges of the crystal represented as <100>, four hard directions across the body diagonals denoted as <111> and twelve saddle points across the face diagonals, which lead to positive magnetocrystalline anisotropy constant [59,60]. The large magnetocrystalline anisotropy energy of cobalt ferrite is mainly attributed to the Co^{2+} ions on the B sites of the spinel. As the crystal field is not capable to quench the orbital magnetic moment, there is a strong spin-orbit coupling (L-S coupling) and due to this coupling there is large magnetocrystalline anisotropy energy (MAE) [61]. Depending on the method of preparation, $CoFe_2O_4$ may have normal spinel, mixed spinel or inverse spinel structures and can be expressed by:

$[Fe^{3+}_{1-x}Co^{2+}_{x}]_A\ [Fe^{3+}_{1+x}Co^{2+}_{1-x}]_B$. The parameter of inversion, *x*, is equal 0 for inverse spinel and to 1 when the spinel is normal.

Beside the all above fact discussed; rare earth elements are especially different because of their higher ionic radii and higher magnetic moment which highly influenced the properties of the spinel ferrite. Therefore, we have decided to use the rare earth doping with different composition percent in the spinel ferrite. At the same time due to its unique properties of Co-ferrite, the amount of Co^{2+} will be kept constant in the whole range of sample composition.

In the present study we have choose Ho^{3+} and Pr^{3+} rare earth element as a substitute ions for Fe^{3+} in $CoFe_2O_4$.

Multiferroic and magnetoelectric properties of single-phase $Bi_{0.85}La_{0.1}Ho_{0.05}FeO_3$ ceramics were studied by Xingquan Zhang et al. [62] R.N. Bhowmik and R. Ranganathan studied Magnetic properties in rare-earth substituted spinel $Co_{0.2}Zn_{0.8}Fe_{2-2x}$ RE_xO_4 (RE=Dy, Ho and Er, x= 0.05) [63].Effect of rare-earth Ho ion substitution on magnetic properties of Fe_3O_4 magnetic fluids were studied by R. V. Upadhyay et al. [64]. Marit Stange et al. [65] studied structural aspects of the distorted perovskite ABO_3 phase $Pr_{1-x}Sr_xFeO_3$, were studied by powder X-ray diffraction, powder neutron diffraction, 57 Fe Mössbauer spectroscopy, and Fe, Sr, and Pr L^{III}-edge EXAFS techniques. Yanfei Wu et *al.*[66] studied the structure, electromagnetic properties and microwave absorption of the hexaferrites BaCo- $NiPr_xFe_{16-x}O_{27}$ and tries to illustrate the effect of the Pr^{3+}substitution for Fe^{3+}on these properties.

In the light of the literature as discussed above, it is well known that the structural and the dielectric properties of ferrites are strongly dependent on method of synthesis, sintering temperature, chemical composition and grain structure or size. Hence, the study of such properties at different frequencies, temperatures and chemical compositions may provide valuable information about the kind and amount of additives required to obtain high quality materials for practical applications. As a result, the study of electric and dielectric properties is equally important as those of magnetic properties from the applied fundamental research point of view. By keeping the importance of $CoFe_2O_4$ and rare earth elements such

as holmium (Ho^{3+}) and praseodymium (Pr^{3+}) ions we have synthesized following two ferrite systems in order to investigate structural and magnetic properties

1. $Ho_xCoFe_{2-x}O_4$ (x = 0.0, 0.025, 0.05, 0.075, 0.1)
2. $Pr_xCoFe_{2-x}O_4$ (x = 0.0, 0.025, 0.05, 0.075, 0.1)

Methodology:

The microstructures and properties of ferrite materials are also very sensitive to the preparation methodology used in their synthesis. Many methods, such as co-precipitation, spray pyrolysis, combustion synthesis, hydrothermal synthesis, and sol–gel method [67–71], have been used for the preparation of soft ferrites. However not all methods are commercially feasible due to some intrinsic disadvantages such as complexity, time consumption, or impurity penetration.

Method of sample preparation

Sol gel method is an important mean of preparing inorganic oxides. It is a wet chemical method and a multistep process involving both chemical and physical processes. A sudden increase in viscosity is the common feature in sol-gel processing, indicating the onset of gel formation. The sol–gel method adopted in this research work has the following advantages. First, the composition of nanocrystalline sample to be homogeneous and powder sample possess high quality. Second, the heat treatment temperature is low, and the nanostructure and crystallite size of powder sample can be controlled by the annealing temperature.

Some of other important features of the sol-gel method are:

- Better homogeneity
- High purity
- Lower processing temperature
- Better size and morphological control
- More uniform phase distribution in multi component systems like ferrites.

Objectives:

a. To choose the correct rare earth element with proper ionic radii and magnetic moment as a dopant.

b. To synthesis the rare earth doped cobalt ferrite by sol-gel auto-combustion method.

c. To investigate the phase formation and structural parameter by

- X-ray diffraction technique (XRD)
- Transmission electron microscopy (TEM)
- Scanning electron microscopy (SEM)
- Infrared spectroscopy (IR)

d. To study the magnetic properties such as saturation magnetization, magneton number and coercivity by

- Vibrating sample magnetometer (VSM)

Catalytic activity:

Several transition metal oxides in the form of nano particles were employed as recyclable catalysts for one-pot multicomponent reactions. Higher surface area of nanomaterials allow them to act as effective catalysts for organic synthesis. These nanoparticles have simplified isolation procedure for product, with small amount of catalyst, affording easy recovery and recyclability of the catalyst. The general nanoparticles as a catalyst require conventional isolation techniques such as filtration or centrifugation which sometimes becomes difficult to recover completely.

To overcome this issue, the use of magnetic nanoparticles has emerged as a viable solution. Their insoluble and paramagnetic nature enables easy and efficient separation of the catalysts from the reaction mixture with external magnet.

Chapter # 2

Crystal Structure and Properties of Spinel Ferrites

2.1. Spinel Compounds

The principal member of the group has the formula, AB_2O_4; the '*A*' represents a divalent metal ion such as magnesium, iron, nickel, manganese and zinc. The quadrivalent lead ion can also occupy this site. The '*B*' represents trivalent metal ions such as aluminum, iron, chromium and/or manganese. However, titanium Ti^{4+} and Pb^{2+} etc. may also occupy this site. Solid solutioning is common in this group of minerals meaning that they may contain certain percentages of different ions in any particular specimen [72]. The majority of spinel compounds belong to the space group Fd3m. In most oxide structures, the oxygen ions are appreciably larger than the metallic ions and the spinel structure can be approximated by a cubic close packing of O^{2-} ions in which the cations (e.g. Co^{2+}, Fe^{3+}) occupy certain interstices. The structure of a spinel compound is similar to the highly symmetric structure of diamond. The position of the *A* ions is nearly identical to the positions occupied by carbon atoms in the diamond structure. This could explain the relatively high hardness and high density typical of this group. The arrangement of the other 4 ions in the structure conforms to the symmetry of the diamond structure. The arrangement of the ions also favors the octahedral crystal structure, which is the predominant crystal form and is in fact the trademark of the spinels. There are well over a hundred compounds with the spinel structure reported to date. Most of them are oxides, some are sulphides, selenides and tellurides and few are halides. Many different cations may be introduced into the spinel structure and several different charge combinations are possible; almost any combination that adds up to eight positive charges to balance eight anionic charges [73], for example $Co^{2+}Fe_2^{3+}O_4$, $Mg_2^{2+}Ti^{4+}O_4$, $Li^{1+}Al^{3+}Ti^{4+}O_4$,

$Li_{0.5}^{1+}Al_{2.5}^{3+}O_4$ and $Na_2^{1+}W^{6+}O_4$, etc.

In oxide spinels, the two types of cations do not usually differ greatly in size, because the spinel structure is stable only if the cations are rather medium sized and, in addition, the radii of the different ionic species in the same compound do not differ too much. Similar cation combinations occur in sulphides, e.g. $Zn^{2+}Al_2^{3+}S_4$ and $Cu_2^{2+}Sn^{4+}S_4$. However, in halide spinels e.g. $Li_2^{1+}Ni^{3+}F_4$ and $Li^{1+}Mn_2^{3+}/^{4+}F_4$, cations are limited to charges of +1 and +2, in order to give an overall cation: anion ratio of 3:4.

Most spinels fall into three series determined by a B metal: aluminate series with Al^{3+} (Hercynite, Gahnite, Galaxite); a magnetite series with Fe^{3+} (Magnetite, Magnesioferrite, Franklinite); a chromite series with Cr^{3+} (Chromite, Magnesiochromite). There is extensive cationic exchange (solid solution) within each series but very little between the series [74]. Spinels are classified on the basis of the distribution of cations in the two principal sites, tetrahedral site (T^-) and octahedral site (O^-), into three types.

2.1.1 Types of Spinel

Based on the coulombic energy of charged ions and their influence in the polarization of anions, large divalent ions favour tetrahedral occupancy and large trivalent ions favour octahedral occupancy. From these considerations it follows that 2-3 spinels fevours normal configuration, thus in normal spinel all divalent metal ions occupy tetrahedral A-sites and all trivalent ions occupy octahedral B-sites symbolically normal spinels can be represented as

$(M)^A [Fe^{3+}M^{2+}]^B O_4^{2-}$

Example: Zinc ferrites $(Zn)^A [Fe_2^{3+}]^B O_4^{2-}$

If half of the Fe^{3+} ions occupy A-site and remaining half of the Fe^{3+} ions and all the M^{2+} ions occupy B-site, we call this structure as inverse spinel.

Example: $(Fe)^A[Co\text{-}Fe]^B O_4^{2-}$, $(Fe)^A [Ni\text{-}Fe]^B O_4^{2-}$

In spinel ferrites if the divalent metal ions and trivalent Fe^{3+} ions are distributed randomly over the tetrahedral and octahedral B-sites, then the spinel ferrite is called random spinel.

Example: Magnesium ferrite

$$(Mg_{0.1}Fe_{0.9})^{A}\,[Mg_{0.9}Fe_{1.1}]^{B}\,O_4^{2-}$$

A whole range of possible distribution is observed. This can be represented in general terms by

$$(Me_{\delta}^{II}\,Fe_{1-\delta}^{III})^{A}\,[Me_{1-\delta}^{II}\,Fe_{1+\delta}^{III}]^{B}\,O_4^{2-}.$$

Where the ions inside the bracket are located in octahedral sites and the ions outside the brackets in tetrahedral sites. The limiting case, $\delta=1$ is called normal spinel and the other limiting case, when $\delta=0$ is called inverse spinel. For a random distribution δ can have value in between 0 and 1.

2.2 Spinel Ferrite

2.2.1. Chemical Composition of Spinel Ferrite

Complex oxides with the spinel structure often called "spinels" belong to the group of strategic materials which are used in the wide area of modern technologies. They exhibit excellent magnetic, refractory, semiconducting, catalytic and sorption properties. The general chemical formula of ferrites possessing the structure of the mineral spinel, $MgAl_2O_4$, is $MeFe_2O_4$, where Me represents a divalent metal ion with an ionic radius approximately between 0.6 and 1Å.

In the case of simple ferrites, Me is one of the transition elements Mn, Fe, Co, Ni, Cu and Zn, or Mg and Cd. A combination of these ions is also possible, a mixed ferrite. The symbol Me can represent a combination of ions which have an average valency of two e.g. Li^{1+} and Fe^{3+} in lithium ferrite, $Li_{0.5}Fe_{2.5}O_4$. The trivalent iron ions ($Fe^{3+)}$ in $MeFe_2O_4$ can be completely or partly replaced by another trivalent ion such as Al^{3+} or Cr^{3+}, giving rise to mixed crystals with aluminates and chromites.

These compounds are also ferrimagnetic at room temperature if large amount of non-magnetic ions are not present. If the ferric ions are replaced by a tetravalent ion like Ti^{4+}, an equal part of the Fe^{3+} are changed into Fe^{2+}. A great variety of the chemical composition of ferrimagnetic oxide with spinel structure is possible.

2.2.2. Crystal structure of Spinel Ferrite

The smallest cell of the spinel lattice that has cubic symmetry contains eight "molecules" of $MeFe_2O_4$. The relatively large oxygen ions form an *fcc.* lattice. In the cubic close packed structure two kinds of interstitial sites occur, the tetrahedral (A) and octahedral [B] sites which are surrounded by 4 and 6 oxygen ions respectively. In the above mentioned cubic unit cell, 64 tetrahedral and 32 octahedral sites are present, of which only 8 and 16 respectively, are occupied by metal ions.

In a tetrahedral site, the interstitial is in the center of a tetrahedron formed by four lattice atoms. Three atoms, touching each other, are in plane; the fourth atom sits in the symmetrical position on top. Again the tetrahedral site has a defined geometry and offers space for an interstitial atom. An octahedral position for an (interstitial) atom is the space in the interstices between 6 regular atoms that form an octahedron. Four regular atoms are positioned in a plane; the other two are in a symmetrical position just above or below. All spheres can be considered to be hard and touching each other. The six spheres define a regular octahedron, in its interior there is a defined space for an interstitial atom, bordered by six spheres. The primitive tetrahedral unit cell of spinel ferrite consists of two molecular $MeFe_2O_4$ units and is represented by two octants as shown in the Fig. 2.1. Four primitive unit cells (Fig. 2.1) combine to form the conventional, cubic unit cell of spinel.

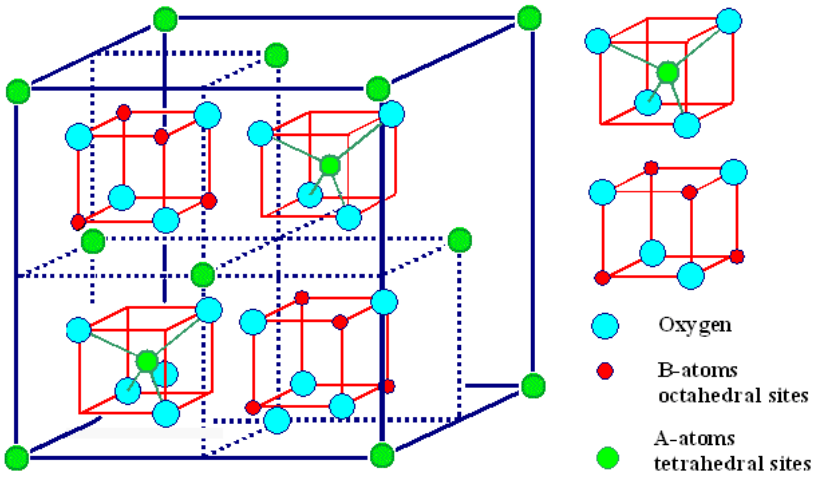

Fig.2.1. $MeFe_2O_4$ Spinel structure [75]

2.3 Magnetic properties

Magnetic material exhibits different kind of magnetic ordering depending upon spin orientation. The magnetic behaviour is caused by spinning of electrons of'd' orbital about their own axis gives rise to spin magnetic moments. The motion of electron in the orbit around the nucleus results in orbital magnetic moments. In case of transition element, these orbital magnetic moments get quenched by crystalline electrical field. The different magnetic behaviour observed is due to different contribution of electron spin.

2.3.1. Classification of Magnetic Properties

On the basis of electron spin magnetism is classified in number of classes as diamagnetism, paramagnetism, ferromagnetism, anti-ferromagnetism and ferrimagnetism.

- ***Diamagnetism:*** In this type of material, the resultant electron spin on each cation is zero.
- ***Paramagnetism:*** Paramagnetism results if there is no interaction between the spin of different atoms.
- ***Ferromagnetism:*** Positive interaction between the spin of the different atom, causing them to align parallel to each other, yields ferromagnetism.
- ***Antiferromagnetism:*** When the spins are antiparallel, due to interaction, it results in antiferromagnetism.
- ***Ferrimagnetism:*** Due to presence of both negative and positive interaction, when some spins are antiparallel to some other but leaving a resultant moment, then it is known as ferrimagnetism.

2.3.2. Magnetic Ordering and Interactions

In ferrites, the metallic ions occupy two crystallographically different sites, i.e. octahedral [B] and the tetrahedral (A) site. Three kind of magnetic interactions are possible, between the metallic ions, through the intermediate O^{2-} ions, by super-exchange mechanism, namely, A-A interaction, B-B interaction and A-B interaction.

It has been established experimentally that these interaction energies are negative, and hence induce an anti-parallel orientation. In general, the magnitude of the interaction energy between the magnetic ion, Me^{I} and Me^{II} depends upon (i) the distances from these ions to the oxygen which the interaction occurs and (ii) the angle Me^{I}-O-Me^{II} represented by the term ϕ as shown in Fig. 2.2.

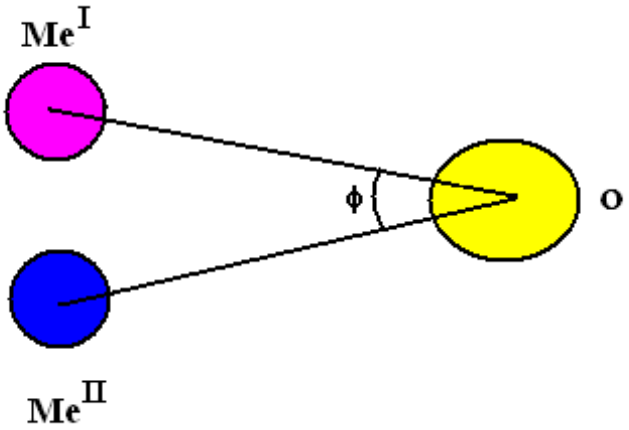

Fig. 2.2: Angle ϕ between Me^{I} and Me^{II} with oxygen ion.

An angle of 180^{0} will give rise to the greatest exchange energy and the energy decreases very rapidly with increasing distances.

The various possible configurations of the ions pairs in spinel ferrites with favourable distances and angle for an effective magnetic interaction as envisaged by Gorter are given in Fig. 2.3. Based on the values of the distance and the angle ϕ, it may be concluded that, of the three interactions the A-B interaction is of the greatest magnitude. The two configurations for A-B interaction have small distances (p, q and q, r) and the values of the angle ϕ are fairly high. Of the two configurations for the B-B interaction, only the first one will be effective since in the second configuration, the distance 's' is too large for effective interaction. The A-A interaction is the weakest, as the distance 'r' is large and the angle $\phi \approx 180$ [76].

A-B interaction	B-B interaction	A-A interaction
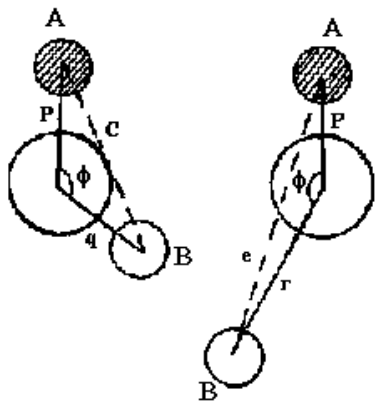	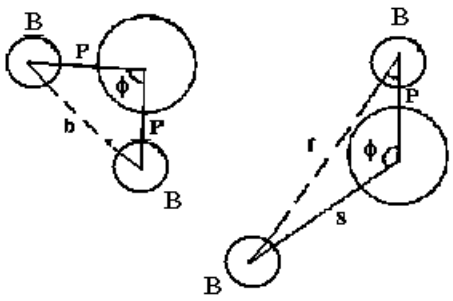	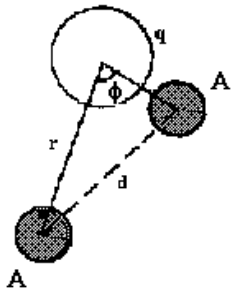
$\phi = 126^0$ $\phi=154^0$	$\phi=90^0$ $\phi=125^0$	$\phi=79^0$

Fig. 2.3: Configuration of ion pairs in spinel ferrites with favourable distance and angles for effective magnetic interaction.

Thus, with only A-B interaction predominating the spins of the A and B site ions in ferrites will be oppositely magnetized sublattice A and B with a resultant magnetic moment equal to the difference between those of A and B site ions. In general, the value of saturation magnetic moment for the B lattice (M_B) is greater than that of the A lattice (M_A), so that the resultant saturation magnetization (Ms) may be written as

$$M_s=|M_B-M_A|$$

With this theory, Neel could satisfactorily explain the experimentally observed magnetic susceptibility and magnetic saturation data obtained for ferrites. Theoretically computed values of the saturation magnetic moments per formula unit of the ferrites agree very well with the experimental values as seen from Table 2.2.

2.3.3. Magnetization

The magnetization is a powerful tool to study the different parameters such as domain wall rotation, anisotropy, magnetic hardness or softness of material, magnetic ordering etc. Ferrites exhibit almost all the properties similar to that of ferromagnetic materials. When the magnetic field is applied to the ferromagnetic material, the magnetization may vary from zero to saturation value. This behaviour is expressed by Weiss [77] by introducing the idea of existence of domains. According to Weiss, though each domain is spontaneously magnetized in the direction of field, magnetization may vary from one domain to another domain. In general, specimen consists of many domains, in domain configuration i.e. a function of applied field. The magnetic moment of specimen is a vector sum of magnetic moment of each domain. As a result the magnetization or average magnetic moment per unit volume may have value between zeros to saturation.

Studies on magnetic hysteresis of ferrite provide useful information of the magnetic parameter like saturation magnetization (Ms) coercive force (H_C) and remanence ratio (Mr/Ms). According to the values of these parameters, the ferrites can be classified as soft and hard ferrites. The ferrites with low coercive force are called soft ferrites and ferrites with high Hc are called hard ferrites. Soft ferrites are those materials which do not retain permanent magnetism, which provide easy magnetic path. Hard ferrites retain permanent magnetism and are difficult to magnetize and demagnetize. According to Neel [78] the coercive force (H_C) is related to saturation magnetization, internal stress, porosity [79] and anisotropy [80]. The Hysteresis properties are highly sensitive to crystal structure, heat treatment, chemical composition, porosity and grain size.

2.3.4. Types of Magnetic Materials

Most of magnetic materials of industrial interests are ferromagnetic materials. The ferromagnetic materials can be categorized into two; one is soft magnetic materials and the other is hard magnetic materials. As shown in the magnetization curve, a ferromagnetic material with the demagnetized state does not show magnetization although they have spontaneous magnetization. This is

because the ferromagnetic materials are divided into many magnetic domains. Within the magnetic domains, the direction of magnetic moment is aligned. However, the directions of magnetic moments vary at magnetic domain walls so that it can reduce the magnetostatic energy in the total volume. In the demagnetized state, total magnetization is cancelled because of the random orientation of the magnetizations in magnetic domains. When external magnetic field is applied, domain walls migrate and disappear when all magnetic moments are aligned to the direction of the magnetic field. When all magnetic domains are wiped away and magnetizations are all aligned to the direction of the magnetic field, magnetization is saturated. This magnetization is called saturation magnetization, Ms.

2.3.4.1 Soft Magnetic Material

When domain wall can easily migrate, the ferromagnetic material can be easily magnetized at low magnetic field. These types of ferromagnetic materials are called soft magnetic material, and are suitable for applications of magnetic cores or recording heads. Since soft magnetic materials can be demagnetized at low magnetic field, coercivity Hc is low. As they can be easily magnetized, permeability is high. For ferromagnetic materials to be soft, their magnetocrystalline anisotropy and magnetostriction constant must be low. In addition, for easy migration of magnetic domains, they must have small number of defects such as crystal grains.

2.3.4.2 Hard Magnetic Materials

When domain wall is difficult to migrate, magnetization of the ferromagnetic material occurs only when high magnetic field is applied. In other words, these types of ferromagnetic materials are difficult to magnetize, but once magnetized, it is difficult to demagnetize. These materials are called hard magnetic materials, and are suitable for applications such as permanent magnets and magnetic recording media. Hard magnetic materials have high magnetocrystalline anisotropy. Since large magnetic field is required to demagnetize, their coercivity Hc is usually high, but coercivity is highly sensitive to the microstructure.

2.3.5 Hysteresis

In Fig. 2.4, various forms of magnetism are shown on a hysteresis loop. where *Ms* is saturation magnetization at which all the spins are aligned with the magnetic field; *Hc* is the coercive field which is the internal magnetic field of material; M_R is the remanent magnetization which is the magnetization retained by the material. It can be seen from the figure that superparamagnetic and paramagnetic materials do not have a hysteresis loop.

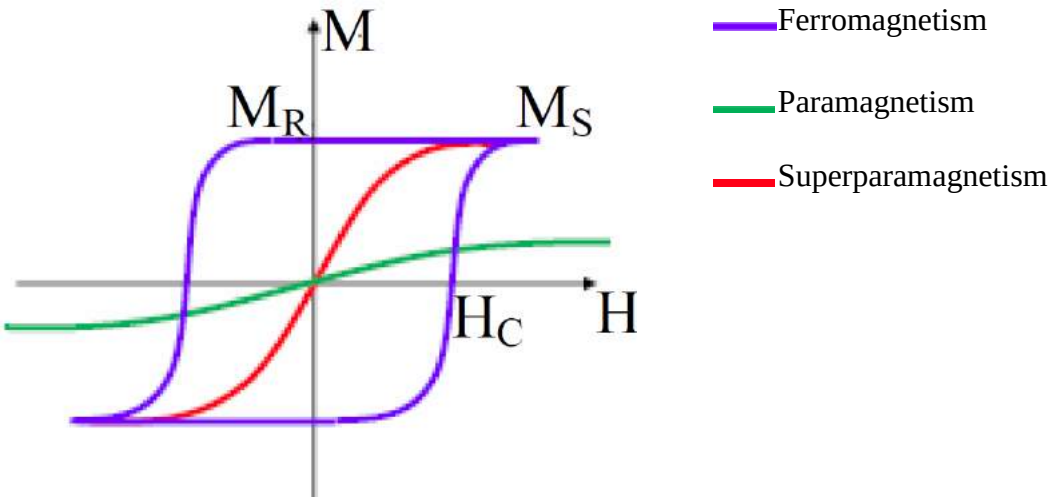

Fig. 2.4. Magnetization (*M*) vs. applied field (*H*) for ferromagnetic, paramagnetic and superparamagnetic materials.

2.3.6 Exchange Interactions

Magnetism in transition metal oxides is observed to be rather complex than that of individual isolated atoms because of the presence of coupling of atomic moments. This coupling of moments is responsible for cooperative nature of magnetism in transition metal oxides. The statistical correlation for electrons of like spin, with each surrounded by a void due to local depletion of parallel spin electrons, is called exchange. There exist three types of magnetic interactions direct exchange, double exchange and super-exchange.

2.3.6.1 Direct Exchange Interaction

When the individual moments are located close enough to allow sufficient overlap of their wave functions, the direct exchange can occur. In such conditions minimum Coulomb's interactions will be experienced when electrons are located between the nuclei. The electrons in such a condition should have opposite spins which results in anti-ferromagnetism. While ferromagnetism is observed when the moments are arranged parallel to each other, which is possible only when the electrons are located far from one another. Such a magnetic dipole-dipole interaction would be too small by a factor at least 103 to explain the observed Curie temperatures. The interaction can be explained on the basis of an exchange force, which is quantum mechanical in origin; according to Heisenberg. The exchange energy *Eex* between two atoms having spins *Si* and *Sj* is given simply by

$$Eex = -2Jex\, S_i \cdot S_j$$

$$= -2Jex\, Si\, .\, Sj\, cos\theta \qquad (2.3)$$

Where *Jex* is called exchange integral which occurs in the calculation of the exchange effect and it is a measure of the extent to which the electronic charge distributions of the two atoms concerned overlap one another, and θ is the angle between the spins. If *Jex* has a positive value then the exchange energy *Eex* is minimum when electron spins are parallel i.e., θ = 0 (ferromagnetism). If *Jex* has negative value, then *Eex* is minimum when electron spins are anti-parallel; i.e., θ = 180º (antiferromagnetism).

2.3.6.2 Super-exchange Interaction

The oxide ion has a very small interaction magnitude with metallic ions in its ground state because of a completely filled 2p orbital. The superexchange interaction has been proposed for the case in which there is a mechanism of excitation from this ground state as the interaction can only take place in the excited state with the metallic ion. The possible excitation mechanism involves the temporary transfer of one oxide *2p* electron to a neighboring metal ion. Qualitatively we can describe the superexchange interaction by considering the following example of ferric ions in an oxide (Fig 2.5). We go from a ground state of these ferric ions in which the five *3d* electrons according to Hund's rule are all

aligned parallel to each other. The six *2p* electrons of the oxygen ion form three pairs. The spin of electrons in each of these pairs is paired and they reside in a dumb-bell shape *p*-orbital. In an excited state the electron from the nearby oxide ion leaves the *p*-orbital and becomes (temporarily) part of Fe^{3+} ion, which becomes Fe^{2+} on gaining Néel electron. The transfer process in which we have one Fe^{3+} ion on one side of the oxygen and another Fe^{3+} ion on the other side is given as shown in (Figure 2.5).

The one Fe^{3+} ion now becomes a Fe^{2+} ion. The unpaired electron of the oxygen *p* orbital which was directed toward the Fe^{3+} ions now can interact with the Fe^{3+} ion present on the opposite side.

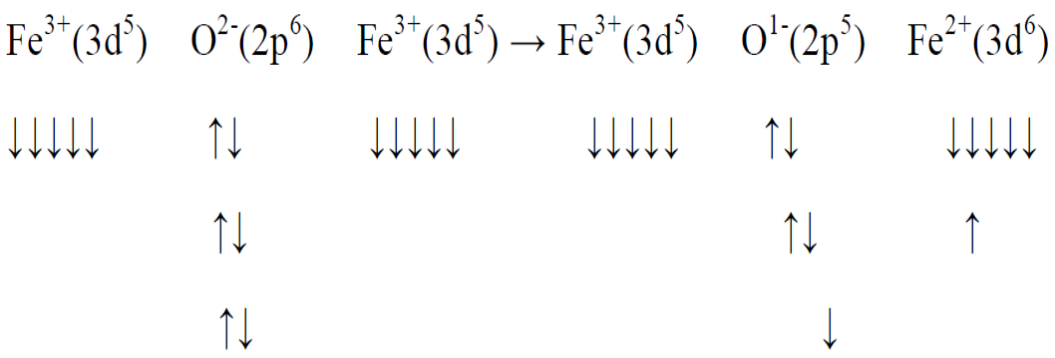

Fig. 2.5. Super-exchange Interactions [10]

The overall coupling between the cations depends on a combination of direct exchange, excitation and intra-atomic (Hund's Rule) coupling, and is known as superexchange. If the *3d* orbital of the metal ions are less than half full, the superexchange should favour a positive interaction; for *3d* shells which are half filled or more than half filled, e.g. Fe^{3+} ion, a negative interaction with anti-parallel spin is probable. It is generally assumed that this superexchange interaction diminishes rapidly as the distance between the ions increases. The dumbbell shape of the *2p* orbital makes it reasonable to assume that the interaction for a given ionic separation is greatest when the metal oxygen-metal angle is 180° and is least when this angle is 90°. Thus in a spinel lattice we conclude that *AB* interaction is relatively strong, the *A-A* interaction is relatively weak and the *B-B* interaction is probably intermediate [81].

2.3.7 Magnetic Anisotropy

In most magnetic materials, to varying degree, the magnetization tends to align itself along one of the main crystal directions. That direction is called the easy direction of magnetization. All ferromagnetic and ferrimagnetic materials possess, to a lesser or greater degree, a crystal direction or a set of directions in which the magnetization prefers to be oriented [82].

This magnetic anisotropy can have various causes. The most important in magnetic materials are the shape and magnetocrystalline anisotropies. Shape anisotropy is associated with the geometrical shape of a magnetized body, and refers to the preference that the polarization in a long body is for the direction of the major axis. The magnetocrystalline anisotropy is associated with the crystal symmetry of the material. There are three situations that give rise to this anisotropy as an intrinsic crystal property. The first and most important one is that in which the atoms possess an electron-orbital moment in addition to an electron-spin moment. In such a situation the spin direction may be coupled to the crystal axis. This arises through the coupling between spin and orbital moments and the interaction between the charge distribution over the orbit and the electrostatic field of the surrounding atoms. There will be one or more axes or surfaces along which magnetization requires relatively little work. The crystal will then be preferentially magnetized along such an easy axis or plane. The second situation is encountered in non-cubic crystal lattices. In these crystals the magneto-static interaction between the atomic moments is also anisotropic, which may give rise to easy directions or planes of magnetization. The third possibility of crystal anisotropy is found in the directional ordering of atoms as described by Néel [78]. This typically involves solid solutions of atoms of two kinds, A and B, linked by the atomic bonds *A-A*, *A-B* and *B-B*. In the presence of a strong external magnetic field the internal energy of these bonds may be to some extent direction-dependent. Given a sufficient degree of atomic diffusion as a result of raising the temperature, for example a certain ordering can be brought about in the distribution of the bonds; in this way it is possible to "bake" the direction of this field into the material as the easy axis of magnetization. In addition to these sources of magnetocrystalline anisotropy mechanical stresses may contribute through the magneto-elastic

(magneto-strictive) properties of the crystal. This contribution, however, is considered to be negligible in hard magnetic materials [82].

Chapter # 3

Synthesis Method and Characterization Techniques

This chapter presents a brief background of the various methods of sample preparation and characterization techniques used for studying properties (like structural, electric, dielectric, and magnetic) of presently investigated ferrite systems. The details of experimental techniques, various characterization equipments and their working details are also given in this chapter

3.1 Synthesis Method

Sol gel method is an important mean of preparing inorganic oxides. It is a wet chemical method and a multistep process involving both chemical and physical processes. A sudden increase in viscosity is the common feature in sol-gel processing, indicating the onset of gel formation.

The important features of the sol-gel method are.

a) Better homogeneity

b) High purity

c) Lower processing temperature

d) Better size and morphological control

d) More uniform phase distribution in multi component systems like ferrites.

The steps in sol gel synthesis are as follows.

i) Hydrolysis

The process of hydrolysis may start with a mixture of metal alkoxide and water in a solvent usually alcohol at the ambient or slightly elevated temperature.

ii) Polymerization

This step involves condensation of adjacent molecules where in H_20 and alcohol, are eliminated and metal oxide linkages are formed. Polymeric networks grow to colloidal dimensions in the liquid (sol) state.

iii) Gelation

In this step, the polymetric networks link up to form a three dimensional network throughout the liquid. The system becomes somewhat rigid, on removing the solvent from the sol. Solvent as well as water and alcohol molecules remain inside the pores of the gel.

iv) Drying

Water and alcohol are removed at moderate temperatures leaving a hydroxylated metal oxide with residual organic content.

V) Dehydration

This step is carried out between 670 K and 1070 K to take off the organic residues and chemically bound water, yielding a glass metal oxide.

VI) Densification:

Temperature in excess of 1270K is used to form the dense oxide product. The sol-gel technique has been used to prepare sub micrometer metal oxide powders with a narrow particle size distribution and unique particle shapes. Metal - ceramic composites as well as organic- inorganic composites have been prepared by the sol gel route. Fig. 3.1 depicts the flow chart of sol-gel auto-combustion method.

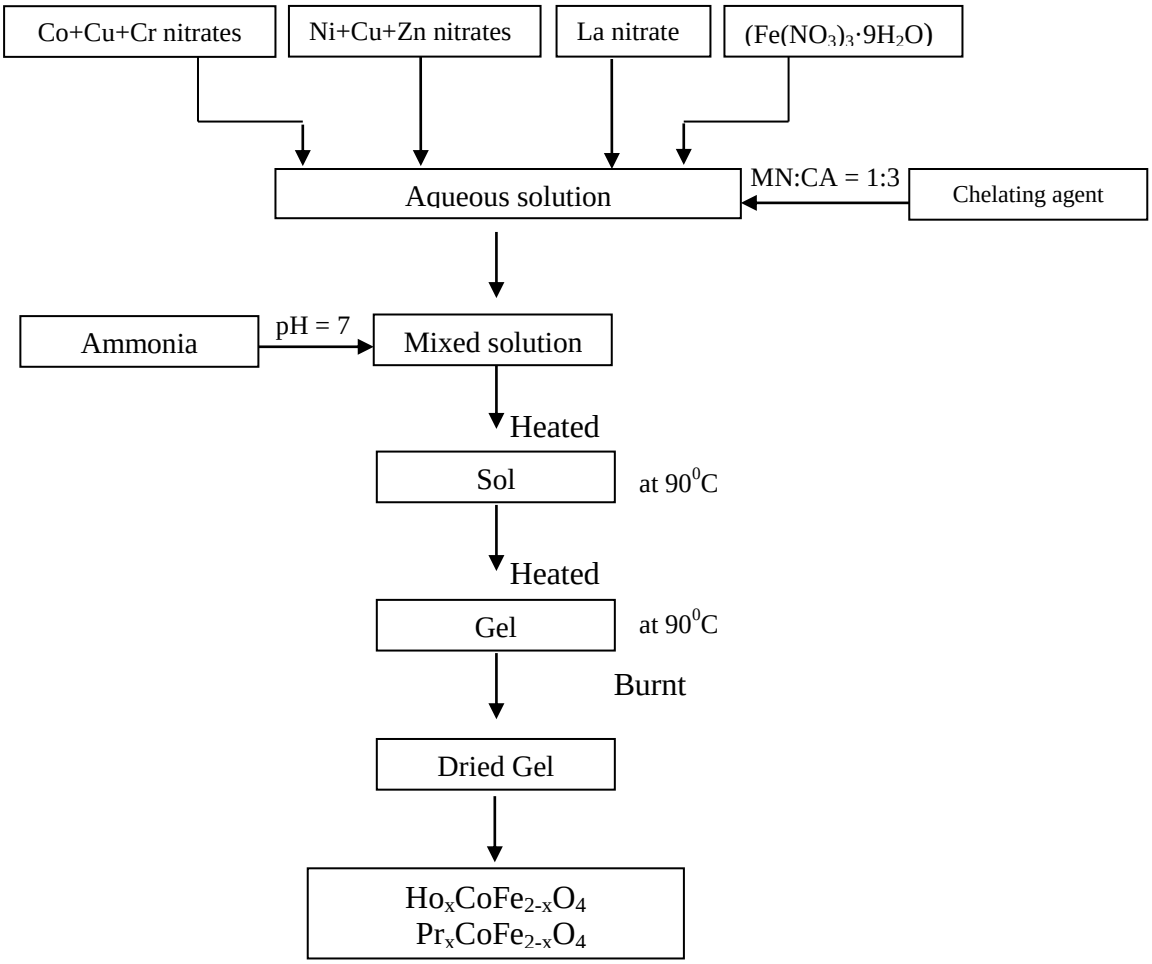

Fig. 3.1: Flow chart of sol-gel auto-combustion method

3.2 Characterization techniques

3.2.1 X-ray Diffraction

The X-ray diffraction technique is used for the structural/phase analysis of the material under investigation. The basic principle is that for a fixed wavelength (λ), the constructive interference occurs for a fixed set of an interplaner spacing (d) and incidence angle (θ) (Figs. 3.3 & 3.3). According to Bragg's condition of diffraction:

$$\lambda = 2d\sin\theta \qquad \textbf{3.1}$$

For cubic system, d is given by

$$\frac{1}{d^2} = \frac{h^2+k^2+l^2}{a^2} \qquad \textbf{3.2}$$

Combining the above two equations we get a relation, which predict the diffraction angle for any set of planes for a given 'λ' if the following condition is satisfied,

$$Sin^2\theta = \frac{2}{4a^2}(h^2 + k^2 + l^2) \qquad \textbf{3.3}$$

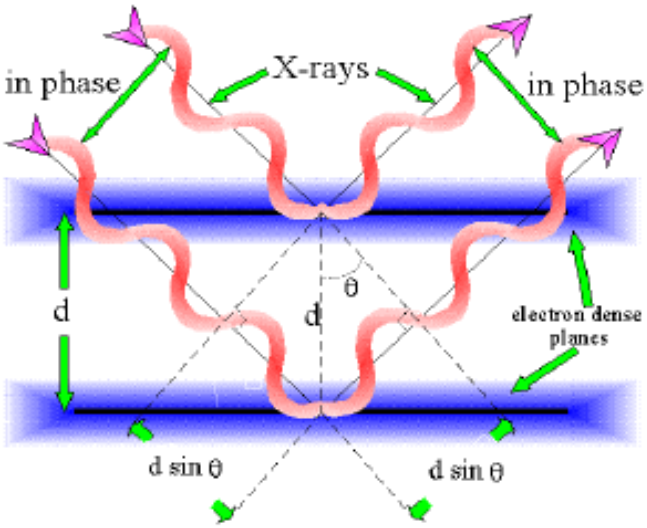

Fig. 3.2: Basic principle involved in diffraction of X- ray beam from assembly of lattice-atoms

It is seen that diffraction directions are determined by the shape and size of the unit cell. This is an important point. All we can possibly determine about an unknown crystal by the measurement of the directions of diffracted beams are the shape and size of its unit cell. The intensities of diffracted beams are determined by the positions of the atoms within the unit cell and it follows that we must measure intensities if we are to obtain any information about the atom positions. It is also found for many crystals, that there are particular atomic arrangements, which reduce the intensities of some diffracted beams to zero. In such cases, there is simply no diffracted beam at the angle predicated by the equations of the type eqs. (3.3 and 3.4). It is in this sense that equations of this kind predict all possible diffracted beams.

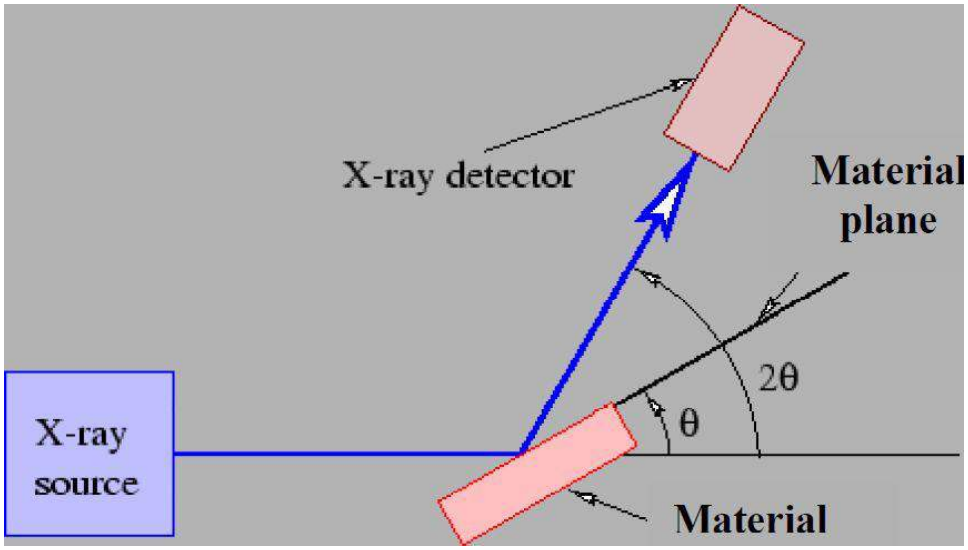

Fig. 3.3: Schematic diagram of Bragg's diffraction

While indexing for cubic structure, it has to be kept in mind that for simple cubic and simple tetragonal all (h k l) values are permissible, yet reflections corresponding to ($h^2+k^2+l^2$) values equal to 7, 15, 23…. are all absent. The reflection peaks for bcc satisfy the condition h+k+l = 2n. For fcc structure, the reflection peaks are found to have (h k l) values either all even or all odd. The average grain size of the sample can be calculated from the width of the peak by using the relation:

$$B = \frac{K\lambda}{L\cos\theta} \qquad \textbf{3.4}$$

Where B is the broadening of line expressed in the unit of 2θ, K is a constant ~ 1 in most case and L is the average length of the crystallites; and λ and θ have their usual meanings.

Generally, X-ray diffraction provides information about the:

(a) Long range order structure

(b) Phase composition

(c) Crystallinity, crystal size and shape

(d) Micro-stress and strain

(e) Texture (crystal orientation)

X-ray diffraction technique is a powerful technique to study the crystal structure of a material. Qualitatively and quantitatively it also determines the amorphous contain of the sample. The technique helps in identifying the constituents of multiphase mixture. The X-ray diffraction pattern yields information of the position of Bragg's peaks. The XRD patterns also helps to identify the structural phases present in the end product obtain by the method of preparation used. The XRD patterns of all the samples were recorded on Philips X-ray diffractometer (Model 3710) by employing the following specification.

Target:	Cu-Kα
2θ range:	$20\text{-}80^0$
Step width:	0.02,
Count rate:	400-700 counts/sec.

3.2.2 Transmission Electron Microscopy (TEM)

Transmission Electron Microscopy (TEM) is a well known technique for imaging solid materials at atomic resolution. Structural information can be acquired both by (high resolution) imaging as well as by electron diffraction. Additional detectors allow for elemental and chemical analysis down to this sub-nanometer scale.

Basic Principles

The design of a transmission electron microscope (TEM) is analogous to that of an optical microscope. In a TEM high-energy (>100 kV) electrons are used instead of photons and electromagnetic lenses instead of glass lenses. The electron beam passes an electron-transparent sample and a magnified image is formed using a set of lenses. This image is projected onto a fluorescent screen or a CCD camera. Whereas the use of visible light limits the lateral resolution in an optical microscope to a few tenths of a micrometer, the much smaller wavelength of electrons allows for a resolution of 0.2 nm in a TEM.

Imaging

Image contrast is obtained by interaction of the electron beam with the sample. Several contrast effects play a role. In the resulting TEM image denser areas and areas containing heavier elements appear darker due to scattering of the electrons in the sample. In addition, scattering from crystal planes introduces diffraction contrast. This contrast depends on the orientation of a crystalline area in the sample with respect to the electron beam. As a result, in a TEM image of a sample consisting of randomly oriented crystals each crystal will have its own grey-level. In this way one can distinguish between different materials, as well as image individual crystals and crystal defects. Because of the high resolution of the TEM, atomic arrangements in crystalline structures can be imaged in large detail.

Electron Diffraction

By adjusting the magnetic lenses such that the back focal plane of the lens rather than the imaging plane is placed on the imaging apparatus a diffraction pattern can be generated. For thin crystalline samples, this produces an image that consists of a pattern of dots in the case of a single crystal, or a series of rings in the case of a polycrystalline or amorphous solid material. For the single crystal case the diffraction pattern is dependent upon the orientation of the specimen and the structure of the sample illuminated by the electron beam. This image provides the investigator with information about the space group symmetries in the crystal and the crystal's orientation to the beam path. This is typically done without utilising any information but the position at which the diffraction spots appear and the observed image symmetries.

Diffraction patterns can have a large dynamic range, and for crystalline samples, may have intensities greater than those recordable by CCD. As such, TEMs may still be equipped with film cartridges for the purpose of obtaining these images, as the film is a single use detector.

In case of a crystalline material, electron diffraction will only occur at specific angles, which are characteristic for the crystal structure present. As a result, a diffraction pattern of the irradiated area is created that can be projected onto the CCD camera. In this way, electron diffraction can provide

crystallographic information from thin films, bulk materials as well as from nanometer sized particles (Figure 3.4).

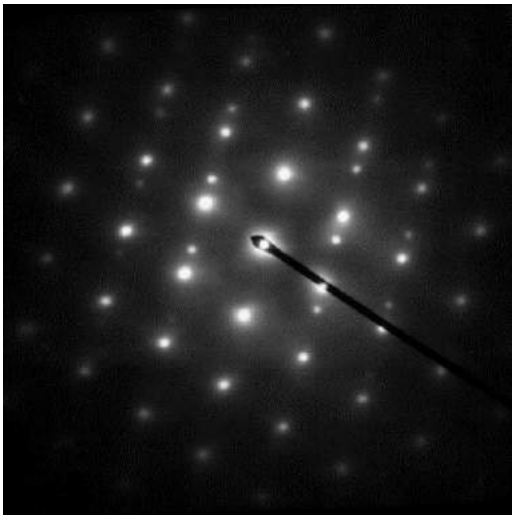

Fig. 3.4 (a): Crystalline diffraction pattern from a twinned grain of FCC Austenitic steel

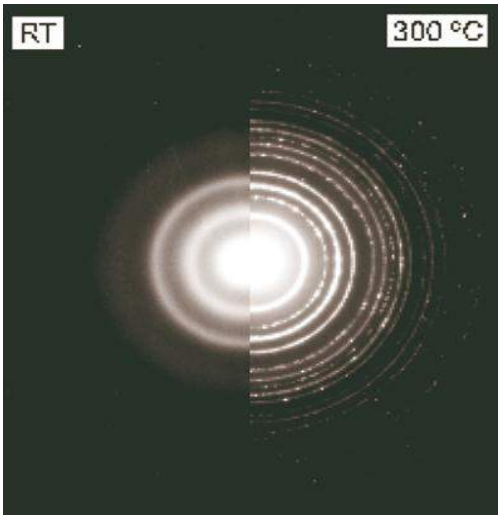

Fig. 3.4 (b): Electron diffraction patterns of an as-deposited (room temperature) and an annealed (300 ºC) Al-Ge film. The left part shows a set of a few, broad rings, characteristic of an amorphous film. The right part shows a large number of sharp rings. The diameters of these rings are characteristic for the crystal structure present. In this case a mixture of crystalline Al and crystalline Ge.

Chemical Analysis

As a result of the interaction of the electron beam with the specimen, some energy is transferred from the electrons to the sample. The excitation and de-excitation of atoms and molecules in the sample allow (local) chemical analysis. This analysis can either be performed using the broad beam used for normal imaging, or by focusing the beam size down to 0.2 nm. The combination of Scanning TEM (STEM), a mode in which this narrow beam scans a selected area of the specimen, with chemical analysis techniques such as Electron Energy Loss Spectroscopy (EELS) and Energy Dispersive X-Ray analysis (EDX) allows for mapping of the lateral distribution of elements with high spatial resolution.

3.2.3 Scanning Electron Microscope (SEM)

A scanning electron microscope is a type of electron microscope that images a sample by scanning it with a high-energy beam of electrons in a raster scan pattern. The electrons interact with the atoms that make up the sample

producing signals that contain information about the sample's surface topography, composition, and other properties such as electrical conductivity.

The types of signals produced by the SEM include secondary electrons, back-scattered electrons (BSE), characteristic X-rays, light (cathode), specimen current and transmitted electrons. Secondary electron detectors are common in all SEMs, but it is rare that a single machine would have detectors for all possible signals. The signals result from interactions of the electron beam with atoms at or near the surface of the sample. In the most common or standard detection mode, secondary electron imaging or SEI, the SEM can produce very high-resolution images of a sample surface, revealing details about less than 1 to 5 nm in size. Due to the very narrow electron beam, SEM micrographs have a large depth of field yielding a characteristic three-dimensional appearance useful for understanding the surface structure of a sample. This is exemplified by the micrograph of pollen shown to the right. A wide range of magnifications is possible, from about 10 times (about equivalent to that of a powerful hand-lens) to more than 500,000 times, about 250 times the magnification limit of the best light microscopes. Back-scattered electrons (BSE) are beam electrons that are reflected from the sample by elastic scattering. BSE are often used in analytical SEM along with the spectra made from the characteristic X-rays. Because the intensity of the BSE signal is strongly related to the atomic number (Z) of the specimen, BSE images can provide information about the distribution of different elements in the sample. For the same reason, BSE imaging can image colloidal goldimmuno-labels of 5 or 10 nm diameter which would otherwise be difficult or impossible to detect in secondary electron images in biological specimens. Characteristic X-rays are emitted when the electron beam removes an inner shell electron from the sample, causing a higher energy electron to fill the shell and release energy. These characteristic X-rays are used to identify the composition and measure the abundance of elements in the sample.

The electron beam comes from a filament, made of various types of materials. The most common is the Tungsten hairpin gun. This filament is a loop of tungsten which functions as the cathode. A voltage is applied to the loop, causing it to heat up. The anode, which is positive with respect to the filament, forms powerful attractive forces for electrons. This causes electrons to accelerate

toward the anode. Some accelerate right by the anode and on down the column, to the sample. Other examples of filaments are Lanthanum hexaboride filaments and field emission guns.

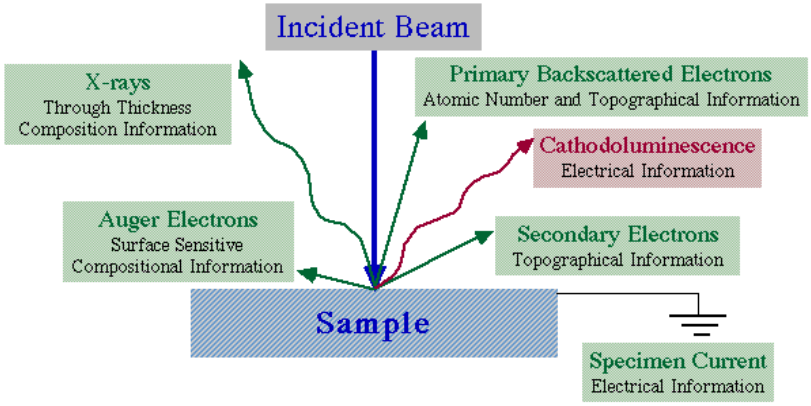

Fig 3.5: Electron specimen interaction.

The SEM uses electrons instead of light to form an image. A beam of electrons is produced at the top of the microscope by heating of a metallic filament. The electron beam follows a vertical path through the column of the microscope. It makes its way through electromagnetic lenses which focus and direct the beam down towards the sample. Once it hits the sample, other electrons (backscattered or secondary) are ejected from the sample. Detectors collect the secondary or backscattered electrons, and convert them to a signal that is sent to a viewing screen similar to the one in an ordinary television, producing an image.

3.2.4 Infrared Spectroscopy (IR)

Infrared spectroscopy is the method of choice of qualitative analysis of organic material and it has wide application to inorganic substances as well. The infrared spectrum of a material has aptitude for the fingerprint, a unique property of that material and of its physical state. The spectrum is unique because it reflects the vibration between atoms within the molecule, and even slight changes in

geometry or bond strength between atoms cause noticeable shift in the infrared absorption pattern.

When a molecule interacts with the radiation of the proper frequency, it absorbs energy and molecule is set into vibration. By measuring the transmitted energy as a function of radiation frequency, we can determine which frequency has been absorbed by the sample. The resulting plots of energy versus frequency are the infrared spectrum of the sample.

The infrared spectra of all the samples of the present series were recorded at room temperature in the range 300 - 800cm^{-1} on a Perkin Elemer spectrometer (Model 783). To study the IR spectra of all the samples, about one gram of fine powder of each sample was mixed with KBr in the ratio 1:250 by weight to ensure uniform distribution in the KBr pellet. The mixed powder was then pressed in a cylindrical die to obtain clean disc of approximately 1 mm thickness. The IR spectra were used to locate the band position. The IR spectra were used to determine bond length R_A and R_B, in a cubic crystal for tetrahedral (A) and octahedral [B] site using formula given by Gorter [83]. Using the analysis of Waldron [84], the force constant K_0 and K_t were calculated.

3.2.5 Vibrating Sample Magnetometer (VSM)

A vibrating sample magnetometer or VSM is a scientific instrument that measures magnetic properties invented in 1955 by Simon Foner at Lincoln Laboratory MIT. The paper about his work was published shortly afterward in 1959 [85]. A sample is placed inside a uniform magnetic field to magnetize the sample. The sample is then physically vibrated sinusoidally, typically through the use of a piezoelectric material. Commercial systems use linear actuators of some form and historically the development of these systems was done using modified audio speakers, though this approached was dropped due to the interference through the in-phase magnetic noise produced, as the magnetic flux through a nearby pickup coil varies sinusoidally. The induced voltage in the pickup coil is proportional to the sample's magnetic moment, but does not depend on the strength of the applied magnetic field. In a typical setup, the induced voltage is measured through the use of a lock-in amplifier using the piezoelectric signal as its reference

signal. By measuring in the field of an external electromagnet, it is possible to obtain the hysteresis curve of a material.

A typical hysteresis curve of a spinel ferrite is also shown in Fig. 3.5. A great deal of information can be learned about the magnetic properties of a material by studying its hysteresis loop. A hysteresis loop shows the relationship between the induced magnetic flux density (**B)** and the magnetizing force **(H).** It is often referred to as the B-H or M-H loop.

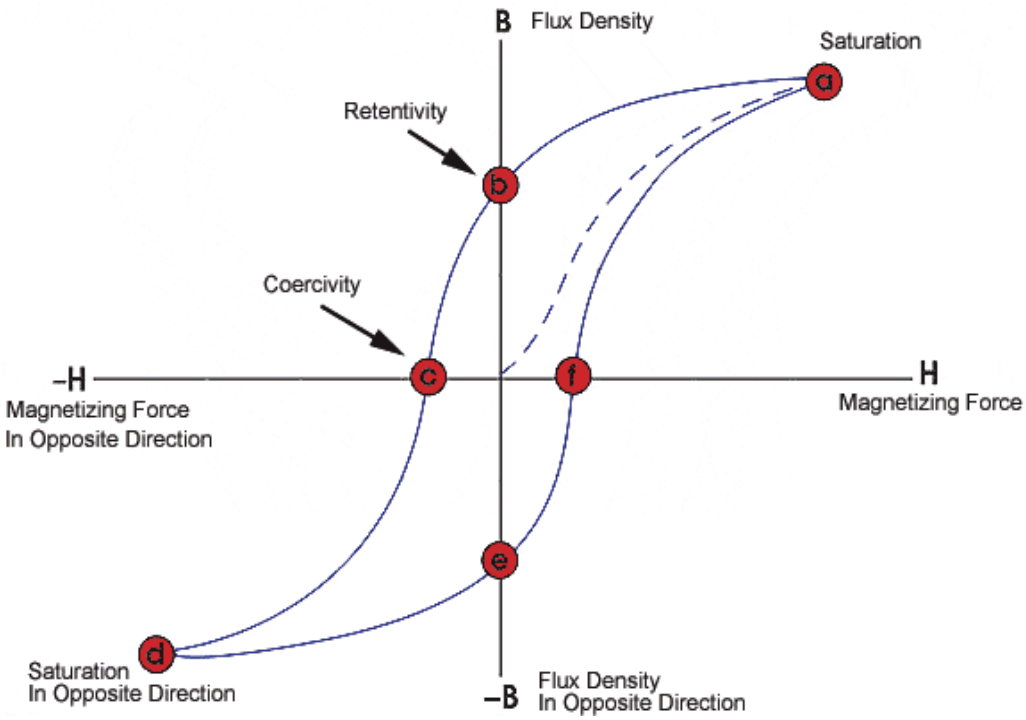

Fig. 3.6: A typical hysteresis curve of a spinel ferrite**.**

From the hysteresis loop, a number of primary magnetic properties of a material can be determined such as magnetization (Ms), coercivity (H_C), remanence magnetization (Mr) etc.

Chapter # 4

Results and Discussion on $Ho_xCoFe_{2-x}O_4$ Ferrite System

4.1 Introduction

With regards to the rapidly mounting field of nanotechnology, ferrite nanoparticles have been the core of extensive research pertaining to their widespread applications, be it biomedical, techno logical or industrial. Trends in ferrite technology in the days to come includes challenges in applications, advancement in manufacturing techniques and cost factor in both commercial and defense applications [18].

Cobalt ferrite ($CoFe_2O_4$) is a ferrimagnetic material which presents the highest magnetocrystalline anisotropy and magnetostriction coefficient among ferrites. It has been regarded as one of the competitive candidates for a variety of applications in high density magnetic recording media, microwave devices, high sensitivity sensor, and biomedical industries [86].$CoFe_2O_4$ possess an inverse spinel structure, generally, it is found that in an inverse spinel cubic crystal structure in which half of the tetrahedral sites (A-sites) are occupied by half of Fe^{3+}ions. The octahedral sites (B-sites) will be held by the leftover $Fe^{3+}$with the transition metal ions. In theory, the addition of appropriate transition metal ion into the spinel structure will generate the movement of many cations between two lattice sites and directly affect crucial properties especially magnetic behavior of ferrites. Introducing a relatively small amount of RE, an important modification of both the structure, and magnetic and electrical properties can be observed in these ferrites which has attracted the attentions of researchers. It is known that the magnetic behavior of the ferromagnetic oxides is largely governed by the Fe–Fe interaction (the spin coupling of the 3d electrons) and by introducing rare earth (RE) ions into the spinel lattice, the RE–Fe interactions may start to have an

appreciable effect (3d–4f coupling), which can lead to small change in the magnetization and curie temperature. However, the RE–RE interactions are very weak since their results from the indirect mechanism 4f–5d–5d– 4f [87]. There are a few reports available which have mentioned the synthesis of rare earth (RE^{3+}) substituted nanocrystalline spinel ferrites in single phase form using different chemical routes despite having big difference in ionic radius of RE^{3+} and Fe^{3+} ions [88-92].

In the present work, $CoFe_2O_4$ is modified on rare earth Ho^{3+} substitution due its intrinsic large magnetic moment and anisotropy. In such a case, the rotation of the spin is largely controlled by the crystalline field effect of rare earth ions and if this anisotropy field is strong enough, the spins are forced to align along the local anisotropic axis. This will lead to different types of magnetic ordering in the system.

Chemically prepared magnetic nanoparticles exhibit superior magnetic properties compared to their bulk counterparts due to small particle size and uniform distribution. In order to form these fine spinel-type ferrite particles, various wet methods have been devised including freeze-drying, spray drying, co-precipitation and sol–gel as well as dry methods such as mechanical alloying and thermal plasma [93-95].

In addition, combustion synthesis has recently been developed to synthesize ultra-fine powders of ceramic oxides. This method is very simple, cost-effective and fast. In brief, in this technique, an aqueous solution, containing an organic compound as fuel (for example glycine, citric acid, urea, etc.) and suitable metal salts as oxidizer (nitrates are generally preferred since they have good solubility in water), is introduced to a furnace or microwave oven. The solution then starts boiling. The heating and evaporation of the nitrate solution results in an exothermal, self-sustaining and fast chemical reaction [96].

Even though studies on the fabrication and the magnetic characteristics of cobalt ferrite nanoparticles substituted with different cations are rapidly expanding, however to the best of our knowledge, there is no study concerning the structural and magnetic properties of holmium (Ho^{3+}) substituted cobalt ferrite synthesized by sol-gel auto-combustion method.

Particularly, anticipating the possible contribution of Ho^{3+} and in order to enhance structural and magnetic property of $CoFe_2O_4$, we have systematically substituted Ho^{3+} in $Ho_xCoFe_{2-x}O_4$ and prepared by sol-gel auto-combustion method. XRD, SEM, TEM, IR and magnetization were carried out to understand our observation of structural and magnetic behavior in Ho substituted $CoFe_2O_4$.

4.2 Experimental

The ferrite powders were synthesized through sol-gel auto-combustion route to achieve homogeneous mixing of the chemical constituents on the atomic scale and better sinterability. AR grade cobalt nitrate ($Co(NO_3)_2 \cdot 3H_2O$), holmium nitrate ($Ho(NO_3)_3 \cdot 5H_2O$), iron nitrate ($Fe(NO_3)_3 \cdot 9H_2O$) and citric acid ($C_6H_8O_7 \cdot H_2O$), were used to prepare the $Ho_xCoFe_{2-x}O_4$ (x = 0.0, 0.025, 0.05, 0.075, 0.1) ferrite compositions. Reaction procedure was carried out in air atmosphere without protection of inert gases. The molar ratio of metal nitrates to citric acid was taken as 1:3. The metal nitrates were dissolved together in a minimum amount of double distilled water to get a clear solution. An aqueous solution of citric acid was mixed with metal nitrates solution, then ammonia solution was slowly added to adjust the pH at 7. Then the solution was heated at 90 ºC to transform into gel. When ignited at any point of the gel, the dried gel burnt in a self-propagating combustion manner until all gels were completely burnt out to form a fluffy loose powder. The auto-combustion was completed within a minute, yielding the brown-colored ashes termed as a precursor. The as prepared powder then annealed at 600 ºC for 4 h.

Sol-gel auto-combustion synthesized powder samples were X-ray examined by Phillips X-ray diffractometer (Model 3710) using Cu-K_α radiation (λ=1.5405Å). Transmission electron microscope (TEM) measurements were recorded on Philips (Model CM 200). The infrared spectra of all the samples were recorded at room temperature in the range 300 cm^{-1} to 800 cm^{-1} using Perkin Elmer infrared spectrophotometer. Room temperature magnetization of the samples was measured using the pulse field magnetization set-up.

4.3 Results and discussion

4.3.1. Structural Analysis

The XRD pattern of the as-synthesized $CoFe_2O_4$ nanoparticles is shown in Fig. 4.1. The diffraction peaks related to Bragg's reflections from (220), (311), (40 0), (422), (511) and (4 4 0) planes correspond to the standard structure of $CoFe_2O_4$ (JCPDS card no. 22-1086) which has spinel cubic type with a space group of Fd3m.As Ho^{3+} substitution increases the deviation from single phase becomes more prominent with the appearance of some un-indexed peak as secondary phase with insignificant amount of hematite phase. The formation of secondary phases in the ferrite during sintering process is governed by the type and the amount of Ho^{3+}used. Therefore, the small amount of Ho^{3+}ions in $CoFe_2O_4$ can affect not only the phase composition but also the size of the spinel matrix. This is probably due to ortho-ferrite ($HoFeO_3$) phase [63]. It has been reported [97] that phase formation is affected by the concentration of rare earth element, Ho^{3+}, in substituted samples of $CoFe_2O_4$.The most important reason for the phase formation in the Ho^{3+}substituted $CoFe_2O_4$ samples is electronic configuration and ionic radii of the Ho^{3+}rare earth element. The Ho^{3+} ion has the larger radius of about (1.04 Å) to occupy the tetrahedral ($4f_1$) or the octahedral ($12k$, $2a$, $4f_2$) sites of Fe^{3+} whose ionic radius is 0.67 Å. Therefore, when the substitution of Ho^{3+} ions is high, this lead to the formation of secondary phases on the grain boundaries because of the diffusion of RE-Ho^{3+} ions. K. Kamala Bharathi et al. [98] also observed a small distortion in the lattice upon the substitution of Fe by Ho in the B site and may relate this fact to the changes in the O-Fe and O-Co bond lengths in the B site.

The lattice parameter '*a*' was calculated using the following equation [99]:

$$a = d\sqrt{(h^2 + k^2 + l^2)} \qquad \textbf{4.1}$$

Where *d* is the inter-planer spacing and (*hkl*) is the index of the XRD reflection peak. It is observed from Table 4.1 and Fig. 4.2 that lattice constant 'a' increased from 8.355 to 8.383Å with an increase in Ho^{3+} substitution. It is very likely that the ionic size mismatch for a small substitution of Fe^{3+} atoms by Ho^{3+} alone would be able to produce such a non-monotonic increase in lattice parameter, because the radius of Ho^{3+}(1.04 Å) is larger than the radius of Fe^{3+}(0.67 Å). In searching for an

alternative explanation of the observed lattice expansion in annealed samples, the exchange of (Fe^{3+} and Co^{2+}) cations among A- and B-sites cannot be ruled out in Ho^{3+} doped $CoFe_2O_4$ nanoparticles.

The X-ray density (dx) of all the samples of the series was obtained by the following relation:

$$dx = \frac{8M}{Na^3} \qquad \textbf{4.2}$$

where '8' is the number of molecules per unit cell, 'M' is the molecular weight of sample, 'N' is the Avogadro's number and 'a' is lattice constant. It is observed from Table 4.1 and Fig. 4.3 that the X-ray density increased from 5.345 to 5.536g/cm^{3}with increase in Ho^{3+} substitution. This behaviour of X-ray density is related to the molecular weight (M) and lattice constant (a). The increase in X-ray density may be due to the greater atomic mass of Ho^{3+} (164.93 a.m.u) than that of Fe^{3+} (55.85 a.m.u)

The average crystallite diameter 'D_{XRD}' of powder estimated from the most intense (311) peak of XRD and using the Scherrer formula [99]:

$$D_{XRD} = \frac{0.9\lambda}{B\cos\theta} \qquad \textbf{4.3}$$

where λ is the wavelength used in XRD, B is the full width of half maximum in (2θ), θ is the corresponding Bragg angle. Figure 4.4 and Table 4.1 shows that the crystallite diameter increased from 32.1 to 39.7nm with an increase in Ho^{3+} substitution for x = 0.075, thereafter it decreased to 32.1 for x = 0.1.

The specific surface area (S) was calculated from the diameter of the particle in nanometer and the measured density in g/cm^3 using the relation [100]:

$$S = \frac{6000}{Dd_B} \qquad \textbf{4.4}$$

where D is the average crystallite size and d_B is the bulk density. The variation of surface area (S) with Ho^{3+} substitution is shown in Fig. 4.4 and Table 4.1.

SEM micrographs were used to obtain further structural information and selected samples are shown in Fig. 4.5 (a-e). Fig. 4.5 (a-e) show good spherical shaped particles in the material. The SEM pictures also indicate nearly uniform distribution of particles. Better grain boundaries were observed at smaller substitution of Ho^{3+} ions. Compared with the XRD results mentioned above, it can

be confirmed that after the addition of Ho^{3+}ions, the main phase of the samples is Ho^{3+} doped $CoFe_2O_4$ and grain boundary phase could be $HoFeO_3$. Further, it is observed that the grain size is decreased with Ho^{3+} substitution even though the particle size is increased. The decrease in grain size of the samples with increasing Ho^{3+} substitution ions can be explained as follows.

The Ln^{3+} ions have empty or half-filled or fully filled 4f electron shell with stable structure, so the sample with rare earth ions has high thermal stability. Due to the larger bond energy of Ho^{3+}–O^{2-}as compared with that of Fe^{3+}–O^{2-}, it is obvious that more energy is needed to make Ho^{3+} ions enter into lattice and form the bond of Ho^{3+}– O^{2-}. Bond energy is a part of inner energy. During the process of bond break or formation, inner energy will be changed in the chemical reaction. If the bulk work is small enough and can be neglected, the variation of enthalpy will be equal to the variation of inner energy. The variation of bond energy will directly lead to the variation of enthalpy. So the increase of bond energy will induce the increase of inner energy, i.e. more energy is needed to form the bond of Ho^{3+}–O^{2-}. The higher thermal stability of the Ho^{3+} substituted samples relatives to cobalt ferrite, and hence more energy is needed for the Ho^{3+} substituted samples to complete crystallization and growth of grains. In addition, the formed $HoFeO_3$ phase pinning at the grain boundary will hinder the growth of ferrite grains, resulting in smaller ferrite gains and thus denser samples.

The TEM micrograph of the synthesized Ho substituted $CoFe_2O_4$ ferrite nanoparticles are shown in Fig. 4.6 showing almost homogeneous and uniform distribution of the particles in this powder sample. The particles are consisted of some regular and irregular polyhedrons with mean sizes of about 34 nm (x = 0.0) and 41 nm (x = 0.075) much larger than the size obtained from XRD data. The particles tend to agglomerate because they experience a permanent magnetic moment proportional to their volume. The TEM images of sample show that the particles are aggregated and the average value of the nanocrystalline samples are consistent with the result from XRD according to the Scherrer formula. The bright fringes observed from the corresponding SAED patterns (Fig. 4.7) of the selected region indicate that the samples are crystallized. The SAED patterns indicate that Ho^{3+}substituted ferrite nanoparticles were found in well-crystalline nature. The superimposition of the bright spot with Debye ring pattern indicates polycrystalline

nature of the sample.

The bulk density 'd_B' of the specimens has been determined by the hydro-static method. The variation of the bulk density is shown in Fig. 4.8 and the values are depicted in Table 4.1.The bulk density increased from 4.352 (x = 0.0) to 4.599 (x =0.1) with increase in Ho^{3+} substitution. One possible reason for the increasing densities is that the introduction of Ho^{3+}ions produced smaller ferrite grains, thus resulting in denser samples, which was quite in agreement with the changes in the percentage shrinkages of diameter, and relative densities of the samples. Another reason for the increasing densities is the formation of foreign phase $HoFeO_3$.

The percentage porosity is calculated using the following relation:

$$P = \left(\frac{d_X - d_B}{d_X} \right) \times 100 \qquad \textbf{4.5}$$

where dx and d_B are the X-ray density and bulk density respectively. Table 4.1 and Fig. 4.8 shows that the porosity decreased with an increase in Ho^{3+} substitution. The decrease in porosity is related to increase in bulk density.

Using the experimental values of lattice constant '*a*', oxygen positional parameter '*u*' (0.375 Å) and substituting using the following equations, the allied parameters such as tetrahedral and octahedral bond length (d_{Ax} and d_{Bx}), tetrahedral edge, shared and unshared octahedral edge (d_{AXE}, d_{BXE} and d_{BXEU}) were calculated.

$$d_{Ax} = a\sqrt{3}\,(u-1/4) \qquad \textbf{4.6}$$

$$d_{Bx} = a\,[3u^2-(11/4)u+43/64)]^{1/2} \qquad 4.7$$

$$d_{AxE} = a\sqrt{2}\,(2u-1/2) \qquad \textbf{4.8}$$

$$d_{BxE} = a\sqrt{2}(1-2u) \qquad \textbf{4.9}$$

$$d_{BxEu} = a\,[4u^2 - 3u + (11/16)]^{1/2} \qquad \textbf{4.10}$$

Figure 4.9 and Table 4.2 show that all the allied parameter increased with an increase in Ho^{3+} substitution. The variation of allied parameters is related to the difference in the ionic radii of Ho^{3+} and Fe^{3+}. The Ho^{3+} ion with the larger ionic radii increases the allied parameter as the replaces Fe^{3+} ions of smaller ionic radii. The hopping length for A-site (L_A) and B-sites (L_B) are calculated using the values of lattice constant.

$$L_A = a\sqrt{\frac{3}{4}} \quad \textbf{4.11}$$

$$L_B = a\sqrt{\frac{2}{4}} \quad \textbf{4.12}$$

The variation of hopping lengths with Ho^{3+} content *x* is shown in Table 4.3 and Fig. 4.10 It is observed from Fig. 4.10 that the distance between the magnetic ions (hopping length) Ho^{3+}increases as Ho^{3+} substitution increases. This behavior of hopping length with *x* is analogous with the behavior of lattice constant with Ho^{3+} substitution. This variation may be attributed to the difference in the ionic radii of the constituent ions, which makes the magnetic ions become larger to each other and the hopping length increased.

4.3.2 Infrared Spectroscopy

The room temperature IR spectra of the all the composition are shown in Fig. 4.11. The spectra are recorded in the range from 300 to 800 cm^{-1}. The band positions for all the investigated composition are given in Table 4.4. The spectra show two main absorption bands $\upsilon_1$and$\upsilon_2$as a common feature of all the ferrites. The high-frequency band υ_1 lies in the range702-725 cm^{-1} while the low-frequency band υ_2 is varying in the 486-497 cm^{-1} range. The difference in the band position is expected because of the difference in Fe^{3+}- O^{2-}distance for the octahedral and tetrahedral compounds. From the IR spectra it is noticed that the frequency $\upsilon_1$and $\upsilon_2$areslightly shifted with an increasing Ho^{3+}concentration and consequently with decreasing Fe ions concentration. Waldron [84] studied the vibration spectra of ferrites and attributed the υ_1 band to the intrinsic vibrations of the tetrahedral groups and υ_2 band to the octahedral groups. Thus, the replacement of La^{3+} with Fe^{3+} ions (having larger ionic radius and higher atomic weight than Fe^{3+}) at octahedral site in the ferrite lattice affects the Fe^{3+}- O^{2-}stretching vibration. This may be reason for the observed change in υ_1 and υ_2 band positions.

4.3.3 Cation Distribution

The cation distribution in spinel ferrite can be obtained from the analysis of X-ray diffraction pattern. In the present work, the Bertaut method [101] is used to determine the cation distribution. This method selects a few pairs of reflections according to the expression:

$$\frac{I_{hkl}^{Obs.}}{I_{h'k'l'}^{Obs.}} = \frac{I_{hkl}^{Calc.}}{I_{h'k'l'}^{Calc.}} \qquad \textbf{4.13}$$

where $I_{hkl}^{Obs.}$ and $I_{hkl}^{Calc.}$ are the observed and calculated intensities for reflection (hkl), respectively. The best information on cation distribution is achieved when comparing experimental and calculated intensity ratios for reflections whose intensities (i) are nearly independent of the oxygen parameter, (ii) vary with the cation distribution in opposite ways and (iii) do not differ significantly.

The distribution of divalent and trivalent cations among octahedral and tetrahedral sites in the presently investigated samples were determined from the ratio of XRD lines I_{220}/I_{440} and I_{422}/I_{400}.These planes are assumed to be sensitive to the cation distribution. The temperature and absorption factors are not taken into account in our calculations as they do not affect the intensity calculation. If an agreement factor (R) is defined as in Eq. (4.14), the best-simulated structure which matches the actual structure of the sample will lead to a minimum value of R and the corresponding cation distribution is obtained for each hkl and $h'k'l'$ reflection pair considered:

$$R = \left| \left(\frac{I_{hkl}^{Obs.}}{I_{h'k'l'}^{Obs.}} \right) - \left(\frac{I_{hkl}^{Calc.}}{I_{h'k'l'}^{Calc.}} \right) \right| \qquad \textbf{4.14}$$

For the calculation of the relative integrated intensity (I_{hkl}) of a given diffraction line from powder specimens as observed in a diffractometer with a flat-plate sample holder, the following formula is valid,

$$I_{hkl} = |F|_{hkl}^2 P L_P \qquad \textbf{4.15}$$

where F is the structure factor, P is the multiplicity factor, L_P is the Lorentz-polarization factor and

$$L_P = \frac{1+cos^2 2\theta}{sin^2\theta cos\theta} \quad \textbf{4.16}$$

The atomic scattering factors for various ions were taken from the literature [99].

It should be added that the calculated integrated intensities are valid at 0 K. Because the observed values are obtained at room temperature, a suitable correction is in principle necessary for precise comparison. However, the spinels are high-melting compounds, the thermal vibration of the atoms at room temperature should not differ greatly from that at absolute zero. Therefore, in our intensity calculations no temperature correction was deemed necessary.

The cation distribution from in above mentioned way is listed in Table 4.5. It is observed from table 4.5 that the Ho^{3+} ions show a preference for octahedral sites. It is to be noted that the radius of the octahedral site is larger than that of tetrahedral site in the spinel lattice. As mentioned earlier the ionic radius of the Ho^{3+} ion is 1.04 Å which could be large for tetrahedral A site and therefore these larger Ho^{3+} ions occupy octahedral site. It can also be assumed that the small amount of Ho^{3+}cations substituted for Fe^{3+} cations which enter into the octahedral sites by rearrangement of cations between the tetrahedral and octahedral sites to minimize the free energy of the system. It is also observed that Co^{2+} ion initially occupy only octahedral sites, but as the Ho^{3+} concentration increased Co^{2+} ions occupied tetrahedral A site as well. Partial migration of Co^{2+} ions (0.78Å) from B to A sites has been observed by increasing the Ho^{3+} concentration accompanied by an opposite transfer of equivalent number of Fe^{3+} ions (0.67Å) from A to B sites in order to relax the strain at the octahedral sites [102].

The mean ionic radius of the tetrahedral A- and octahedral B-sites (r_A and r_B) was calculated for all the samples using the relations discussed elsewhere [103, 104]. The values are given in Table 4.6 and its variation is shown in Fig. 4.12. It is observed from Fig. 4.12 that both r_A and r_B increased with an increase in Ho^{3+} substitution. The increase in r_B is due to the occupancy of larger Ho^{3+} (1.04 Å) at octahedral B site which replaced smaller Fe^{3+}(0.67 Á) ions. The site ionic radii of tetrahedral A-site (r_A) initially remain constant and it increased for $x \geq 0.075$. The increase in $r_A$for $x \geq 0.075$ is due to the migration of Co^{2+} ions from B site to A site.

The theoretical values of lattice parameter (a_{th}) were calculated using the following equation [105]:

$$a_{th} = \frac{8}{3}\sqrt{3}\left[(r_A + R_0) + \sqrt{3}(r_B + R_0)\right] \quad \textbf{4.17}$$

where r_A and r_B are radii of tetrahedral (A) site and octahedral [B] site, R_O is radius of oxygen i.e. (R_O = 1.32 Å). The variations of theoretical lattice parameter are shown in Table 4.6 and Fig. 4.13. It is observed theoretical lattice constant increased with increase in Ho^{3+} substitution. This variation is similar to that observed for experimentally determined lattice parameter (a).

Using the values of 'a', the radius of oxygen ion R_O= 1.32 Á and 'r_A' in the following expression, the oxygen positional parameter '*u*' was calculated [21]:

$$u = \left[(r_A + R_0)\frac{1}{\sqrt{3a}} + \frac{1}{4}\right] \quad \textbf{4.18}$$

As discussed earlier the *A* site is smaller in size than the *B* sites. *A* site is unable to accommodate available cations without local distortion of the sites. Thus each *A* site expands by an equal displacement of the four surrounding oxygen ions, towards and along the body diagonal of the cube, to form a tetrahedral with an *A*−ion having cubic symmetry. However, six oxygen ions surrounding a B site are shifted in such a way that this oxygen octahedral shifts by the same amount, as the first expands. A quantitative measure of this displacement is the oxygen positional parameter *u*, given by a distance between an oxygen ion and a face of a cube. The ideal FCC parameter is *u* = 3/8 = 0.375, where the packing of ions, within the lattice, is taken as perfect. However, slight deviation from the perfect value may occur due to relatively larger oxygen ion which causes a small distortion of the lattice structure to make space for the cations at the available interstitial sites in the unit cell. The oxygen atom in the spinel structure is not generally located at the exact FCC sub lattice. Their detailed positions are deformed as given by the *u* parameter, which reflect adjustment of the structure to accommodate differences in the radius ratio of the cation in *A* and *B* sites [106].Figure 4.13 and Table 4.6 shows the variation of oxygen positional parameter '*u*' with Ho^{3+} substitution. In most oxide spinels the oxygen ions are apparently larger than the metallic ions. Our value of '*u'* is larger than its ideal value (*u* = 0.375 Å), this larger value may probably be due to many reasons, including the history of the samples,

experimental or measurement errors, e.g. precision of the observed X-ray intensity and the theoretical data used for the scattering model of the system.

4.3.4 Magnetization

In the present work to tailor the magnetic properties of the cobalt ferrite, Fe^{3+} ions are partially substituted by trivalent ions of rare earth element Ho^{3+}, aiming to occupy the spin down sites and, consequently, to increase the net magnetization. Magnetic measurements of Ho^{3+} substituted $CoFe_2O_4$ ferrite nanoparticles were carried out at room temperature using pulse field hysteresis loop technique with a peak field of 9 kOe and the hysteresis loops are shown in Fig. 4.14 As it can be seen, the variation of magnetization as a function of applied field presents a wide cycle and the observed hysteresis loops are characteristic behavior of hard magnetic material. The values of saturation magnetization (Ms), remanence magnetization (Mr), coercivity (Hc) and magneton number (n_B) obtained from magnetization plots are given in Table 4.7. The effect of rare earth element Ho^{3+} substitution on the magnetic properties of the material is in general a positive one. It is observed from Figs 4.14 and 4.16 that magnetization increased with an increase in Ho^{3+} substitution because of larger magnetic moment of Ho (10.6 μ_B) than Fe (5μ_B). The magnetic moment in the case of the Ho^{3+} is 10.6 μ_B and generally originated from the localized 4*f* electrons. Therefore, the effect of Ho^{3+}ions in the cobalt ferrite materials seems to be similar to the substitution of magnetic ions in the octahedral Fe sites of the spinel lattices.

In spinel ferrite the saturation magnetization is dominated by the superexchange interactions between the tetrahedral (A-sites) and octahedral (B-sites) sites cations. According to Neel's molecular-field model [107], the A-B super exchange interaction predominate the intrasublattice A-A and B-B interactions. Therefore, the net magnetic moment is given by the sum of the magnetic moments of the A and B sublattices. The magnetic moment per formula unit (n_B) was calculated from Neel's sub-two-lattice model using the relation,

$$n_{Bcal.} = M_B - M_A \qquad \textbf{4.19}$$

where M_B and M_A are the B and A sub-lattice magnetic moments in μ_B. The variation of $n_{Bcal.}$ with Ho^{3+} substitution is shown in Fig. 4.15. According to the

cation distribution (Table 4.5) Co^{2+} ($3\mu_B$) ions mostly contribute to the B-site sublattice magnetization, Ho^{3+} (10.6 μ_B) ions contribute only to the B-site sublattice magnetization whereas Fe^{3+} (5 μ_B) contribute equally to A and B site sublattice magnetization. The preferential occupancy of Ho^{3+} ions at the octahedral B-sites in the $CoFe_2O_4$ spinel will result in decreasing the concentration of Fe^{3+} ions in these sites and resulted into the increase of net magnetic moment. The increase in magnetization with the increasing Ho^{3+} content means that the $Fe_A^{3+} - O^{2-} - Ho_B^{3+}$ superexchange interaction is stronger than the $Fe_A^{3+} - O^{2-} - Fe_B^{3+}$ interaction. The increase in *Ms* and consequently n_B could also be contributed by the enhancement of hyperfine fields at 12*k* and 2*b* sites [108].It is also worth to mention here that while $CoFe_2O_4$ was substituted by an amount of Ho^{3+} ions, the interaction between the spins of the Ho^{3+} ion and theFe^{3+} ion, which, to some extent, decouples the antiferromagnetic interactions between the Fe^{3+} ions and thus provides a significant enhancement of the magnetization.

The observed magnetic moment per formula unit in the Bohr magneton (μ_B) was calculated using a relation 4. 20

$$n_B = \frac{Molecular\ weight\ (Mw) \times saturation\ magnetization\ (Ms)}{5585} \qquad \textbf{4.20}$$

It is obvious from Table 4.7 and Fig. 4.15 that the calculated and observed values of the magneton number are in good agreement with each other.

Remanence magnetization (Mr) increased from 28.5 to 34.6 emu/g with Ho^{3+} substitution (Table 4.7). Remanence ratio (R), i.e. Mr/Ms is calculated for Ho^{3+} substituted $CoFe_2O_4$ nanoparticles. Table 4.7 shows that R is ranging from 0.451 to 0.467 which is well below the typical value~1 for single domain isolated ferromagnetic particles. The remanence ratio is~0.5 for randomly oriented uniaxial anisotropic ferromagnetic particles [109]. The deviation of R from typical single domain class value may be assigned to the interaction amongst the grains which are affected by the core–shell structure of grains and grain size distribution in material. The observed remanence ratio is well agreed to the values of single domain or pseudo-single domain particles of other chemical routed RE doped $CoFe_2O_4$ samples [110].

The anisotropy constant (K) can be calculated using following relation and assuming the magnetic particles to be isolated (exchange interacting spin) single domains,

$$K = \frac{HcMs}{2}$$

The values of K listed in table 4.7 are much higher than that of previously reported RE-$CoFe_2O_4$ [111]. This shows that grains are not single domains and anisotropy contribution is not uniaxial, but it may be cubic magneto-crystalline anisotropy and hence strong grain to grain interactions exist in these materials.

Coercivity (Hc) of $CoFe_2O_4$ increased with the increase in Ho^{3+} substitution (Fig. 4.16).The coercivity increases with Ho^{3+} substitution that may be due to the enhancement of magneto crystalline anisotropy with anisotropic Fe^{2+} ions located on 2 A sites as usually found in rare earth substitution and this happens due to elevated sintering temperature [112].The coercivity increase with the increase of Ho substitution. It is observed that Hc is inversely proportional to the packing of magnetic materials or the grain size that is $Hc \propto 1/r$. It is also to be noted that the coercivity is a microstructure property. It depends upon defects, surface effect, strains, non-magnetic atoms, etc. in the material [113]. The coercive force variation of the system shows a typical size dependent behavior. This behavior can be attributed to the combination of surface effect and its surface anisotropy [114]. The electronic configuration of Ho^{3+} ions results in the lattice or crystalline field distortion, and generates an internal stress. Also, the strong spin-orbit coupling of rare earth Ho^{3+} ions may contribute to the anisotropy, when they are located in the B sites of ferrite [115]. This might also one of the reasons to increase the coercivity of the samples with Ho^{3+} substitution.

Table 4.1 Lattice constant (a), X-ray density (d_x), crystallite size (D_{XRD}), specific surface area (S), bulk density (d_B) and porosity (P) of $Ho_xCoFe_{2-x}O4$

Comp. x	a (Å)	dx (g/cm^3)	D_{XRD} (nm)	S (m^2/g)	d_B (g/cm^3)	P (%)
0.000	8.355	5.345	32.1	42.95	4.352	18.58
0.025	8.363	5.392	34.8	39.19	4.399	18.41
0.050	8.372	5.436	37.9	35.42	4.469	17.79
0.075	8.379	5.484	39.7	33.43	4.521	17.56
0.100	8.383	5.536	32.1	40.64	4.599	16.92

Table 4. 2 Tetrahedral bond (d_{AX}), octahedral bond (d_{BX}), tetra edge (d_{AXE}) and octahedral edge (d_{BXE}) (shared and unshared) of $Ho_xCoFe_{2-x}O4$

Comp. x	d_{AX} (Å)	d_{BX} (Å)	Tetra edge (Å)	Octa edge d_{BXE} (Å)	
			d_{AXE}	Shared	unshared
0.000	1.8957	2.0397	3.0955	2.8120	2.9555
0.025	1.8964	2.0405	3.0967	2.8130	2.9565
0.050	1.8977	2.0420	3.0989	2.8150	2.9587
0.075	1.9018	2.0463	3.1056	2.8211	2.9650
0.100	1.9034	2.0480	3.1081	2.8234	2.9675

Table 4.3 Hopping lengths(L_A and L_B) of $Ho_xCoFe_{2-x}O4$

Comp. x	Hopping length	
	L_A (Å)	L_B (Å)
0.000	3.6176	2.9538
0.025	3.6211	2.9566
0.050	3.6250	2.9598
0.075	3.6280	2.9623
0.100	3.6301	2.9640

Table 4.4 IR absorption bands of $Ho_xCoFe_{2-x}O4$

Comp. x	ν_1 (cm^{-1})	ν_2 (cm^{-1})
0.000	725	497
0.025	708	499
0.050	714	491
0.075	702	496
0.100	725	486

Table 4.5 Cation distribution of $Ho_xCoFe_{2-x}O4$

Comp. x	**Cation distribution**
0.000	$(Fe)^A [CoFe]^B O_4$
0.025	$(Fe)^A [CoHo_{0.025}Fe_{0.975}]^B O_4$
0.050	$(Fe)^A [CoHo_{0.05}Fe_{0.95}]^B O_4$
0.075	$(Co_{0.05}Fe_{0.95})^A [Co_{0.95}Ho_{0.075}Fe_{0.975}]^B O_4$
0.100	$(Co_{0.05}Fe_{0.95})^A [Co_{0.95}Ho_{0.1}Fe_{0.95}]^B O_4$

Table 4.6 Ionic radii of tetrahedral A-site (r_A), octahedral B-site (r_B), theoretically lattice constant (a_{th}) and oxygen positional parameter (u) of $Ho_xCoFe_{2-x}O4$

Comp. 'x'	r_A (Å)	r_B (Å)	a_{th} (Å)	u (Å)
0.000	0.670	0.725	8.518	0.3849
0.025	0.670	0.730	8.530	0.3847
0.050	0.670	0.734	8.543	0.3845
0.075	0.676	0.736	8.556	0.3847
0.100	0.676	0.741	8.569	0.3845

Table 4.7 Saturation magnetization (M_s), remanence magnetization (Mr), remanence ratio (R), magneton number (η_B), anisotropy constant (K) and coercivity (H_C) of $Ho_xCoFe_{2-x}O4$

Comp. x	M_s (emu/g)	M_r (emu/g)	R	η_B (μ_B)		K (erg/cm^3)	H_C (Oe)
				Obs.	Cal.		
0.000	61.06	28.5	0.467	2.57	3.0	38743	1269
0.025	65.19	29.8	0.457	2.77	3.14	45144	1385
0.050	66.96	30.9	0.461	2.88	3.28	49651	1483
0.075	71.10	32.1	0.451	3.09	3.62	56560	1591
0.100	74.05	34.6	0.467	3.26	3.76	55241	1492

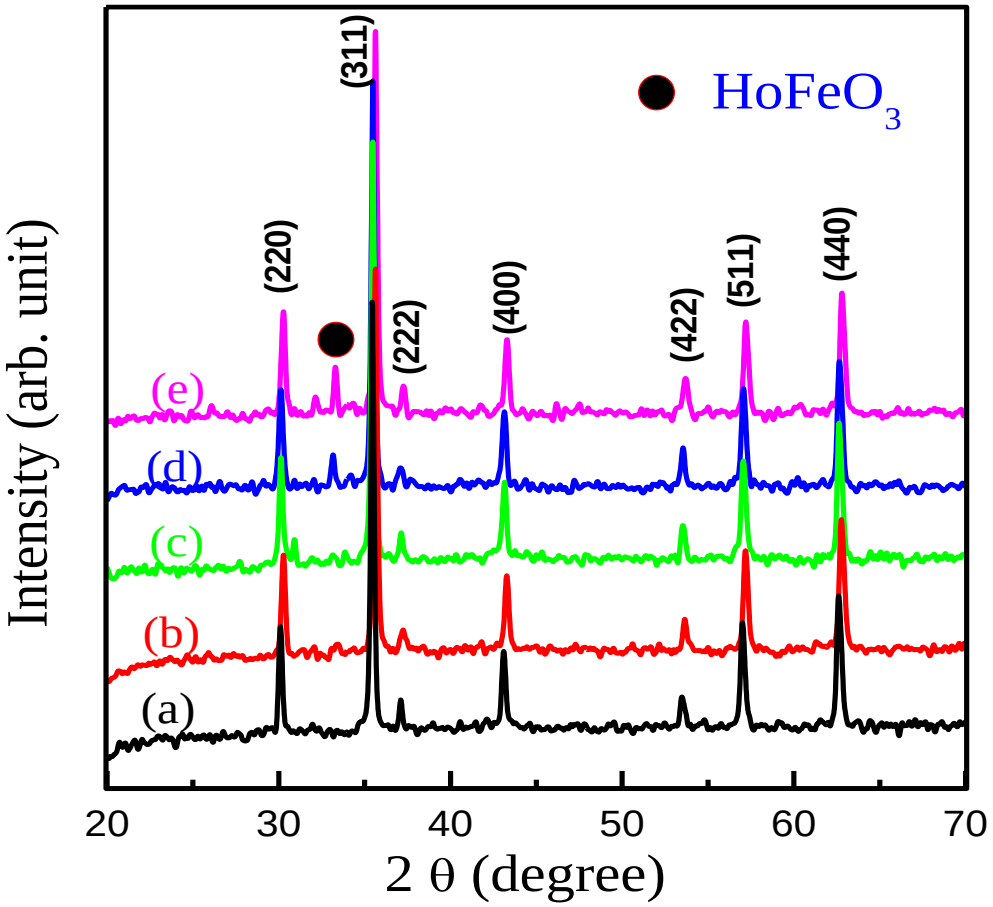

Fig. 4.1: X-Ray diffraction patterns of (a) x = 0.0, (b) x = 0.025, (c) x = 0.050, (d) x = 0.075 and (e) x = 0.1 for $Ho_xCoFe_{2-x}O_4$

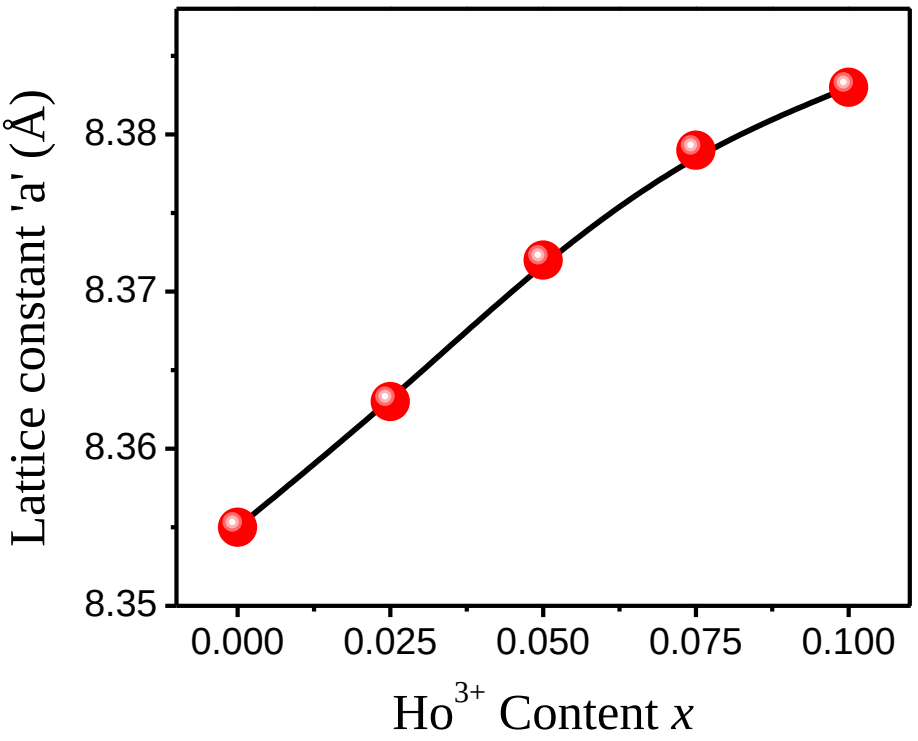

Fig. 4.2: Variation of lattice constant with Ho^{3+} content x

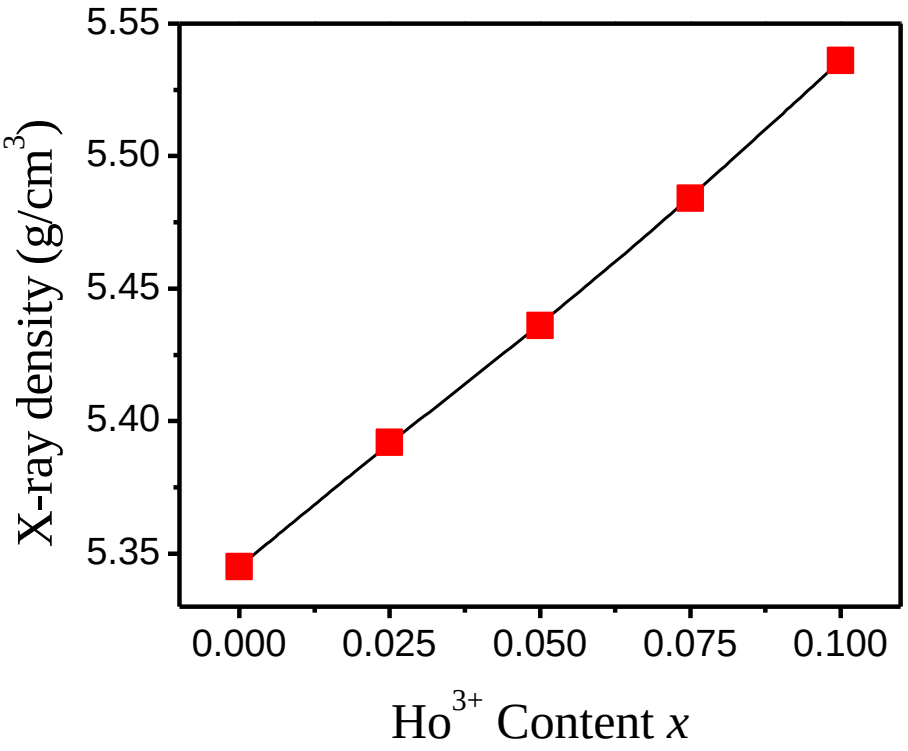

Fig. 4.3: Variation of X-ray density with Ho^{3+} content x.

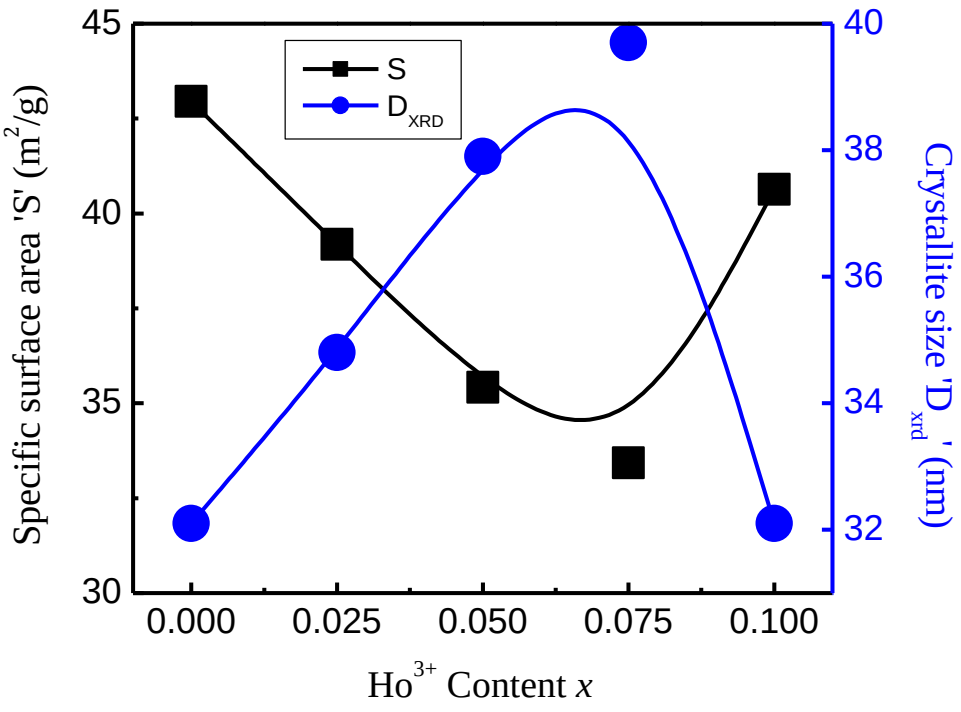

Fig. 4.4: Variation of specific surface area (S) and crystallite size (D_{xrd}) with La substitution of $Ho_xCoFe_{2-x}O_4$

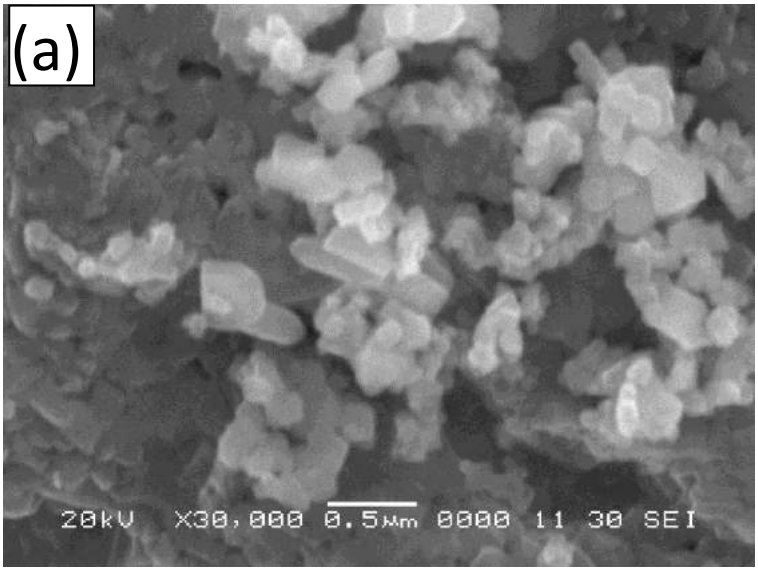
(a)
20kV X30,000 0.5µm 0000 11 30 SEI

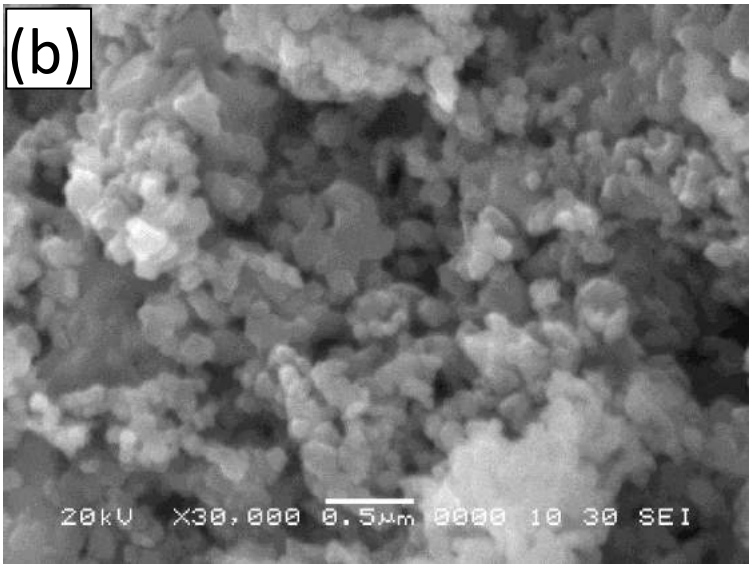
(b)
20kV X30,000 0.5µm 0000 10 30 SEI

=

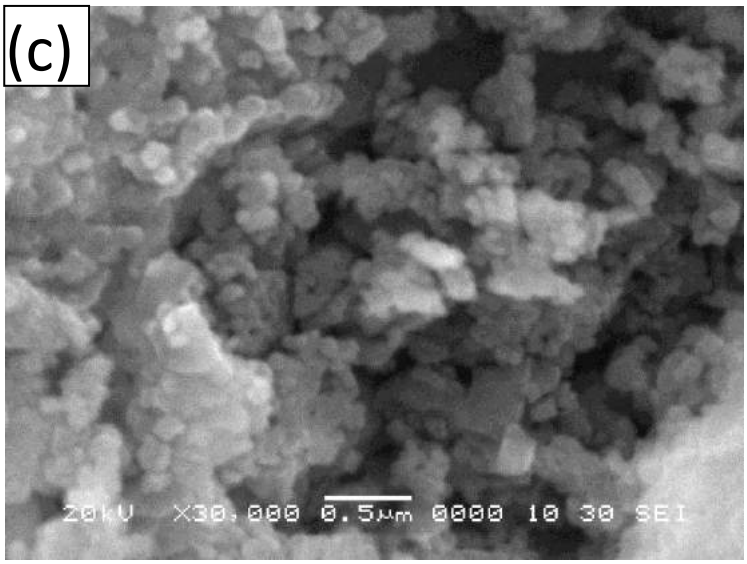

Fig. 4.5. (a) = 0.0, (b) = 0.025 and (c) = 0.05,

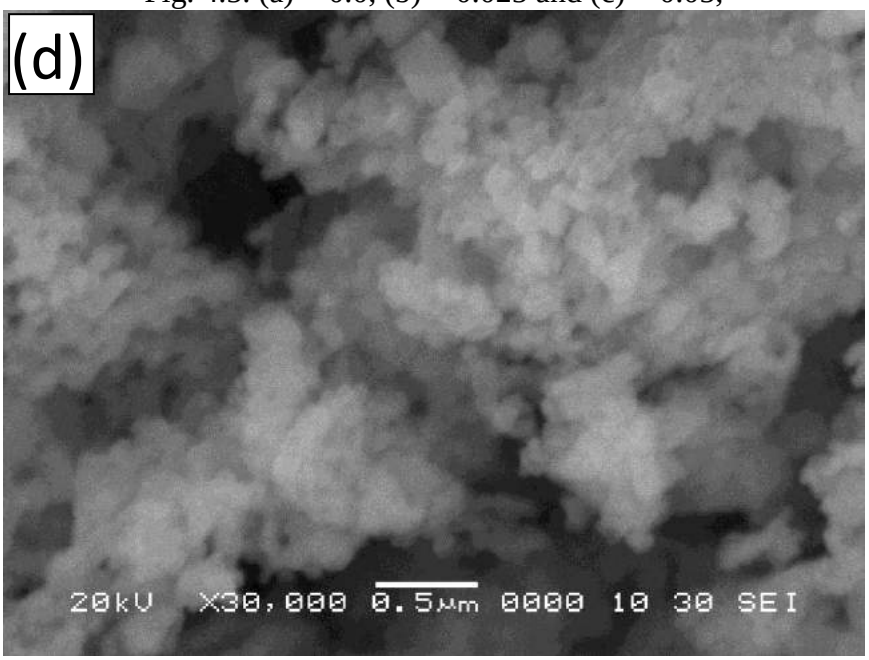

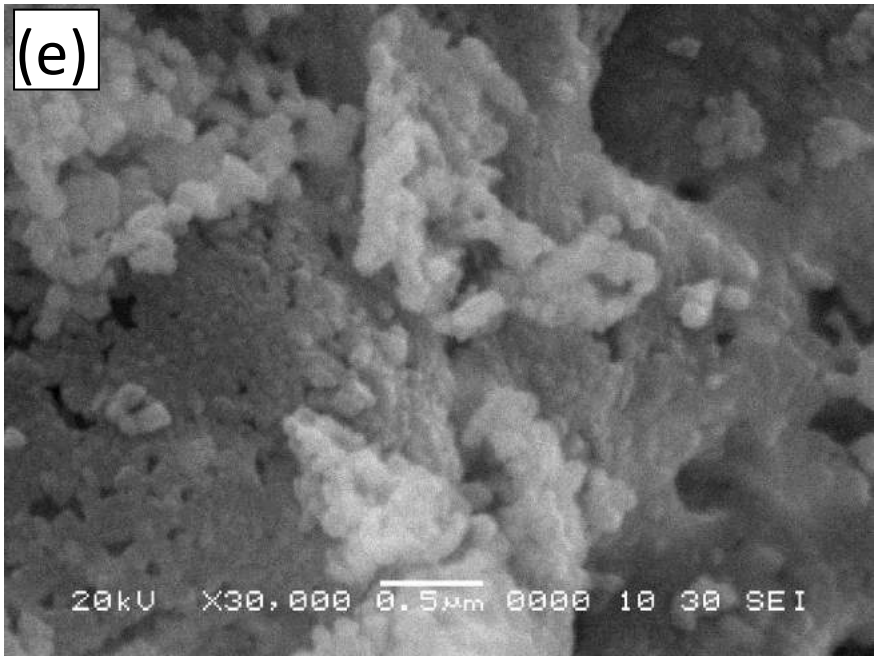

Fig. 4.5. (d) = 0.075 and (e) = 0.1

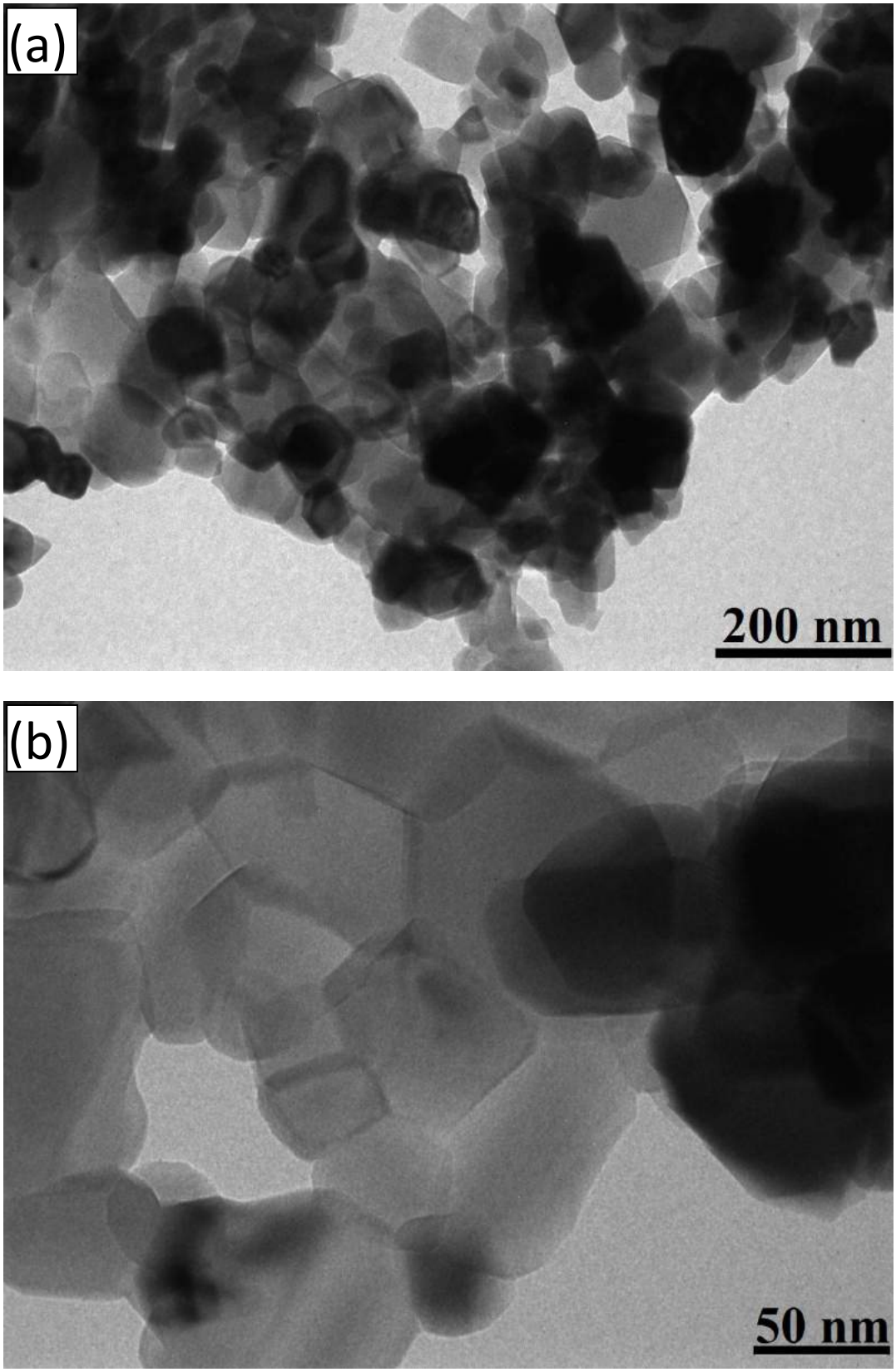

Fig. 4.6: TEM images of (a) x = 0.0 and (b) x = 0.075

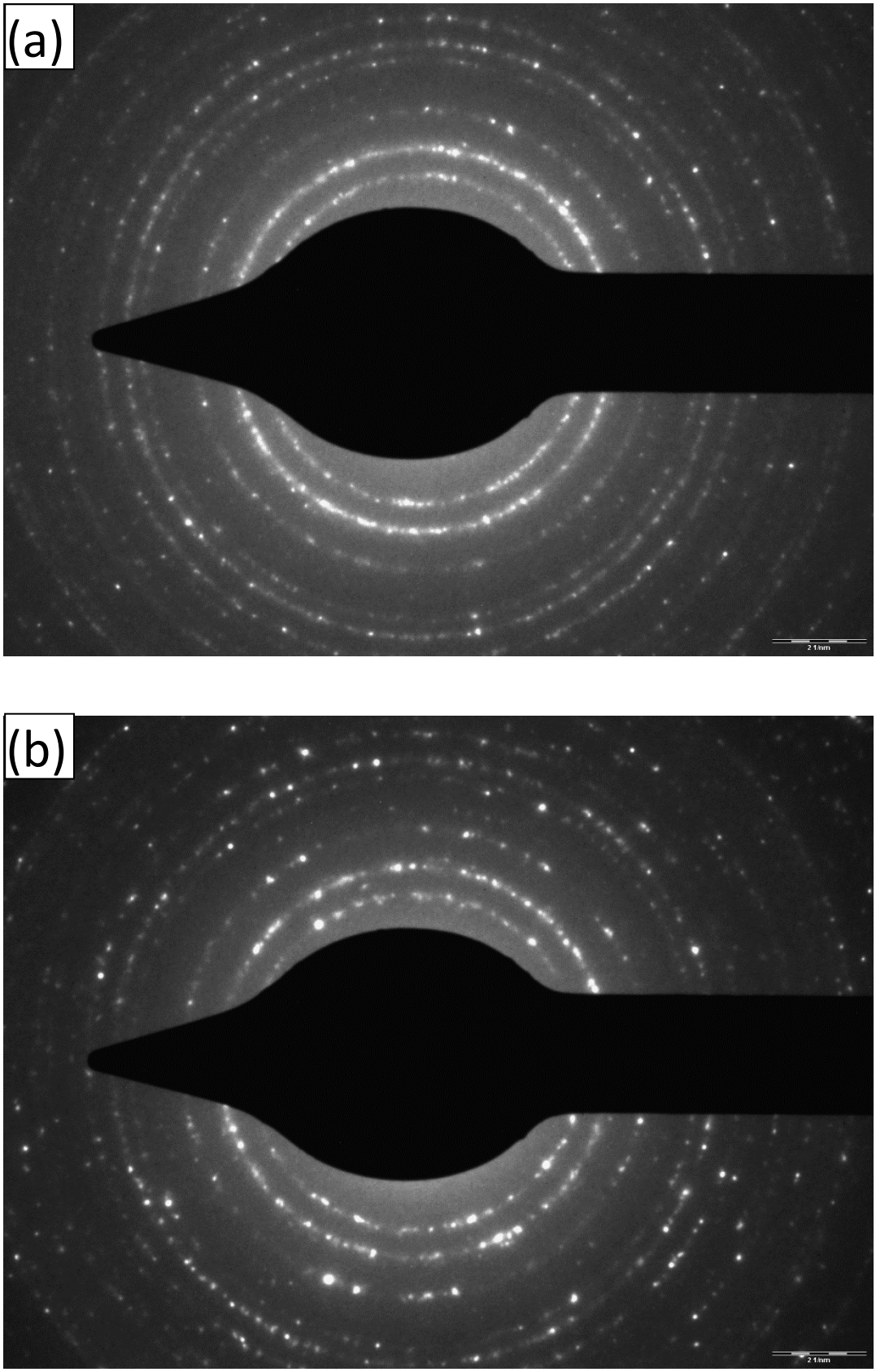

Fig. 4.7: SAED images of (a) x = 0.0 and (b) x = 0.075

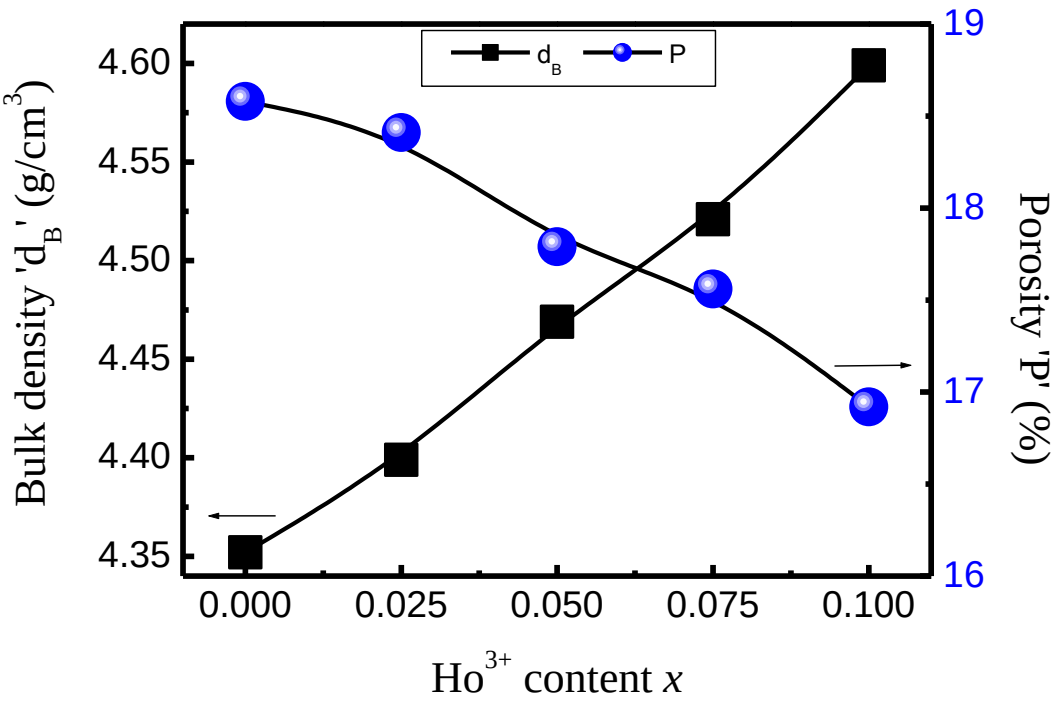

Fig. 4.8: Variation of bulk density (d_B) and porosity (P) with Ho^{3+} content x.

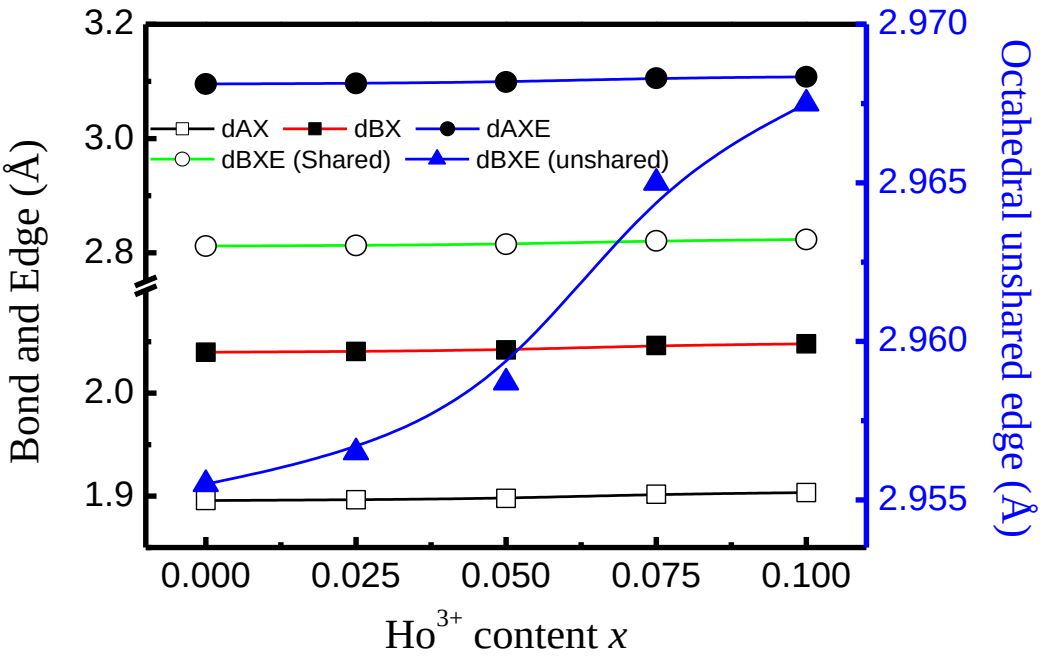

Fig. 4.9: Variation of Tetrahedral bond (d_{AX}), octahedral bond (d_{BX}), tetra edge (d_{AXE}) and octahedral edge (d_{BXE}) (shared and unshared) with Ho^{3+} content x of $Ho_xCoFe_{2-x}O_4$

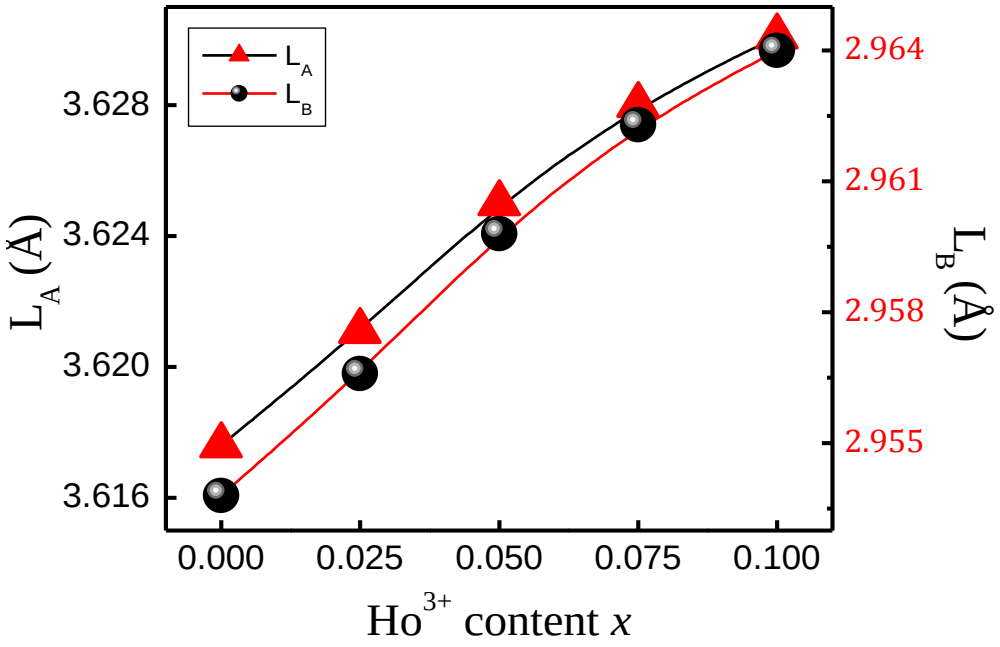

Fig. 4.10: Variation of ion jump lengths (L_A and L_B) with Ho^{3+} substitution of $Ho_xCoFe_{2-x}O_4$

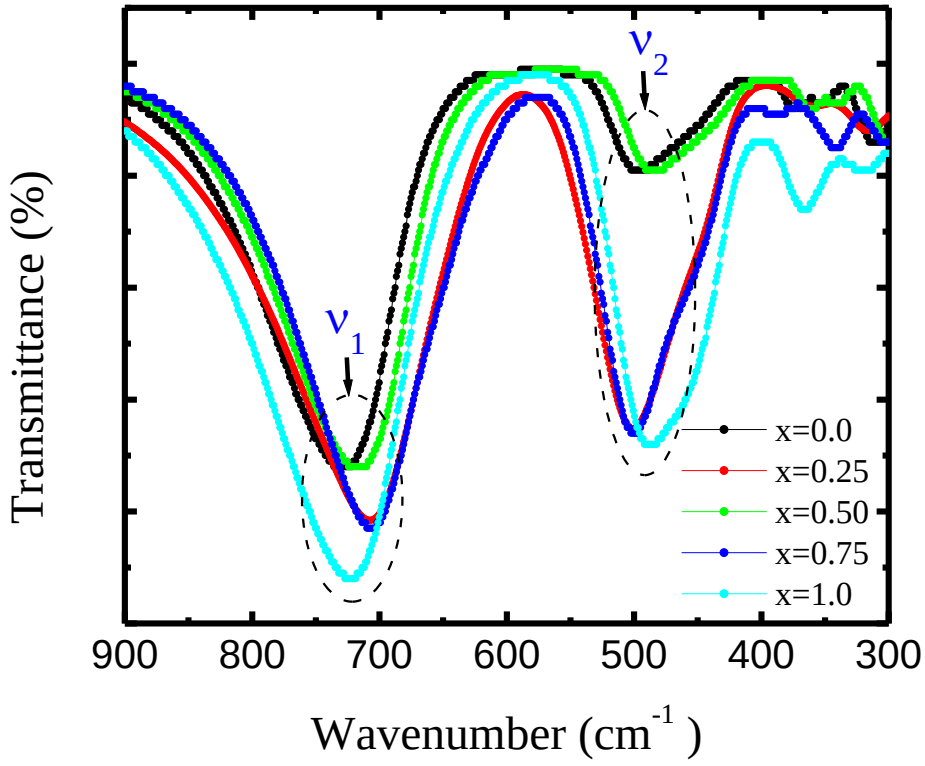

Fig. 4.11: Infrared spectra of $Ho_xCoFe_{2-x}O_4$.

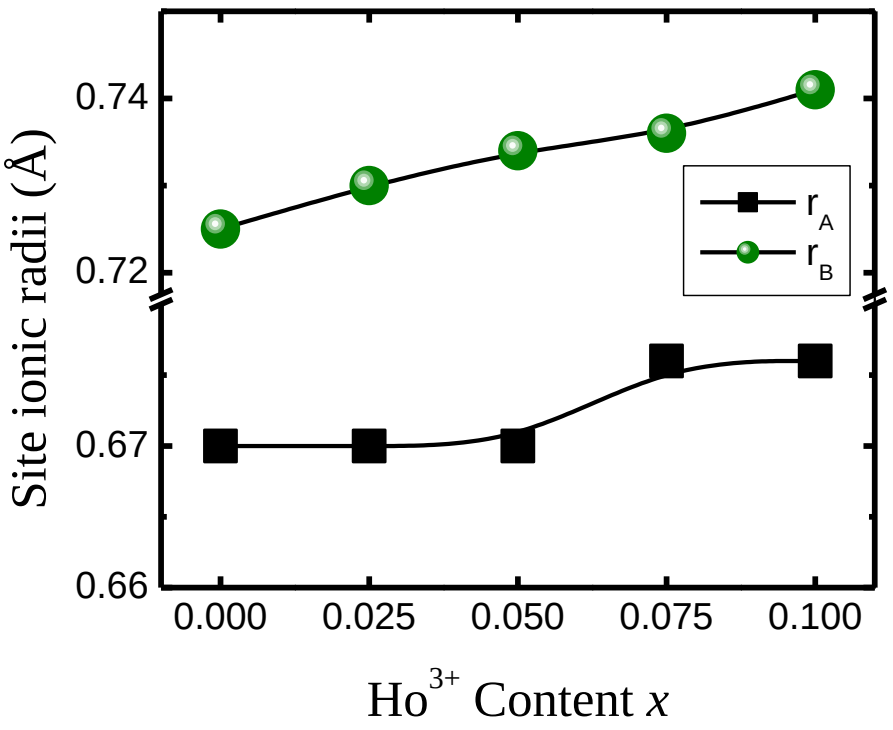

Fig. 4.12: Variation of site ionic radii (r_A and r_B) with Ho^{3+} content x.

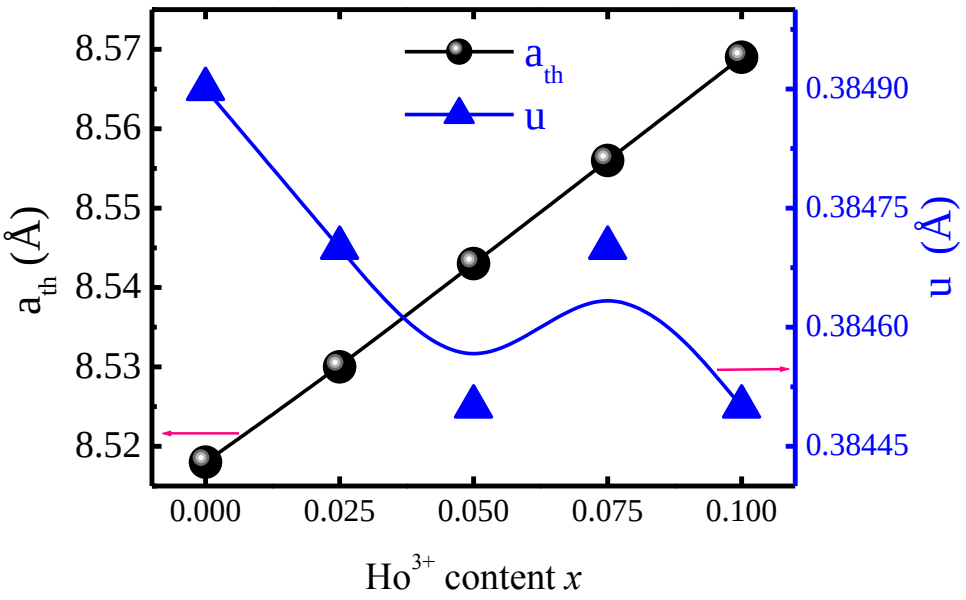

Fig. 4.13: Variation of theoretical lattice constant (a_{th}) and oxygen parameter (u) with Ho^{3+} content x.

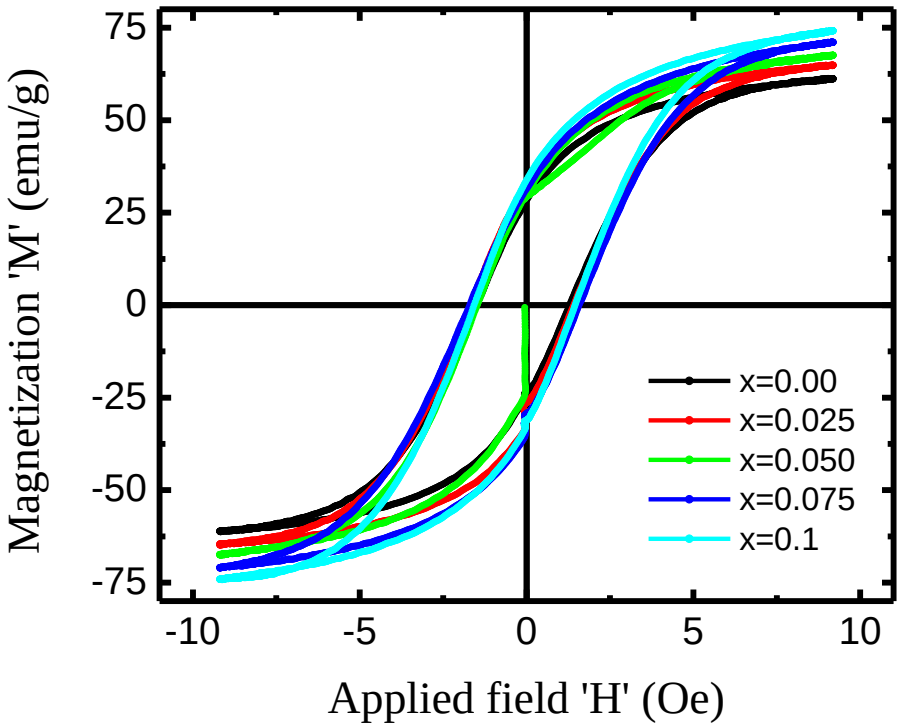

Fig. 4.14: Variation of magnetization (M) with applied field (H).

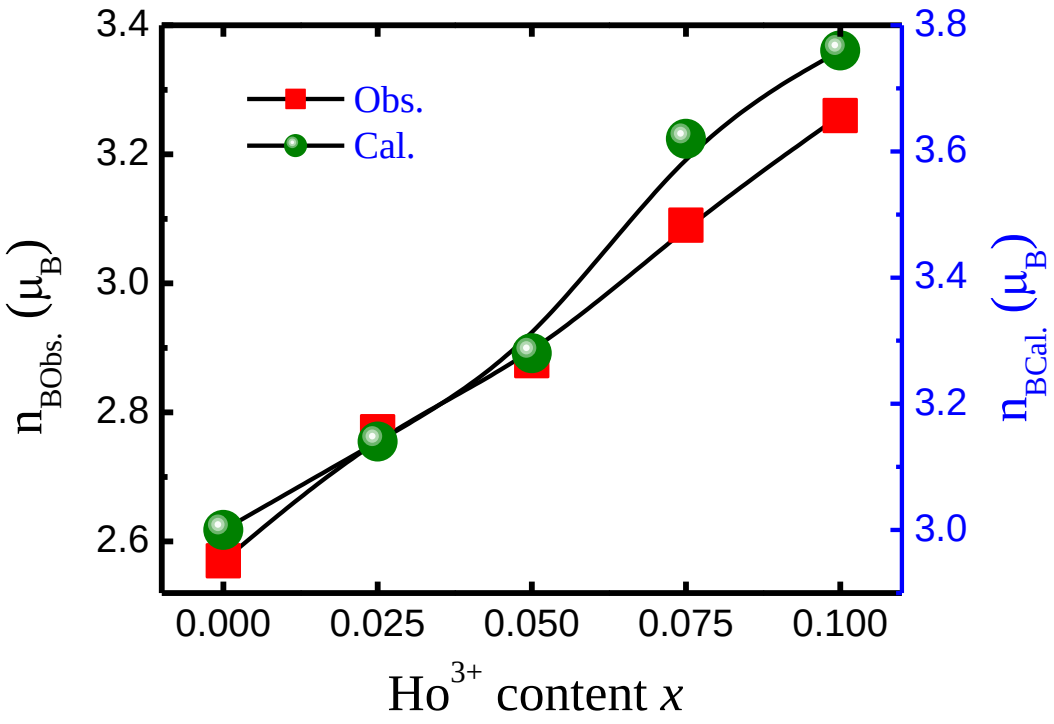

Fig. 4.15: Variation of observed (Obs.) and calculated (Cal.) magneton number with Ho^{3+} content x.

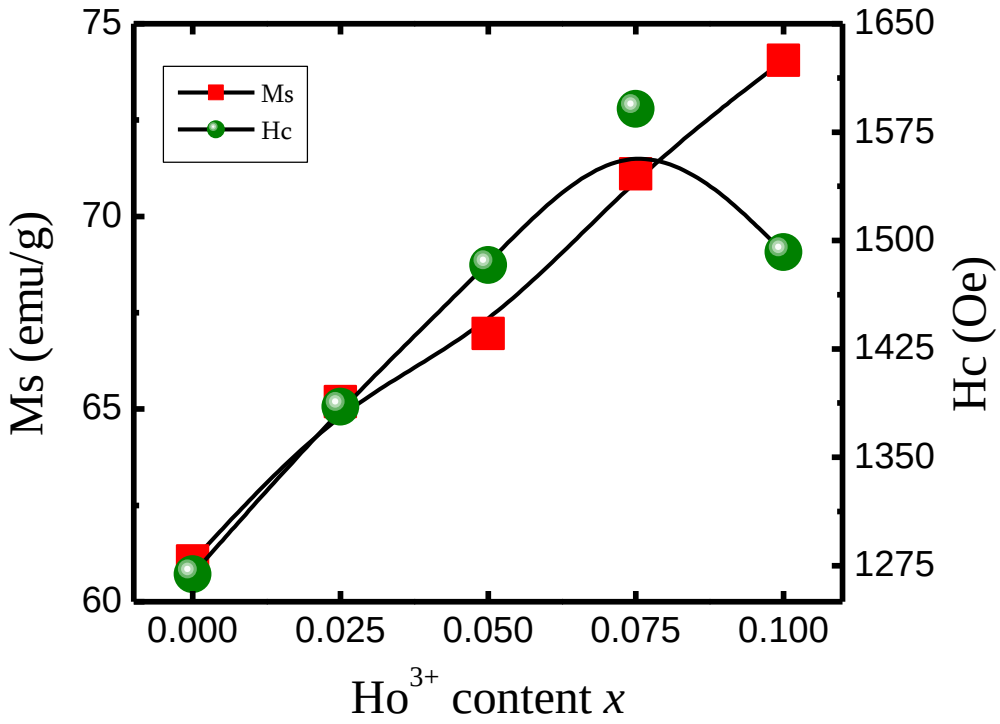

Fig. 4.16: Variation of magnetization (Ms) and coercivity (Hc) with Ho^{3+} content x.

Chapter # 5

Results and Discussion on $Pr_xCoFe_{2-x}O_4$ Ferrite System

5.1 Introduction

There is an increasing interest in magnetic ferrite nanoparticles because of their broad applications in several technological fields including permanent magnets, magnetic fluids, magnetic drug delivery, microwave devices, and high density information storage [116,117]. Chemically prepared magnetic nanoparticles exhibit superior magnetic properties compared to their bulk counterparts due to small particle size and uniform distribution. Technically, spinel ferrites are an important group of magnetic materials with diverse properties applicable in the fabrication of electronic, magnetic and microwave devices.

Cobalt ferrite is partially inverse spinel material having semiconducting nature and exhibits high resistivity, along with moderate magnetization and magneto resistance and very high magneto crystalline anisotropy. These properties can be tailored by proper choice and composition of trivalent cations to replace Fe^{3+}in the parent lattice of cobalt ferrite caused by a structural variation in the host lattice. The rare earth ferrites found important applications in modern telecommunication and electronic devices. An improvement in the intrinsic magnetic properties of the ferrite can be obtained by using optimization of synthetic parameters and partial substitutions for Fe sites, metal ions having much larger ionic radii compared with the Fe ion radius, such as rare earth ions, can be used for enhancing the magnetization and coercive field and as inhibition agents of the grain growth mechanism at high temperature [118,119].

The improvement is largely associated with the increase of both magnetocrystalline anisotropy and coercive field and magnetization observed in RE substituted ferrites. The RE ions may contribute to a change of new magnetic

interactions, thus improving the magnetic properties [120].Rare earth ions can improve densification and increase permeability and resistivity of ferrites. Previous studies suggest that the inhomogeneous magnetic spin structure can be effectively suppressed by RE doping [55, 56]. Furthermore, it is known that the rare-earth ions (RE) have unpaired 4f electrons and strong spin–orbit coupling of the angular momentum. Moreover, 4f shell of rare-earth ions are shielded by $5s^2 5p^6$ orbital and almost not affected by the crystal field of surrounding ions. Doping of rare-earth ions into spinel ferrites, 4f–3d coupling takes place which determines the magnetocrystalline anisotropy of the samples.

One of the most remarkable feature of spinel ferrites is the strong dependence of properties on the state of chemical order, i.e., on the cation distribution [121]. Whereas the magnetic order of the ferrimagnetic spinels is due to a super-exchange interaction mechanism occurring between the metal ions in the tetrahedral A-sites and octahedral B-sites, magnetization arises from the difference of the magnetic moments of the ions in the B-sites and those of the A-sites [122].

RE enters into the 'B' sites by displacing a proportionate number of Fe^{3+} from 'B' to 'A' sites. It is reported that rare earth praseodymium (Pr^{3+}) ions can improve the magnetic properties of hexagonal ferrite [123-125]. However, to the best of authors knowledge there are no reports are available in the literature regarding the substitution of Pr^{3+} ions in cobalt spinel ferrite synthesized by sol-gel auto combustion technique. In the current study we have directed our attention to the preparation of rare earth Pr^{3+} substituted $CoFe_2O_4$ ferrite nanodimensional powders by sol-gel auto-combustion method. The effect of Pr^{3+} on the structural and magnetic properties of $CoFe_2O_4$ was in focus of the investigation.

5.2 Experimental

Sol-gel auto-combustion method was used to synthesize Pr^{3+} substituted $CoFe_2O_4$. Analytical grade citric acid ($C_6H_8O_7 \cdot H_2O$), praseodymium nitrate $Pr(NO_3)_3.6H_2O$, cobalt nitrate $Co(NO_3)_2.6H_2O$, and iron nitrate ($Fe(NO_3)_3 \cdot 9H_2O$) were used as starting materials.

\

5.2.1. Sol Formation

The stoichiometric amount of above mentioned metal nitrate and citric acid was dissolved into de-ionized water to form a mixed solution. Homogenous distribution and segregation of the metal ions was achieved by the use of citric acid. The pH value of the solution was maintained in the range 7 by drop wise addition of ammonia solution (base catalyst) in order to speed up the reaction. The solution was constantly stirred using a magnetic agitator. The condensation reaction took place between the adjoining metal chlorides and the molecules of citrates yielding a polymer precursor in colloidal dimensions known as sol.

5.2.2 .Gel Formation

The obtained sol was heated at 90°C on a hot plate under regular stirring to condensate into a xerogel.

5.2.3. Powder Formation

An increase of temperature up to 300 °C led to the ignition of the dry gel and a loose ferrite nanopowder was obtained through the burning of gel in a self-propagating combustion manner. During the combustion process, exothermic decomposition of a redox mixture of metal chlorides and citric acid took place along with the removal of gases such as H_2O, N and CO_2 etc.

Reaction procedure was carried out in air atmosphere without protection of inert gases. The molar ratio of metal nitrates to citric acid was taken as 1:3.The as prepared powder then annealed at 600 ºC for 4 h.

Sol-gel auto-combustion synthesized powder samples were X-ray examined by Phillips X-ray diffractometer (Model 3710) using Cu-K_α radiation (λ=1.5405Å). Transmission electron microscope (TEM) measurements were recorded on Philips (Model CM 200). The infrared spectra of all the samples were recorded at room temperature in the range 300 cm^{-1} to 800 cm^{-1} using Perkin Elmer infrared spectrophotometer. Room temperature magnetization of the samples was measured using the pulse field magnetization set-up, with the maximum applied magnetic fields of 9000 Oe.

5.3 Results and Discussion

5.3.1. Structural Analysis

It is obvious from the XRD patterns (Fig. 5.1) of $Pr_xCoFe_{2-x}O_4$ that the patterns were indexed and cubic lattice was observed. The results indicate that the material has a well-defined crystalline single phase belonging to the fcc system. The diffraction pattern gave a verification of the presence of spinel crystal structure for each composition of $Pr_xCoFe_{2-x}O_4$. Since the XRD patterns of $PrFeO_3$ phase cannot be found in Fig. 5.1 for $x < 0.075$, we can draw a conclusion that Pr^{3+} has entered the lattice of ferrite successfully. It is observed that the cubic spinel phase coexists with some amount of $PrFeO_3$ phase in $x \geq 0.075$. As $CoFe_2O_4$ is nearly inverse spinel, this anomaly in the intensity distribution may arise from the following facts: (i) differences in the cation distribution among the [A] and [B] sites in the spinel lattice and; (ii) phase inhomogeneity, in particular presence of ferrite phases with different cation distributions. The ionic radius of Pr^{3+} ions is 1.13Å which is larger than that of Fe^{3+} (0.67 Å), and the amount of Fe^{3+}ions substituted by Pr^{3+}ions is limited, thus redundant Pr^{3+}ions aggregates on the grain boundaries forming $PrFeO_3$ phase. As a result, there was a limit for the replacement of Fe^{3+} with Pr^{3+}, and the maximum was $x = 0.05$ in our experiment.

The X-ray diffraction patterns show as light shifting in peaks position due to unstable d-spacing values with increasing Pr^{3+} content in all ferrite samples. The replacement of Fe^{3+} ions in octahedral B sites by Pr^{3+} ions would cause the expansion of unit cell, resulting in larger lattice constants [11].

The lattice parameter 'a' was calculated using the following equation [126]:

$$a = d\sqrt{(h^2 + k^2 + l^2)} \qquad \textbf{5.1}$$

where d is the inter-planer spacing and (hkl) is the index of the XRD reflection peak. It is observed from Table 5.1 and Fig. 5.2 that lattice constant 'a' increases from 8.373- 8.423 Å with increase in Pr^{3+} substitution. The ionic radius of Pr^{3+} and Fe^{3+} ions is 1.13 and 0.67 respectively, therefore, when $Fe^{3+}$was replaced by Pr^{3+} the lattice constant should aggrandize as the content of the Pr^{3+}increased.The relationship between Pr^{3+} substitution and lattice parameter can be explained by Vegard's law [127].The law states that the crystallographic parameters of a continuous substitutional solid solution vary linearly with concentration at constant

temperature when the nature of the bonding is similar in the constituent phases.

The X-ray density (dx) of all the samples of the series was obtained by the following relation;

$$dx = \frac{8M}{Na^3} \qquad \textbf{5.2}$$

Where 8 is the number of molecules per unit cell, 'M' is the molecular weight of sample, 'N' is the Avogadro's number and 'a' is lattice constant. It is observed from Table 5.1 and Fig. 5.3 the X-ray density exhibits an increasing trend from 5.309 to 5.405g/cm^3 with an increase in Pr^{3+} substitution. The atomic weight of Pr^{3+} is 140.90amu which is larger than the atomic weight of Fe^{3+} (55.84amu), this lead to increase in dx with Pr^{3+} substitution.

The average crystallite diameter 'D_{XRD}' of powder estimated from the most intense (311) peak of XRD and using the Scherrer formula [126]:

$$D_{XRD} = \frac{0.9\lambda}{B\cos\theta} \qquad \textbf{5.3}$$

Where λ is the wavelength used in XRD, B is the full width of half maximum in (2θ), θ is the corresponding Bragg angle. The reflection plan (311) was used to calculate the crystallite size and lattice constant since this crystallographic plane exhibited the maximum diffraction intensity. Figure 5.4 and Table 5.1 shows that the crystallite size varies in the range of 24.5 to 37.9 nm with Pr^{3+} substitution.

The specific surface area (S) was calculated from the diameter of the particle in nanometer and the measured density in g/cm^3 using the relation [100]:

$$S = \frac{6000}{Dd_B} \qquad \textbf{5.4}$$

where D is the average crystallite size and d_B is the bulk density. The variation of surface area (S) with Pr^{3+} content x is shown in Fig. 5.4 and Table 5.1.

SEM micrographs were analyzed to investigate the grain structure of the nanoparticles and assist in understanding the development of the grain sizes. Fig.5.5 shows the SEM images of the synthesized pure cobalt ferrite and Pr^{3+} substituted cobalt ferrite. It is observed that the average grain size decreases with increase in Pr^{3+} substitution. When Fe^{3+} ions in ferrite lattices are substituted by Pr^{3+}ions, the lattice parameter is found to change. The variation of lattice parameter will lead to the lattice strains, which produce the internal stress. Such a stress

hinders the growth of grains, so the grain sizes of the samples substituted with Pr^{3+} ions. It is also to be noted that the larger bond energy of Pr^{3+}-O^{2-}, all the Pr^{3+}substituted samples have higher thermal stability relative to pure $CoFe_2O_4$, and hence more energy is needed for the substituted samples to complete crystallization and grain growth. As it is observed from XRD data as well, Pr^{3+} ions, because of their larger ionic radius, enter partially into the lattice; the rest may reside at the grain boundary as a second phase. The presence of Pr^{3+} ions at the boundary of grain will bring pressure on the grain and hinder the growth of grains.

TEM images (Fig. 5.6 a and b) of the typical samples show that the particles are aggregated and the average values of the nanocrystalline samples are consistent with the result from XRD according to the Scherrer formula. Interestingly, Fig. 5.6 (a and b) demonstrates that the nanoparticles are not in spherical shape but in square slice shape with small thickness. Fig. 5.6 (c) shows a selected area electronic diffraction (SAED) pattern of the nanoparticles.

The bulk density 'd_B' of the specimens has been determined by the hydro-static method. The variation of the bulk density is shown in Fig. 5.7 and the values are depicted in Table 5.1. Moreover the presence of Pr^{3+} ions activates the sintering process in ferrites and leading increasing densities

Since the formation of secondary phase ($PrFeO_3$) fills inter-granular voids and exhibits good densification, a decrease in porosity was expected with Pr^{3+} contents. The percentage porosity is calculated using the following relation

$$P = \left(\frac{d_X - d_B}{d_X} \right) \times 100 \qquad \textbf{5.5}$$

where dx and d_B are the X-ray density and bulk density respectively. Table 5.1 and Fig. 5.7 shows that the porosity increased with increase in Pr^{3+} substitution. The increase in porosity is related to decrease in crystallite diameter and bulk density.

Using the experimental values of lattice constant 'a', oxygen positional parameter 'u' and substituting using the following equations, the allied parameters such as tetrahedral and octahedral bond length (d_{Ax} and d_{Bx}), tetrahedral edge, shared and unshared octahedral edge (d_{AXE}, d_{BXE} and d_{BXEU}) were calculated.

$$d_{AX} = a\sqrt{3}\left(u - \frac{1}{4} \right) \qquad \textbf{5.6}$$

$$d_{BX} = a\left[3u^2 - \left(\frac{11}{4}\right)u + \frac{43}{64}\right]^{\frac{1}{2}} \quad \textbf{5.7}$$

$$d_{AE} = a\sqrt{2}\left(2u - \frac{1}{2}\right) \quad \textbf{5.8}$$

$$d_{BEshaired} = a\sqrt{2}(1-2u) \quad \textbf{5.9}$$

$$d_{BEunshaired} = a\left(4u^2 - 3u + \frac{11}{16}\right)^{\frac{1}{2}} \quad \textbf{5.10}$$

Table 5.2 and Fig. 5.8 show that all the allied parameter increased with the increase in Pr^{3+} substitution. The variation of allied parameters is related to the difference in the ionic radii of Pr^{3+} and Fe^{3+}. The Pr^{3+} ion with the larger ionic radii increases the allied parameter as the replaces Fe^{3+} ions of smaller ionic radii.

The hopping length for A-site (L_A) and B-sites (L_B) are calculated using the values of lattice constant.

$$L_A = a\sqrt{\frac{3}{4}} \quad \textbf{5.11}$$

$$L_B = a\sqrt{\frac{2}{4}} \quad \textbf{5.12}$$

Table 5.3 and Fig. 5.9 shows the variation of hopping lengths L_A and L_B with Pr^{3+}substitution. It is observed from Table 5.3 and Fig. 5.9 that the distance between the magnetic ions (hopping length) increases as Pr^{3+} substitution increases. This behavior of hopping lengths with Pr^{3+} substitution is an analogous with the behavior of lattice constant with Pr^{3+} substitution. This variation may be attributed to the difference in the ionic radii of the constituent ions, which makes the magnetic ions become larger to each other and the hopping length increased.

5.3.2 Infrared Spectroscopy

In order to confirm the constitutions of spinel structure and to investigate the chemical properties of ferrite, the infrared (IR) spectroscopy of Pr^{3+} substituted $CoFe_2O_4$. The analysis of IR spectra can give information about structural transformation and can be considered as an important tool to get information about position of ions in the crystal. The room temperature IR spectra of all the composition are shown in Fig. 5.10. IR spectrum of the synthesized samples

displayed two absorption bands characteristic of the spinel ferrites at 707-757 and 454-477 cm^{-1}. The higher frequency band (ν_1) was due to stretching vibration of tetrahedral metal oxygen bond and the lower frequency band (ν_2) was due to octahedral metal oxygen bond [84].The band positions for all the investigated composition are given in Table 5.4. The change in the lattice constant is responsible for this shift of the center frequencies. The increase in the unit cell dimensions due to the replacement of Fe^{3+} ions by larger ionic radius Pr^{3+} ions affects the Fe^{3+}–O^{2-}stretching vibrations and this is a prominent cause of change in band positions. The change in the frequency of ν_1 stretching band indicates the preference of Pr^{3+} ions to occupy the octahedral sites. The peak intensity of frequency bands slightly changes with an increasing Pr^{3+}substitution. It is known that the intensity ratio is a function of the change of dipole moment with the inter-nuclear distance (dμ/dr) [128]. This value represents the contribution of the ionic bond Fe-O in the lattice. Furthermore, it is observed from Fig. 5.10 that the normal mode of vibration of tetrahedral cluster (ν_1) is higher than that of octahedral cluster (ν_2), which is attributed to the shorter bond length of tetrahedral cluster and longer bond length of octahedral cluster.

5.3.3 Cation Distribution

The cation distribution in spinel ferrite can be obtained from the analysis of X-ray diffraction pattern. In the present work, the Bertaut method [101] is used to determine the cation distribution. The cation distribution of $Pr_xCoFe_{2-x}O_4$ is listed in Table 5.5. The radius of Pr^{3+} ions was larger than that of others metal ions in the as-obtained products and the interspaces of tetrahedral sites (A) was smaller than that of octahedral site [B], so Pr^{3+} ions was prior to occupy the octahedral sites [B].Partial migration of Co^{2+} ions (0.78Å) from B to A sites has been observed by increasing the Pr^{3+} concentration. Fe^{3+} ions showed no strong preference for any site and occupy both tetrahedral A- and octahedral B-site.

The mean ionic radius of the tetrahedral A- and octahedral B-sites (r_A and r_B) can be calculated for all the samples using the relations discussed elsewhere [129]. The values of r_A and r_B are listed in Table 5.6 and its variation is shown in Fig. 5.11. It is observed from Table 5.6 and Fig. 5.11that the mean ionic radius of the tetrahedral A- and octahedral B-sites increased with an increase in Pr^{3+}

substitution. The increase in r_B is due to the replacement of smaller Fe^{3+} ions of ionic radii (0.67 Á) by the larger rare earth Pr^{3+} ions with 1.13 Å ionic radii at octahedral B-site. The small increase in r_A is due to the migration of Co^{2+} ions from B site to A site, that resulted in the increase the octahedral radii 'r_B'.

The theoretical values of lattice parameter can be calculated with the help of following equation [105],

$$a_{th} = \frac{8}{3}\sqrt{3}\left[\left(r_A + R_0\right) + \sqrt{3}\left(r_B + R_0\right)\right] \qquad \textbf{5.13}$$

Where r_A and r_B are radii of tetrahedral (A) site and octahedral [B] site, R_O is radius of oxygen i.e. (R_O = 1.32 Å). The values of theoretical lattice parameter `a_{th}' obtained by using relation (5.13) are shown in Table 5.6 and its variation is shown in Fig. 5.12. It is observed that a_{th} increased from 8.518 to 8.582Á with increase in Pr^{3+} substitution. The difference between a and a_{th} may be related to the lattice defects for polycrystalline material and the presence of Fe^{3+} on A or B sites which are not taken into account [130].

Using the values of 'a', the radius of oxygen ion R_O = 1.32 Á and 'r_A' in the following expression, the oxygen positional parameter 'u' can be calculated [20],

$$u = \left[\left(r_A + R_0\right)\frac{1}{\sqrt{3}a} + \frac{1}{4}\right] \qquad \textbf{5.14}$$

Figure 5.12 and Table 5.6 shows the variation of oxygen positional parameter 'u' with Pr^{3+} substitution. Our value of 'u' is larger than its ideal value (u = 0.375 Å), this larger value may probably be due to many reasons, including the history of the samples, experimental or measurement errors, e.g. precision of the observed X-ray intensity and the theoretical data used for the scattering model of the system.

5.3.4 Magnetization

The magnetic hysteresis loops collected at room temperature for the present samples are shown in Fig. 5.13. As shown in the hysteresis loop of all the samples are characterized by its moderate magnetization which monotonically increases with increase in applied field and it does attain saturation at the maximum attainable field. The values of saturation magnetization (Ms), remanent magnetization (Mr) and coercivity (Hc) of Pr^{3+}substituted samples are shown in

table 5.7. It is observed from Table 5.7, Figs 5.13 and 5.15 that magnetization increased from 54.7 to 64.2 with increase in Pr^{3+} substitution for $x \leq 0.075$, followed by decrease in Ms for x = 0.1.There are three factors for interpreting magnetization behavior such as hyperfine field enhancements with increase in Fe^{3+}–O–Fe^{3+} superexchange interaction strength and super-transfer fields, spin canting (non-collinear magnetic order), and magnetic dilution with valence state change of Fe^{3+}($3d^5$ high spin) ions into Fe^{2+}($3d^6$ low spin) ions after being substituted by Pr^{3+} ions. At the same time, the magnetic behavior of the ferrimagnetic hexaferrite material is largely governed by the distribution of iron ions on the crystallographic lattice sites and hence the Fe^{3+}–O–Fe^{3+}exchange interactions (the spin coupling of the 3d electrons). The magnetization of the ferrite material varies with the factors influencing the strength of these exchange interactions. In the Pr^{3+} substituted ferrite, Pr^{3+}-Fe^{3+}interactions may also exist via 4f–3d couplings which can cause changes in magnetic properties. The substitution of Pr^{3+} for Fe^{3+}in the spin- up states (12k,6g,$4f_3$ and 2d) appears to cause reduction in magnetization while the substitution in the spin-down states (4e, $4f_1$ and $4f_2$) may lead to an increase in the net magnetization [131].Therefore, if Fe^{3+}in the spin-down states were replaced by Pr^{3+}, the net magnetization in upward spin is expected to increase the total magnetic moment and hence strengthen the magnetization, just as the results show. Besides, the substitution of $Pr^{3+}$to Fe^{3+} induces a perturbation in both electron-density and symmetry around the 2d lattice site, which could strengthen the exchange interactions and hence strengthen the magnetization [108]. According to the above discussion, through the Pr^{3+}substitution in the spin-down states, the Fe^{3+}–O–Fe^{3+}superexchange interaction was strengthened. Hyperfine fields at 12k and 2d sites were enhanced by the higher net magnetization which was meaningful to Ms [123]. Interestingly the Ms decreased for highest value of Pr^{3+} in $CoFe_2O_4$. The observed reduction in saturation magnetization upon RE^{3+} is more complex and semi empirically depends on the exchange energy associated to the magnetic moment of transition metal (TM), the TM–O distances, TM–O–TM angle [118], 4f spin contribution to the spin-up magnetic moment of the ferrimagnetic structure and associated valance changes in Fe^{3+} to Fe^{2+} at 2a and/or $4f_2$ sites upon RE^{3+} substitution These interactions are largely dependent on the associated structural changes as well. The

overall decrease in magnetization with RE^{3+} substitution is also associated with the non-collinear arrangement of magnetic moment of Fe^{3+}. Spin canting or non-collinear magnetic order is a behavior in which spin orientations of magnetic ions align by making angles from the preferred direction. The net magnetic moment or magnetization will change with the spin canting. The spin canting effect may also cause a decrease in Ms. The net magnetic moment or magnetization will change with the spin canting. The spin canting effect caused a decrease in Ms. The magnetic moments in the case of the rare-earth ions generally originates from the localized 4f electrons. Therefore, the effect of Pr^{3+} ions in the $CoFe_2O_4$ materials seems to be similar to the substitution of non-magnetic ions in the octahedral Fe sites of the spinel lattices. As the net magnetic moments in the ferrimagnetic ferrite materials depend on the number of magnetic ions occupying the tetrahedral and octahedral sites, the enhancement in the magnetization as a function of Pr^{3+} substitution is clear. The magnetic moment per formula unit (n_B) was calculated from Neel's sub-two-lattice model using the relation,

$$n_{Bcal.} = M_B - M_A \qquad \textbf{5.15}$$

where M_B and M_A are the B and A sub-lattice magnetic moments in μ_B. AB_2O_4 spinel crystal structure consist of inter-sublattice (A-B) super-exchange interactions and intra-sub-lattice(A-A) and (B-B) exchange interactions. Inter-sub-latticesuper-exchange interactions of the cations on the (A-B) are much stronger than the (A-A) and (B-B) intra-sub-lattice exchange interactions [132]. It is observed from table 5.5 that Pr^{3+}ions occupy the octahedral sites in the ferrite which causes Co^{2+} ions to migrate from B site to A site. This occupancy of Pr^{3+} and Co^{2+} ions increases the difference of magnetic moment between A and B sublattice which resulted in the increase in calculated magnetic moment.

The observed magnetic moment ($n_{BObs.}$) per formula unit in the Bohr magneton (μ_B) was calculated using a relation 5. 16

$$n_{BObs.} = \frac{\text{Molecular weight (Mw)} \times \text{saturation magnetization (Ms)}}{5585} \qquad \textbf{5.16}$$

It is obvious from Table 5.7 and Fig. 5.14 that the calculated and observed values of the magneton number are in good agreement with each other.

Figure 5.15 shows the variation of coercivity with Pr^{3+} substitution. The dependence of the coercivity can be co-related with the variation of grain size, and

it is known fact that coercivity is inversely proportional to the grain size. Larger grain tends to contain a more number of domain walls. The magnetization or demagnetization caused by domain wall movement requires less energy than that required by domain rotation. On contrast with the contribution to magnetization or demagnetization due to domain rotation, the wall movement increases as the number of walls increases with increasing grain sizes [67]. Therefore, samples having larger grains are expected to have lower coercivity, and vice versa. This seems to be the main reason for the changes in coercivity of the Pr^{3+} substituted $CoFe_2O_4$.At the same time, impurities distributed in the grain boundary area break and go against the displacement of domain walls. Due to the existence of the foreign phase $PrFeO_3$ and the like, the samples after doping with more Pr^{3+}ions were expected to have larger coercivity [19]. As reported in the earlier references, the magnetocrystalline anisotropy with anisotropic Fe^{3+} ions will enhance after the substituting of the rare earth, which causes increase in coercivity [133,134].

Table 5.1 Lattice constant (a), X-ray density (d_x), crystallite size (D_{XRD}), specific surface area (S), bulk density (d_B) and porosity (P) of $Pr_xCoFe_{2-x}O_4$

Comp. x	a (Å)	dx (g/cm^3)	D_{XRD} (nm)	S (m^2/g)	d_B (g/cm^3)	P (%)
0.000	8.3732	5.309	24.515	56.50	4.332	18.41
0.025	8.3761	5.352	37.883	36.06	4.392	17.93
0.050	8.3835	5.386	26.046	51.91	4.438	17.60
0.075	8.3984	5.405	37.905	35.04	4.517	16.42
0.100	8.4234	5.404	37.893	35.00	4.524	16.28

Table 5.2 Tetrahedral bond (d_{AX}), octahedral bond (d_{BX}), tetra edge (d_{AXE}) and octahedral edge (d_{BXE}) (shared and unshared) of $Pr_xCoFe_{2-x}O_4$

Comp. x	d_{AX} (Å)	d_{BX} (Å)	Tetra edge (Å)	Octa edge d_{BXE} (Å)	
			d_{AXE}	Shared	unshared
0.000	1.8999	2.0443	3.1025	2.8183	2.9621
0.025	1.9006	2.0450	3.1036	2.8193	2.9631
0.050	1.9023	2.0468	3.1063	2.8218	2.9657
0.075	1.9056	2.0504	3.1118	2.8268	2.9710
0.100	1.9113	2.0565	3.1211	2.8352	2.9798

Table 5.3 Hopping lengths (L_A and L_B) of $Pr_xCoFe_{2-x}O_4$

Comp. x	Hopping length	
	L_A (Å)	L_B (Å)
0.000	3.6257	2.9604
0.025	3.6270	2.9614
0.050	3.6302	2.9640
0.075	3.6366	2.9693
0.100	3.6474	2.9781

Table 5.4 IR absorption bands of $Pr_xCoFe_{2-x}O_4$

Comp. x	υ_1 (cm^{-1})	υ_2 (cm^{-1})
0.000	757	454
0.025	754	461
0.050	718	471
0.075	713	477
0.100	707	475

Table 5.5 Cation distribution of $Pr_xCoFe_{2-x}O_4$

Comp. x	Cation distribution
0.000	$(Fe)^A\,[CoFe]^B\,O_4$
0.025	$(Fe)^A\,[CoPr_{0.025}Fe_{0.975}]^B\,O_4$
0.050	$(Co_{0.05}Fe_{0.95})^A\,[Co_{0.95}Pr_{0.05}Fe]^B\,O_4$
0.075	$(Co_{0.05}Fe_{0.95})^A\,[Co_{0.95}Pr_{0.075}Fe_{0.975}]^B\,O_4$
0.100	$(Co_{0.1}Fe_{0.9})^A\,[Co_{0.9}Pr_{0.1}Fe]^B\,O_4$

Table 5.6 Ionic radii of tetrahedral A-site (r_A), octahedral B-site (r_B), theoretically lattice constant (a_{th}) and oxygen positional parameter (u) of $Pr_xCoFe_{2-x}O_4$

Comp. 'x'	r_A (Å)	r_B (Å)	a_{th} (Å)	u (Å)
0.000	0.670	0.725	8.518	0.3849
0.025	0.670	0.731	8.533	0.3846
0.050	0.676	0.734	8.550	0.3848
0.075	0.676	0.740	8.565	0.3845
0.100	0.681	0.743	8.582	0.3846

Table 5.7 Saturation magnetization (M_s), remanent magnetization (Mr), magneton number (η_B) and coercivity (H_C) of $Pr_xCoFe_{2-x}O_4$

Comp. x	M_s (emu/g)	M_r (emu/g)	η_B (μ_B)		H_C (Oe)
			Obs.	Cal.	
0.000	54.7	17.2	2.30	3.00	644
0.025	56.1	19.4	2.38	2.96	748
0.050	59.3	20.7	2.54	3.13	691
0.075	64.2	22.1	2.77	3.09	804
0.100	61.4	20.6	2.67	3.26	1013

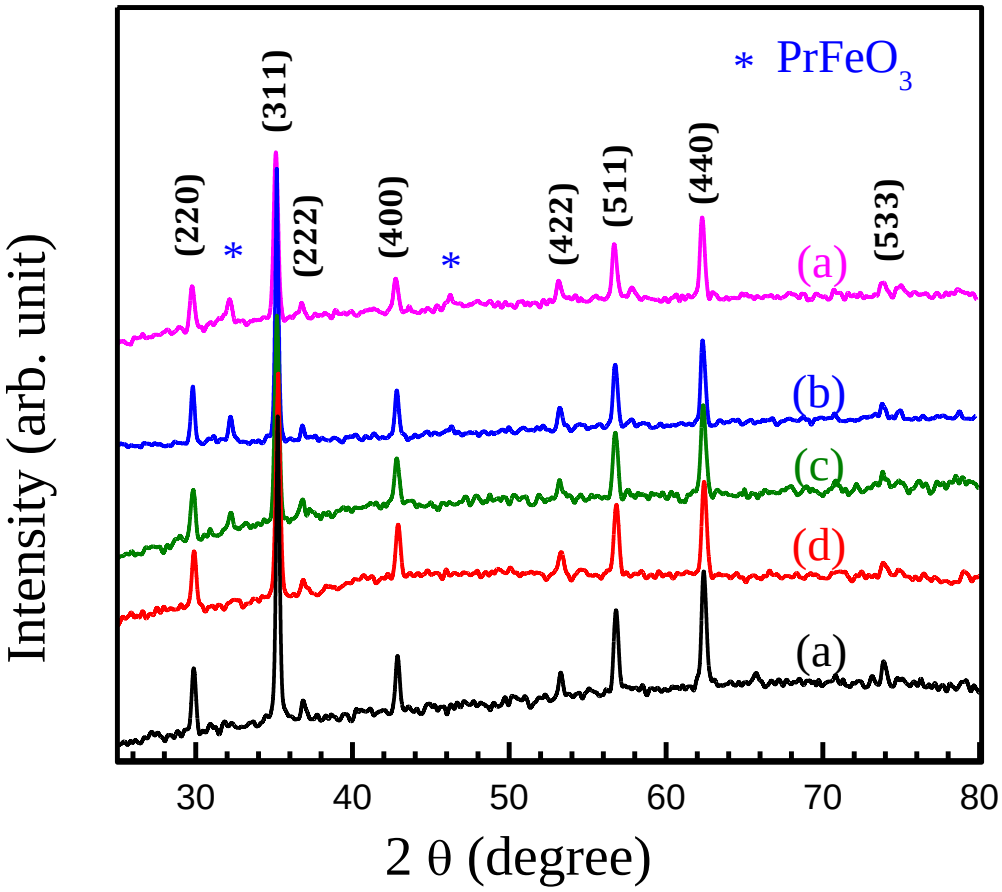

Fig. 5.1: X-Ray diffraction patterns of (a) x = 0.0, (b) x = 0.025, (c) x = 0.050, (d) x = 0.075 and (e) x = 0.1 for $Pr_xCoFe_{2-x}O_4$

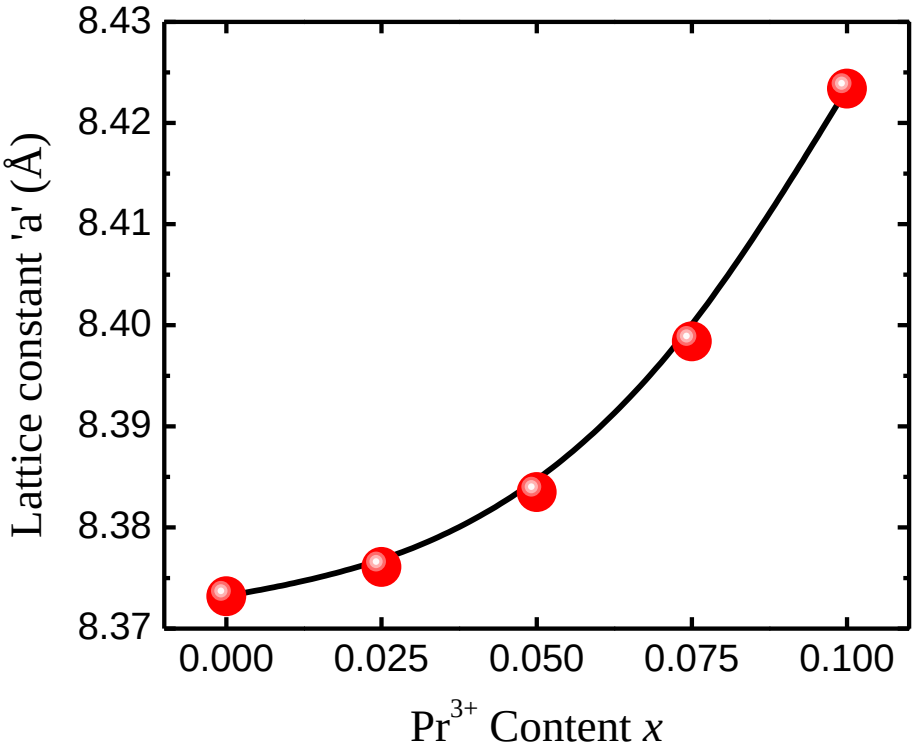

Fig. 5.2: Variation of lattice constant with Pr^{3+}content x

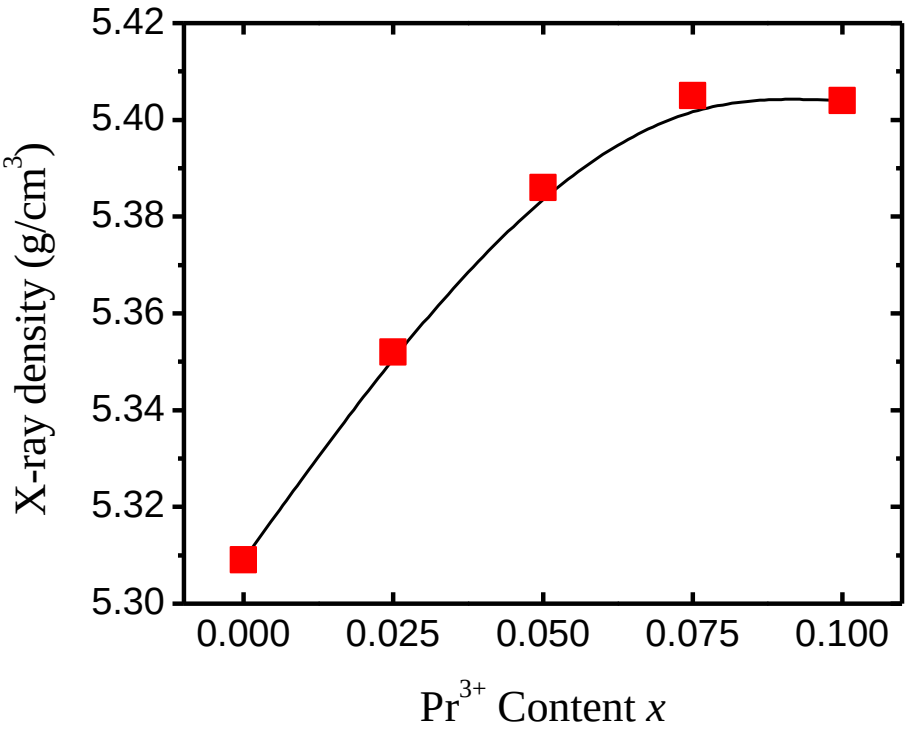

Fig. 5.3: Variation of X-ray density with Pr^{3+} content x.

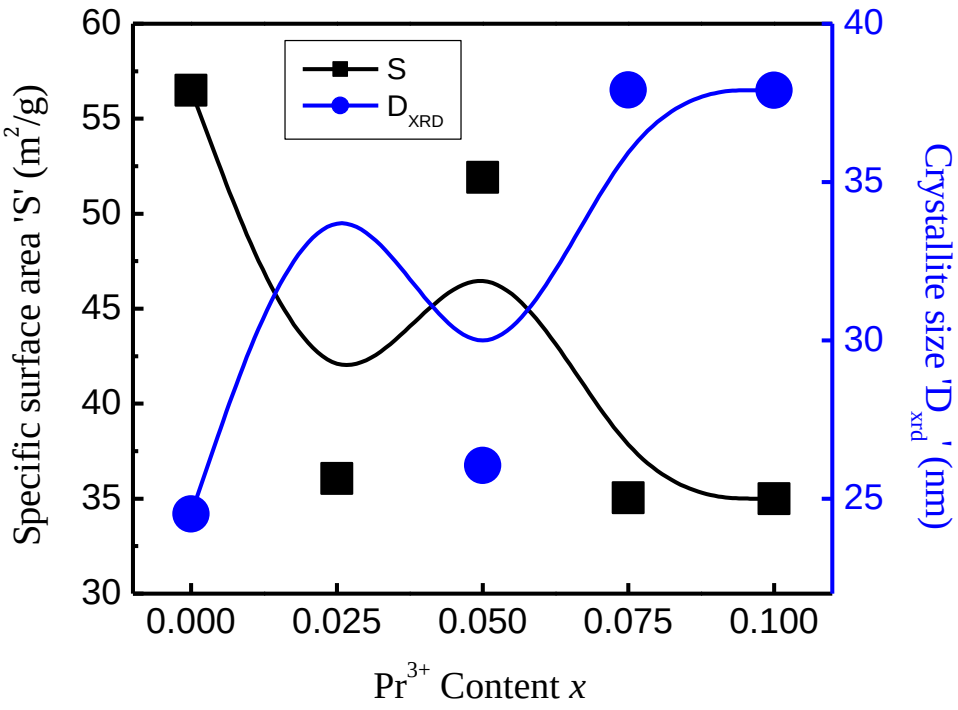

Fig. 5.4: Variation of specific surface area (S) and crystallite size (D_{xrd}) with Pr substitution of $Pr_xCoFe_{2-x}O_4$

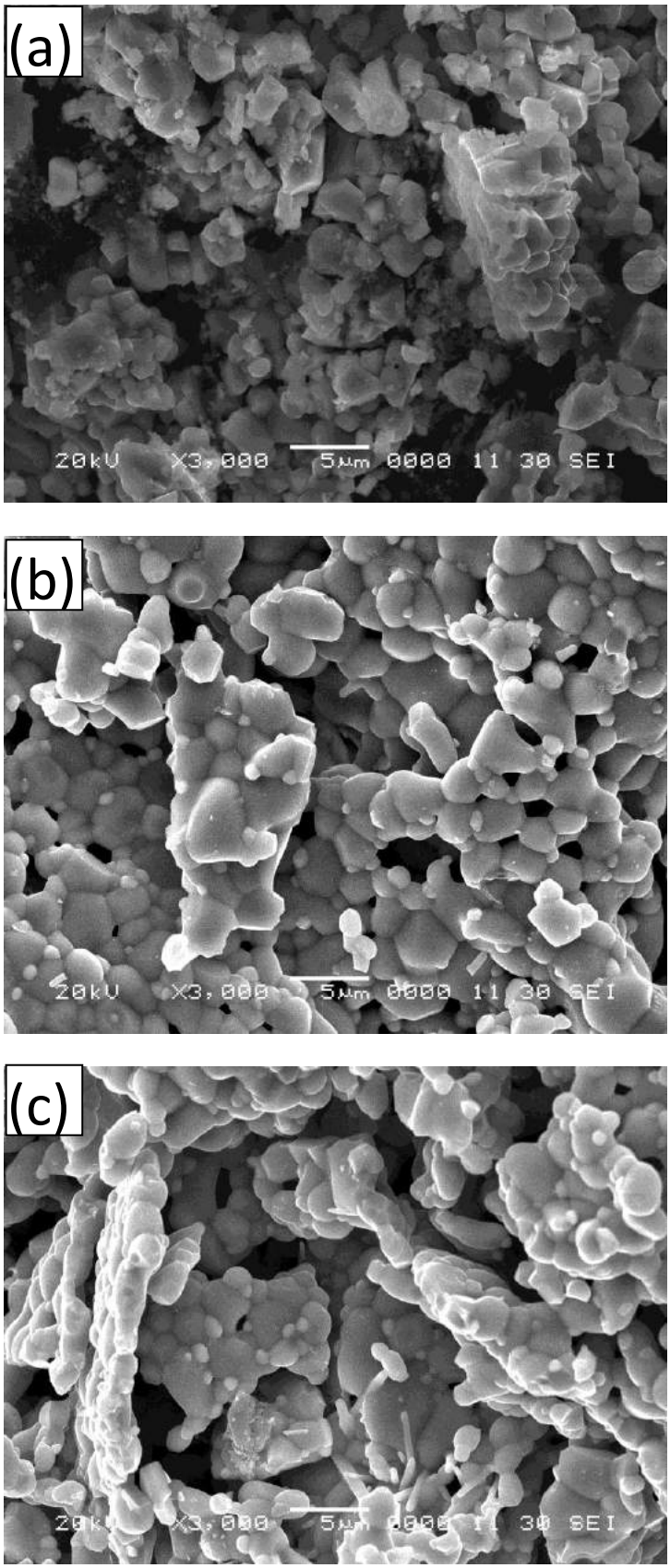

Fig. 5.5. SEM images of (a) x = 0.0, (b) x = 0.025 and (c) x = 0.05,

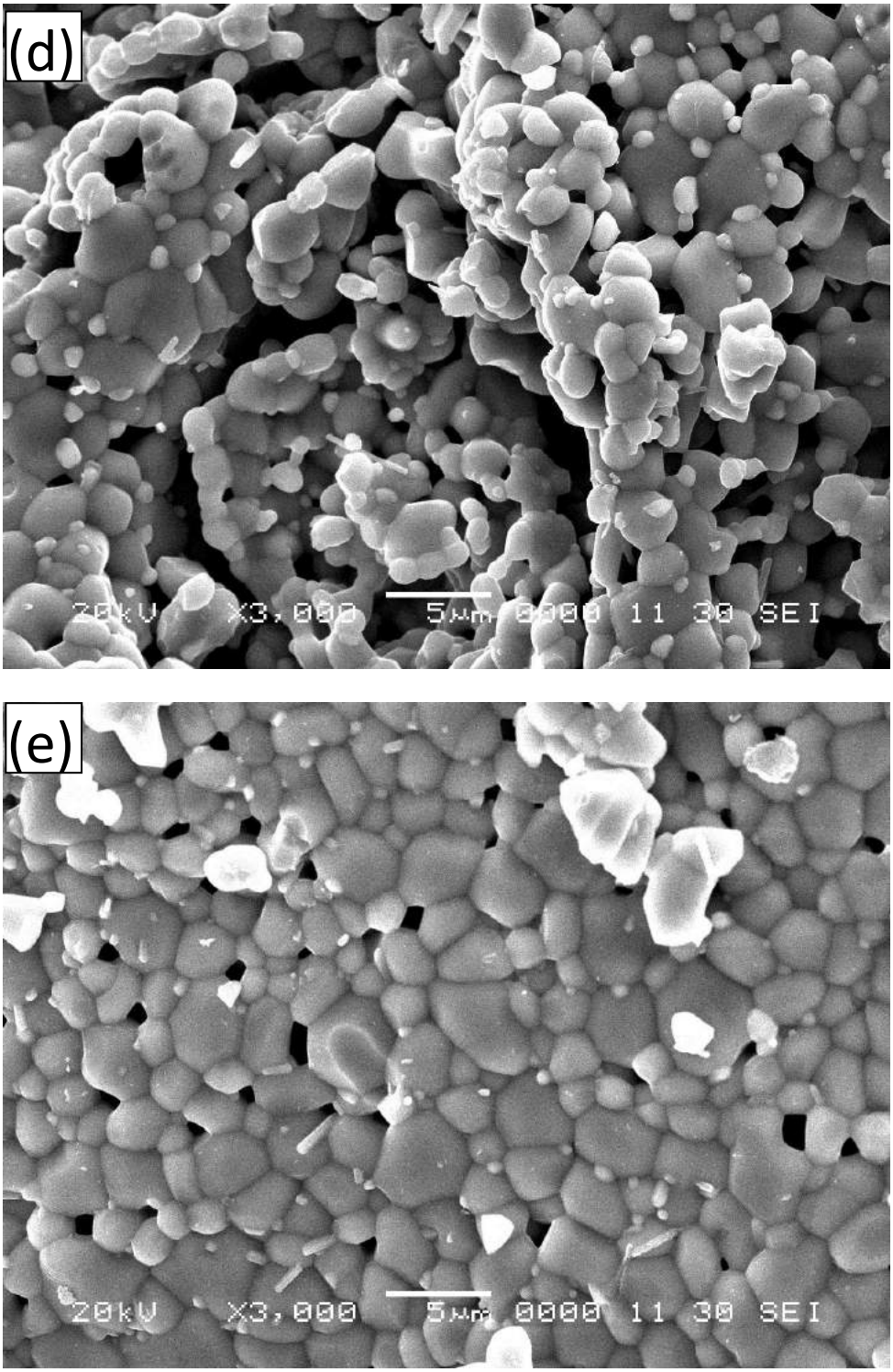

Fig. 5.5. SEM images of (d) x = 0.075 and (c) x = 0.1

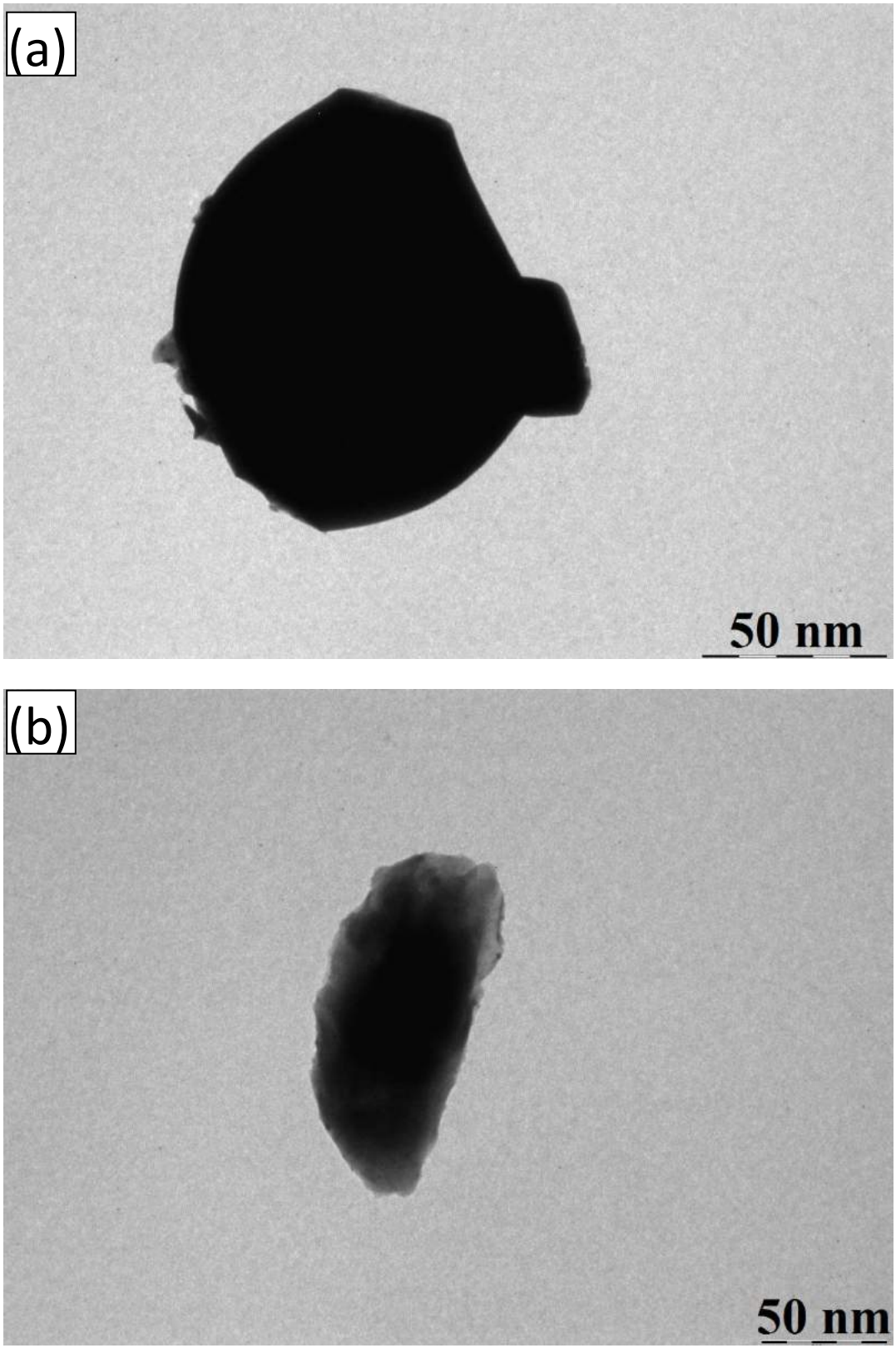

Fig. 5.6: TEM images of (a) x = 0.0 and (b) x = 0.1

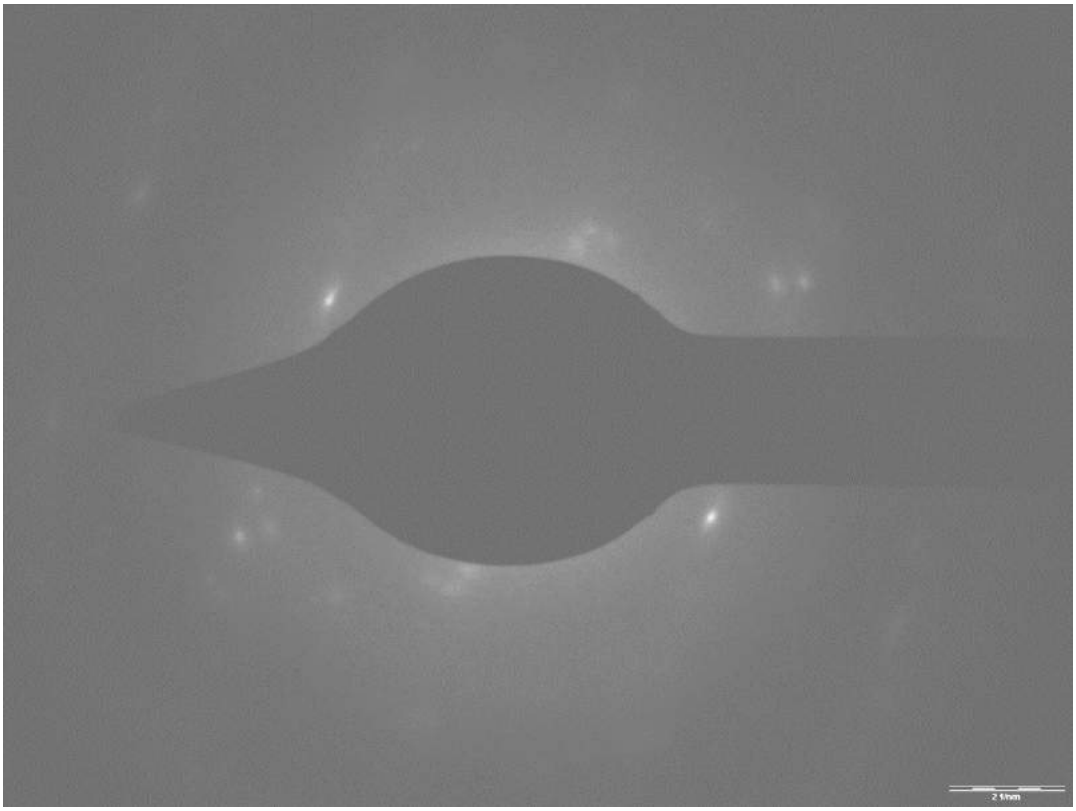

Fig. 5.6:(c) SAED pattern of x = 0.1

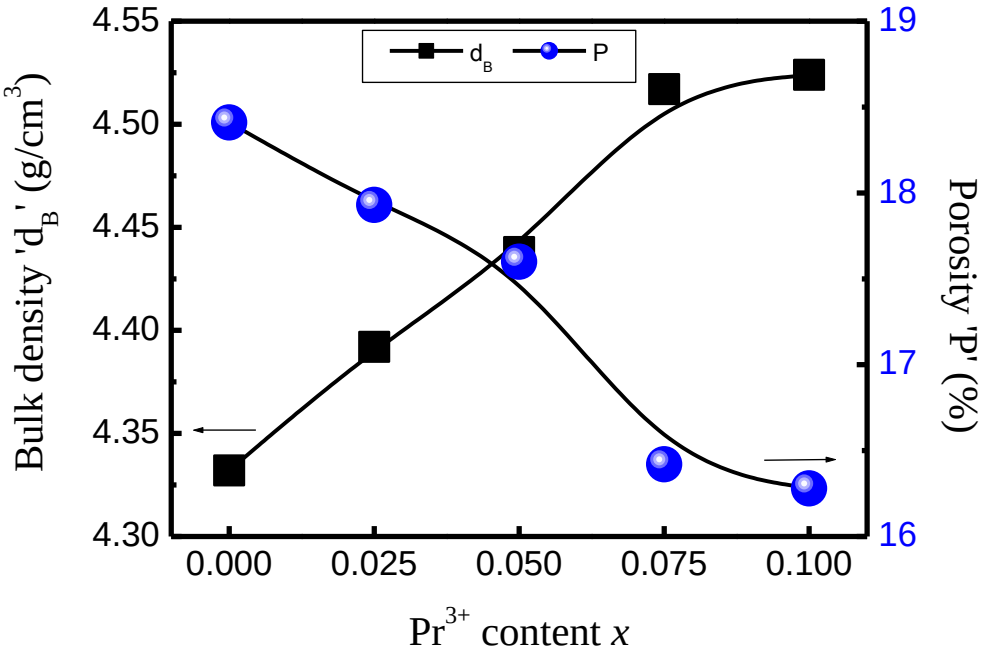

Fig. 5.7: Variation of bulk density (d_B) and porosity (P) with Pr^{3+}content x.

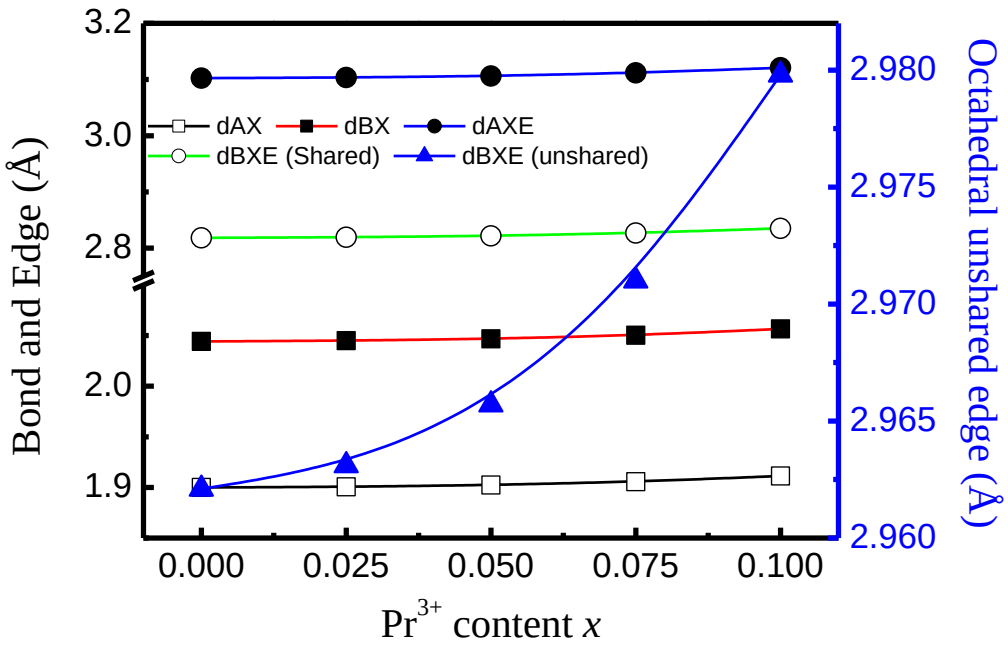

Fig. 5.8: Variation of Tetrahedral bond (d_{AX}), octahedral bond (d_{BX}), tetra edge (d_{AXE}) and octahedral edge (d_{BXE}) (shared and unshared) with Pr^{3+} content x of $Pr_xCoFe_{2-x}O_4$

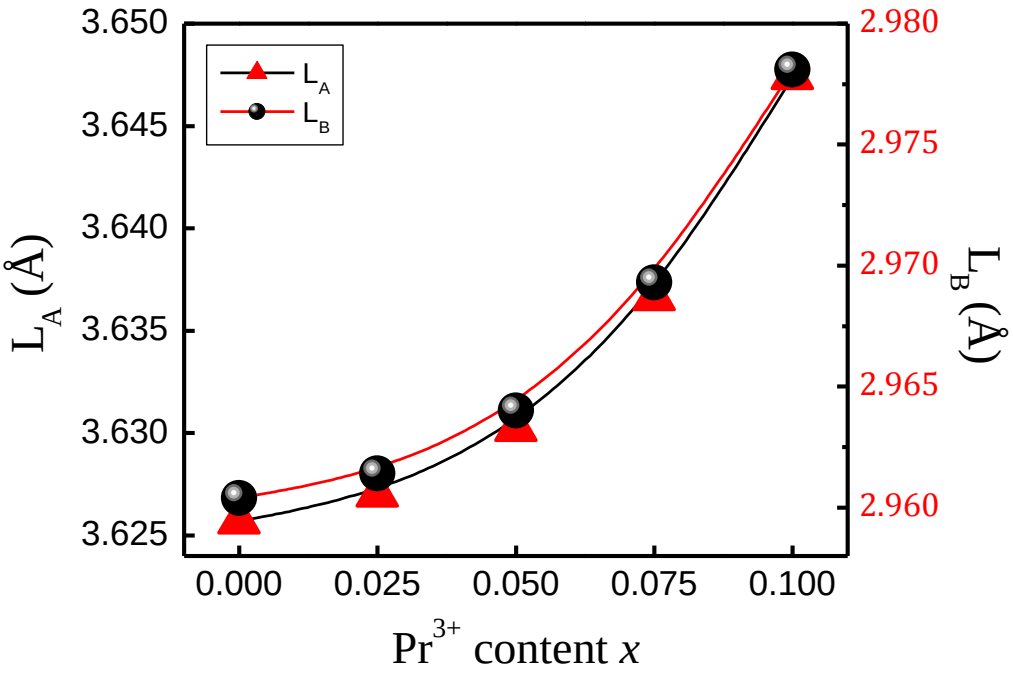

Fig. 5.9: Variation of ionjump lengths (L_A and L_B) with Pr^{3+} substitution of $Pr_xCoFe_{2-x}O_4$

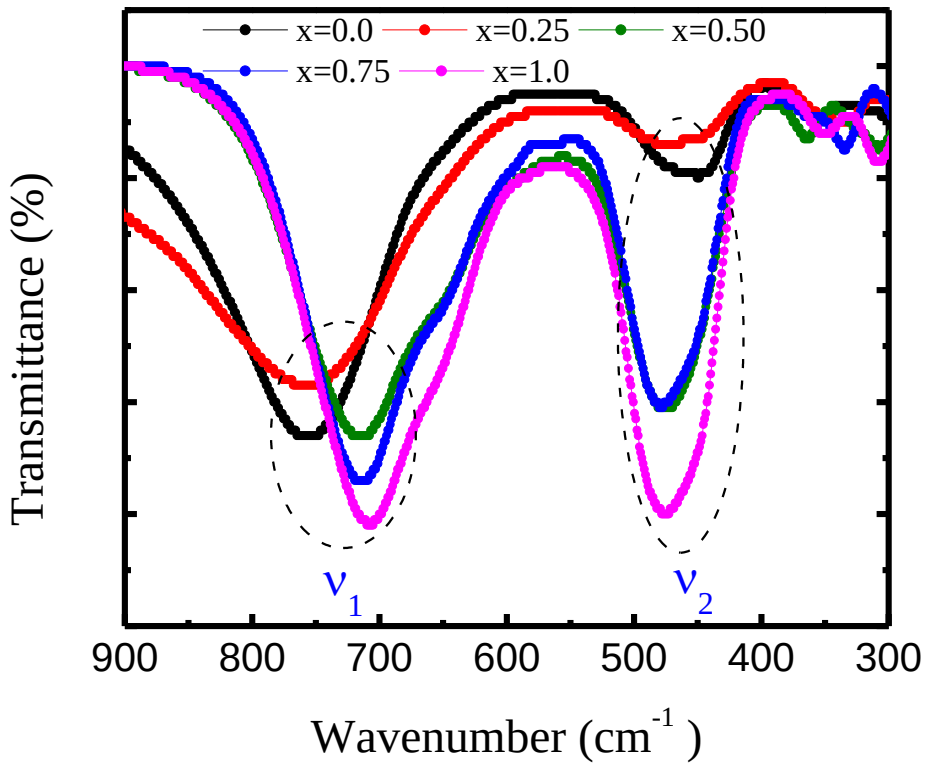

Fig.5.10: Infrared spectra of $Pr_xCoFe_{2-x}O_4$.

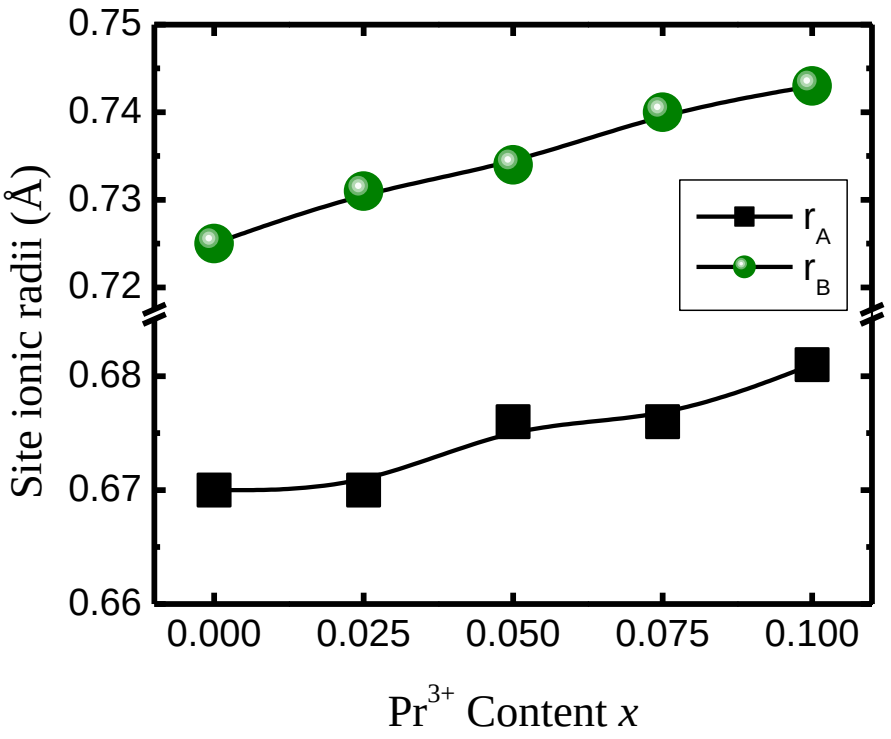

Fig. 5.11: Variation of site ionic radii (r_A and r_B) with Pr^{3+}content x.

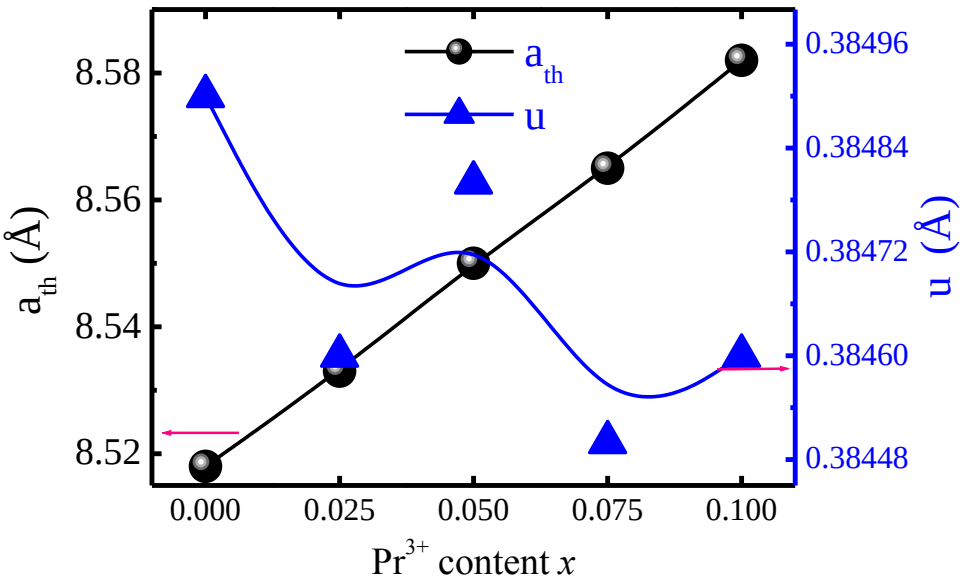

Fig. 5.12: Variation of theoretical lattice constant (a_{th}) and oxygen parameter (u) with Pr^{3+} content x.

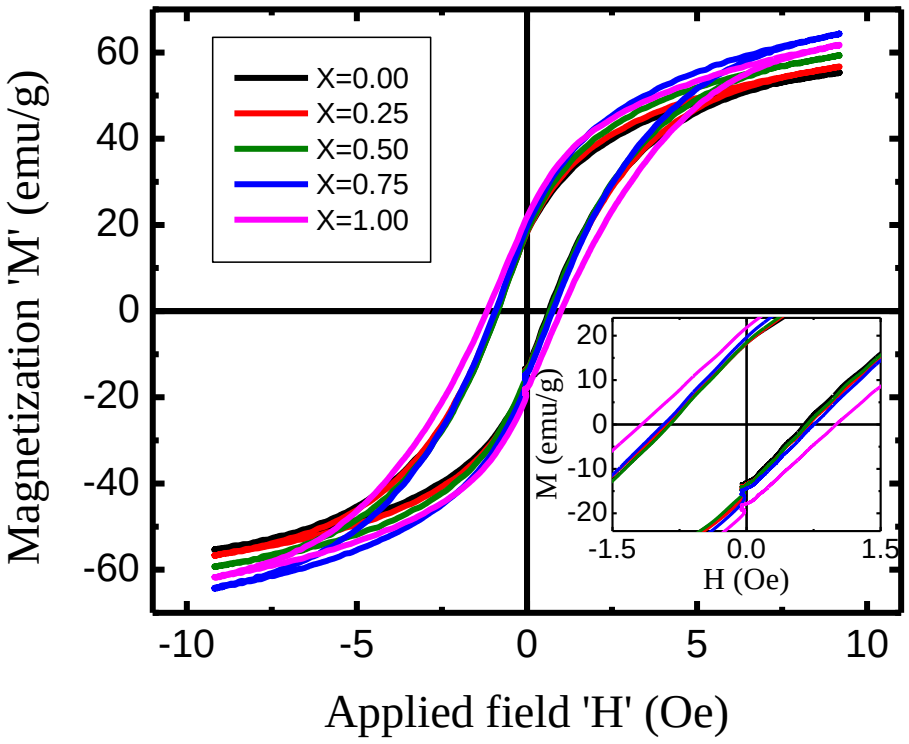

Fig. 5.13: Variation of magnetization (M) with applied field (H) of $Pr_xCoFe_{2-x}O_4$

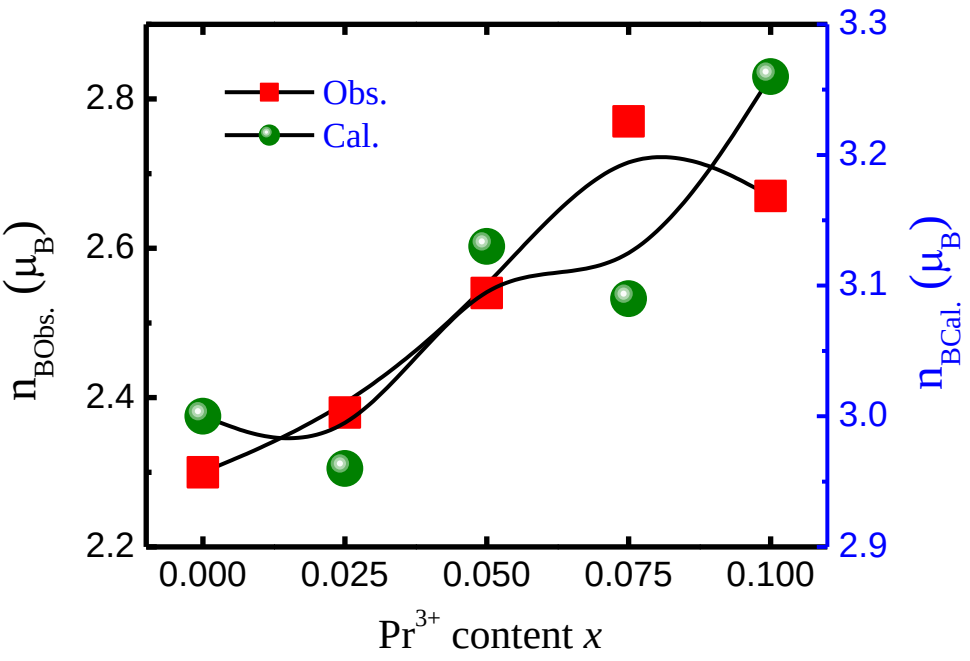

Fig. 5.14: Variation of observed (Obs.) and calculated (Cal.) magneton number with Pr^{3+} content x.

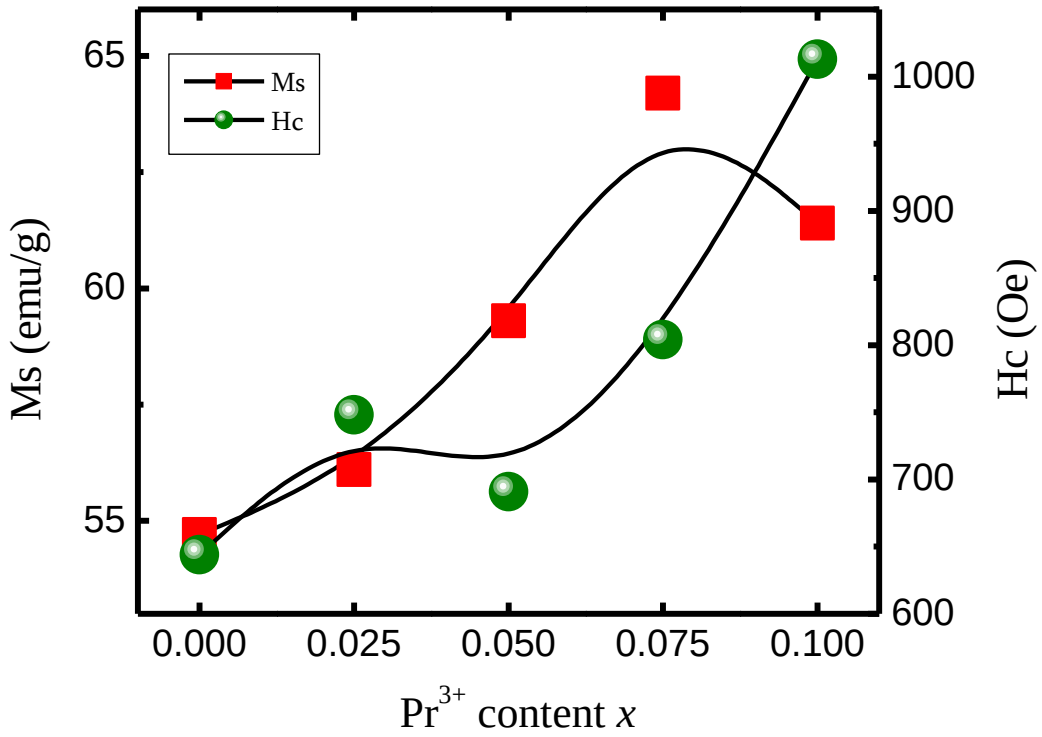

Fig. 5.15: Variation of magnetization and coercivity withPr^{3+}content x.

Chapter # 6

Catalytic Applications of $Ho_xCoFe_{2-x}O_4$ and $Pr_xCoFe_{2-x}O_4$ Ferrite System.

6. A. $Ho_xCoFe_{2-x}O_4$, Ferrite System.

6. A.1. Introduction

Multicomponent reactions (MCR) [135-137] have become important tools for the rapid generation of molecular complexity and diversity with predefined functionality in chemical biology and drug discovery [138-140]. These reactions are often discovered by serendipity, but rational design strategies are now playing an increasing role because of their convergent nature, superior atom economy, and straightforward experimental procedures in the construction of target compounds by the introduction of several diversity elements in a single operation, resulting in substantial minimizations of waste, labor, time, and cost. MCRs, a powerful and virtually reliable target-guided synthetic approach, has extensively been used and applied for the rapid construction of molecular-level complex architectures, and interest from different branches of science is expanding exponentially [141].

Interest in imidazole-containing structures stems from their widespread biological activities and their use in synthetic chemistry. The imidazole ring system is one of the most important substructures found in a large number of natural products and pharmacologically active compounds [142-146]. In recent years, substituted imidazoles are substantially used in ionic liquids [147] that have been given a new approach to 'Green Chemistry'. Triarylimidazole derivatives have many biological activities, for example, herbicidal [148], fungicidal [149], anti-inflammatory [150], and antithrombotic activities [151]. In addition, they are used in photography as photosensitive compound [152]. Literature survey reveals that there are several methods for synthesizing them, mainly using nitriles and esters [153-155] as the

starting materials. The first synthesis of the imidazole core 2,4,5-triphenylimidazoles using 1,2-dicarbonyl compounds aldehydes and ammonia, was proposed by Japp and Radziszewski [156-157]. Subsequently, many other methods for synthesis of this important heterocycle have been published [158-159]. Recently some methods for synthesis of tetra-substituted imidazoles are reported [160]. However, some of these previous methods have suffered from one or more drawbacks like high temperature requirement, highly acidic conditions, and the use of metal cyanides for preparation of the nitrile compounds that limit their utility [161,162]. Some of methods have resorted to harsh conditions (e.g. the formamide synthesis, which requires excess reagents, H_2SO_4 as a condensing agent, 150-200°C, 4-6 h, 40-90% [163-165]. Due to these reasons, the development of mild, efficient and versatile method is still important.

In recent times, several transition metal oxides in the form of nanoparticles were employed as recyclable catalysts for one-pot multicomponent reactions [166]. In general, nanomaterials with natural morphologies containing higher surface area as reactive sites allow them to act as effective catalysts for organic synthesis [167]. These nanoparticles have provided a simplified isolation procedure for the product, with small amounts of catalyst, affording easy recovery and recyclability of the catalyst. In some cases, recovery of the nanoparticles from the reaction mixtures is so difficult that conventional techniques such as filtration or centrifugation are not enough for an efficient recovery. To overcome this issue, the use of magnetic nanoparticles has emerged as a viable solution; their insoluble and paramagnetic nature enables easy and efficient separation of the catalysts from the reaction mixture with an external magnet. Taking into consideration the importance of multicomponent reaction [168,169], we decided to use Ho^{3+} doped $CoFe_2O_4$ nanoparticles as magnetically recoverable and reusable catalyst for the synthesis of 2,4,5-triaryl-1*H*-imidazoles . Herein we wish to report an efficient synthesis of 2,4,5-triaryl-1*H*-imidazoles via one-pot three-component condensat- ion reaction of benzil or benzoin, aromatic aldehydes and ammonium acetate in high yields and short reaction times by using Ho^{3+} doped $CoFe_2O_4$ nanoparticles with as a green, robust and easily recoverable catalyst. (Scheme 1 and 2).

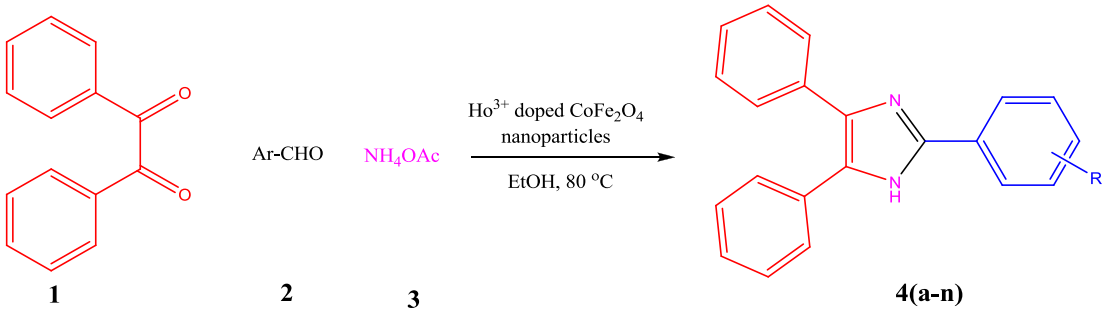

1 **2** **3** **4(a-n)**

Scheme 1. Synthesis of 2,4,5-triarylimidazoles using benzil (**1**), aromatic aldehydes (**2**), and ammonium acetate (**3**) using 5 mol % $Ho_xCoFe_{2-x}O_4$ (x = 0. 05) nanoparticles as catalyst.

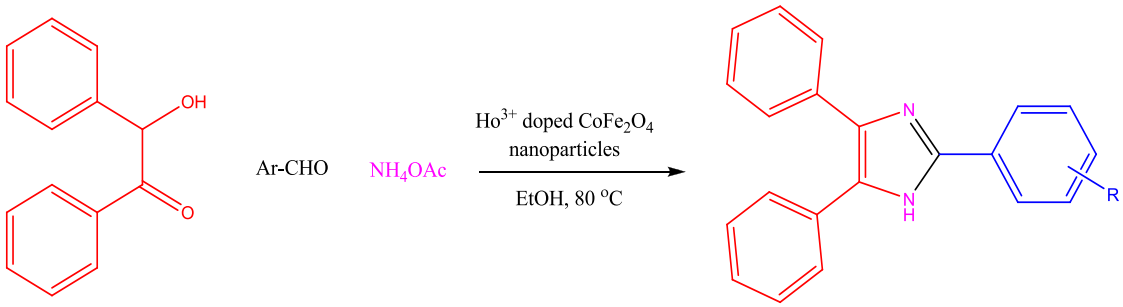

5 **2** **3** **4(a-n)**

Scheme 2. Synthesis of 2,4,5-triarylimidazoles using benzoin (**5**), aromatic aldehydes (**2**) and ammonium acetate (**3**) using 5 mol % $Ho_xCoFe_{2-x}O_4$ (x = 0. 05) nanoparticles as catalyst.

6. A.2. Experimental

6. A.2.1. Chemistry

^{1}H NMR spectra were recorded on a 400 MHz Varian-Gemini spectrometer and are reported as parts per million (ppm) downfield from a tetramethylsilane internal standard. The following abbreviations are used; singlet (s), doublet (d), triplet (t), quartet (q), multiplate (m) and broad (br). Mass spectra were taken with Micromass - QUATTRO-II of WATER mass spectrometer. The purity of the synthesized compounds was checked by TLC. Melting points were determined in capillary tubes and are uncorrected.

6. A.2.2. General procedure for the synthesis of 2,4,5-triaryl-1H-imidazoles 4(a-n)

A mixture of benzil or benzoin (1.0 mmol), aromatic aldehydes (1.0 mmol), ammonium acetate (4.0 mmol), and $Ho_xCoFe_{2-x}O_4$ (x= 0.05) nanoparticles (5 mol %) in ethanol (25 ml) was refluxed (80^oC). The completion of the reaction was checked with TLC (n-hexane: ethyl acetate 4:1). After completion of reaction, the catalyst was magnetically removed from the reaction mixture. The solution was cooled to room temperature and poured on ice-water (50 ml) to get the precipitated solid. It was collected by filtration, washed with water and dried to give the corresponding 2,4,5-triaryl-1*H*-imidazoles. All synthesized compounds were characterized with ^{1}HNMR and mass. Also the melting points recorded and compared with the corresponding literature mp and found to be matching with those.

6. A.2.3. Spectral data for some 2,4,5-triaryl-1H-imidazole deivatives

2,4,5-triphenyl-1*H*-imidazole (4a) Off-white solid; mp 278-280^oC; ^{1}H NMR (400 MHz, DMSO): δ = 7.52-7.60 (m, 6H), 7.69-7.75 (m, 3H), 7.88-7.95 (m, 6H), 8.92 (br, 1H); MS (EI, 70 eV): *m/z* = 296 $[M+H]^+$.

2-(4-methyl phenyl)-4,5-diphenyl-1*H*-imidazole (4b) Off-white solid; mp 231-232 ^oC; ^{1}H NMR (400 MHz, $CDCl_3$) (Fig.6.1): δ = 8.03 - 7.15 (m, 14 H Ar - H), 8.23 (brs, NH), 3.16 (s, 3H,CH3), ES/MS (Fig.6.2) m/z = 312 $[M+H]^+$.

6. A.3. Results and discussion

Ho^{3+} doped $CoFe_2O_4$ nanoparticles were prepared by sol–gel auto-combustion route to achieve homogeneous mixing of the chemical constituents on the atomic scale and better sinterability as reported earlier.

Initially, to study the catalytic efficiency of Ho^{3+} doped $CoFe_2O_4$ nanoparticles, three $Ho_xCoFe_{2-x}O_4$ (x = 0.0, 0.05, and 0.1) nanoparticles were screened to find out best ferrite composition Ho^{3+} doped $CoFe_2O_4$ nanoparticles for synthesis of 2,4,5-triphenyl-1*H*-imidazole (**4a**) as model reaction. The reaction was carried out using benzil (**1**) (1.0 mmol), benzaldehyde (**2**) (1.0 mmol) and ammonium acetate (**3**) (4.0 mmol) in ethanol (25 mL) as solvent using Ho^{3+} doped $CoFe_2O_4$ nanoparticles (20 mol %) as catalyst (Table 6.1). The title compound **4a** was isolated

with 98% yield in the presence of $Ho_xCoFe_{2-x}O_4$ (x= 0.05) nanoparticles in shorter reaction time (10 min) than with other nanoparticles $Ho_xCoFe_{2-x}O_4$ (x= 0.0 and 0.1). After deciding the nanoparticles, the amount of nanoparticles (catalyst load) was optimized for model reaction (**4a**). The catalyst was added in amounts of 30, 20, 15, 10, 5, and 0 mol %. The results indicate that increase in amount of catalyst from 20 mol % to 30 mol % did not show any change in yield ant time of reaction (Table 6.1, Entry 4). Also, when catalyst load was decreased sequentially from 20 mol % to 5 mol %, the results indicate, there were no change in yield and time of the reaction. When no catalyst was added (0 mol %) for model reaction, there was only small amount (Yield 25 %) of product obtained after 180 min. Therefore, 5 mol % of the catalyst $Ho_xCoFe_{2-x}O_4$ (x= 0.05) nanoparticles was assumed to ensure the best yield (98 %) in short reaction time (10 min). Thus, our results make the process under study more attractive and interesting from the viewpoint of economy and simplicity.

To assess the generality of this approach, various aromatic aldehydes were reacted with benzil and ammonium acetate under optimized conditions to obtain 2,4,5-triaryl-1*H*-imidazoles **4(a-n)** (Scheme 1). As shown in Table 6.2, aldehydes containing either electron-withdrawing or electron- releasing groups gave the corresponding 2,4,5-triaryl-1*H*-imidazoles (**3a-3h**) in high yields. In addition, it was specifically considerable that aryl aldehydes bearing electron-releasing groups such as $-CH_3$, $-OCH_3$, -OH, and $-N(CH_3)_2$ reacted very smoothly in short reaction times and higher yields (Table 6.2, **4b-4e**) while electron-withdrawing substitutions such as -Cl and -CN (Table 6.2, **4f-4h**) showed less reactivity in this condensation reaction. As shown in Table 6.2, these condensation reactions also proceed suitably when different heteryl-aromatic aldehydes were used in the synthesis of 2,4,5-triaryl-1*H*-imidazoles derivatives (**4i-4n**) in short reaction times and high yields.

1,2-diketones (like benzil) are usually prepared from the α-hydroxy ketones (like benzoin) catalyzed by various oxidants. Some of these catalysts are toxic, costly and also required the tedious experimental procedures [170]. To avoid the preparation of starting material 1,2-diketones like benzil, the synthesis of 2,4,5-triphenyl-1*H*-imidazole **4a** was studied using benzoin (**5**) (1.0 mmol), benzaldehyde (**2**) (1.0 mmol) and ammonium acetate (**3**) (4.0 mmol). Surprisingly, using the similar reaction conditions, 2,4,5-triphenyl-1*H*-imidazoles **4a** was isolated in 93 % yield within short reaction time (15 min). Encouraged by this result, we extended the methodology for

synthesis of various 2,4,5-triaryl-1*H*-imidazoles **4(a-n)** using benzoin, various aromatic aldehydes and ammonium acetate (Scheme 2). The yields obtained were in the range of 84 % to 95 % (Table 6.2). Similar trends were also observed for Scheme 2, that is, aryl aldehydes bearing electron-releasing groups gave the corresponding 2,4,5-triaryl-1*H*-imidazoles in higher yield as compared with aryl aldehydes bearing electron-withdrawing substitutions.

Catalyst reusability is of major concern in heterogeneous catalysis. The recovery and reusability of the catalyst was investigated in this reaction for model reaction (**4a**). The reaction was carried out using benzil (**1**) (1.0 mmol), benzaldehyde (**2**) (1.0 mmol) and ammonium acetate (**3**) (4.0 mmol) in ethanol (25 mL) as solvent using 5 mol % of $Ho_xCoFe_{2-x}O_4$ (x= 0.05) nanoparticles as catalyst. After completion of reaction (monitored by TLC), catalyst recycling was achieved by fixing the catalyst magnetically at the bottom of the flask with a strong magnet, after which the solution was taken off with a pipette, the solid washed twice with acetone and the fresh substrate dissolved in the same solvent was introduced into the flask, allowing the reaction to proceed for the next run. The catalyst was consecutively reused five times without any noticeable loss of its catalytic activity (Cycle number and yield of **4a**: 1, 98 %; 2, 98 %; 3, 97 %; 4, 97 %; 5, 96 %). These catalysts are highly magnetic and their saturation magnetization values are found to be 67.05 and 68.55 emu/g, which are much higher than other reported magnetic catalysts. Therefore, they could be easily and almost completely separated by an external magnet which is of a great advantage for a heterogeneous catalyst.

The work-up of these reactions was very clean and required only pouring of the reaction mixture over ice-water after removing the catalyst with the help of magnet, and the desired products were thus isolated with high purity. To the best of our knowledge, the synthesis of 2,4,5-triaryl-1*H*-imidazoles derivatives using Ho^{3+} doped $CoFe_2O_4$ nanoparticles as catalyst has not been reported previously. The catalyst is not only efficient but also mild and easy to handle.

6. B. $Pr_xCoFe_{2-x}O_4$ Ferrite System.

6. B.1. Introduction

Multicomponent reactions (MCRs) [135-137] have become important tools for the efficient and rapid generation of structurally complex target compounds with predefined functionality in chemical biology and drug discovery [138-140]. These reactions are often discovered by serendipity, but rational design strategies are now playing an increasing role because of their convergent nature, superior atom economy, and straightforward experimental procedures in the construction of target compounds by the introduction of several diversity elements in a single operation, resulting in substantial minimizations of waste, labor, time, and cost. MCRs, a powerful and virtually reliable target-guided synthetic approach, has extensively been used and applied for the rapid construction of molecular-level complex architectures, and interest from different branches of science is expanding exponentially [141].

Pyrrole is one of the important heterocycle owing to its antitumor, anti-infammatory, antibacterial, antioxidant, and antifungal properties [171-173]. In addition, pyrrole derivatives are also particularly important in materials science [174]. These utilities continue to drive the interest in the development of new synthetic methods for pyrrole derivatives. The traditional routes to their synthesis are multistep reactions, as illustrated by the Paal-Knorr cyclization of 1,4-dicarbonyls with ammonia or primary amines [175,176]. This method suffer from several drawbacks, such as stepwise reactions, narrow substrate scope, and lacking the variation of substituents on the pyrrole ring due to the unity of starting materials. For all these reasons, the search for new atom-economical and green synthetic methods, which avoid the use of special reagents, cost, time, and steps from readily available and inexpensive materials for the synthesis of multisubstituted pyrrole derivatives, has attracted much attention [177,178]. Combining the advantages of multicomponent reaction and the magnetic nanocatalysts, the development of a new atom-efficient and environmentally friendly synthetic procedure for the efficient preparation of structurally diverse pyrroles is therefore an interesting challenge.

With the increasing demand for ‘‘green chemistry’’, the use of efficient and recoverable supported heterogeneous catalysts becomes one of the most important topics of research in synthetic organic chemistry, material science, and engineering.

One of the most attractive alternatives to catalyst are use magnetic ferrites, which have witnessed increasing popularity due to their high surface areas and improved dispersability in the reaction medium [179,180]. Specifically, magnetic ferrite catalysts can be recovered using an external magnet due to the paramagnetic character. This makes the removal and recycling of the catalyst much easier than filtration and centrifugation. Inspired by the utilization of Pr^{3+} doped $CoFe_2O_4$ as magnetically recoverable and reusable catalyst in the field of multicomponent reactions [181-191], herein we wish to report an efficient one-pot four-component synthesis of multisubstituted pyrrole derivatives via reaction of amines, aldehydes, acetylacetone and nitromethane in high yields and short reaction times by using Pr^{3+} doped $CoFe_2O_4$ with as a green, robust and easily recoverable catalyst (Scheme 3).

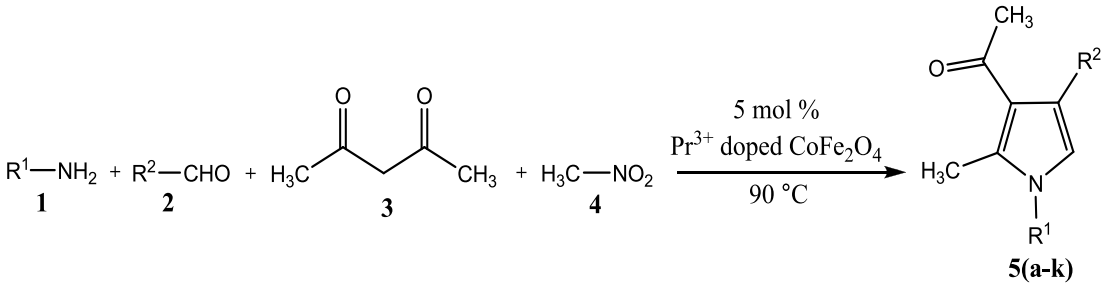

Scheme.3. Synthesis of multisubstituted pyrroles **5(a-k)**.

6. B.2. Experimental

6. B.2.1. Chemicals and apparatus

All solvents, chemicals, and reagents were purchased from Merck, Avra Synthesis and Sigma-Aldrich chemical companies. The purity of the synthesized compounds was checked by TLC. Melting points were determined in capillary tubes and are uncorrected. ^{1}H NMR (400 MHz) and ^{13}C NMR (100 MHz) spectra were recorded on a Varian-Gemini spectrometer and are reported as parts per million (ppm) downfield from a tetramethylsilane internal standard. The following abbreviations are used; singlet (s), doublet (d), triplet (t), quartet (q), multiplate (m) and broad (br). Mass spectra were taken with Micromass- QUATTRO-II of WATER mass spectrometer.

6. B.2.2 General procedure for the synthesis of multisubstituted pyrrole derivatives 5(a-k)

The mixture of amine **1** (1.0 mmol), aldehyde **2** (1.0 mmol), acetylacetone **3** (1.0 mmol), nitromethane **4** (1.0 ml) and $Pr_xCoFe_{2-x}O_4$ (x= 0.05) (5 mol %) was stirred at 90 ^oC (Scheme 3). The completion of the reaction was checked by TLC (n-hexane: ethyl acetate 4:1). Upon completion of the reaction, the reaction mixture was cooled to room temperature and 10 ml of ethyl acetate was added. The pyrrole derivatives were dissolved in ethyl acetate and the catalyst was separated magnetically, washed with ethyl acetate and used for subsequent cycles. Pure products were obtained by evaporation of the solvent, followed by recrystallization from ethanol. The melting points were recorded and compared with the corresponding literature melting point and found to be matching with those.

6. B.2.3. Spectral data for some multisubstituted pyrrole derivatives

1-(4-hydroxyphenyl)-2-methyl-4-phenyl-3-acetyl-1H-pyrrole (5f): Orange solid; mp 150-152 ^oC; ^1H NMR (400 MHz, $CDCl_3$) (Fig. 6.3): δ = 2.07 (s, 3H, $-CH_3$), 2.44 (s, 3H, CH_3-C=O-), 4.70 (br, 1H, Ar-OH,), 6.24 (s, 1H, -CH- of pyrrole), 6.90-7.40 (m, 4H, ArH), 7.45-7.53 (m, 5H, ArH); MS (ES-MS) (Fig. 6.4): *m/z* = 292.24 $[M+H]^+$.

6. B.3. Results and discussion

Pr^{3+} doped $CoFe_2O_4$ ferrites were prepared by sol–gel auto-combustion route to achieve homogeneous mixing of the chemical constituents on the atomic scale and better sinterability as reported earlier.

Initially, to study the catalytic efficiency of pr^{3+} doped $CoFe_2O_4$, all the four $Pr_xCoFe_{2-x}O_4$ (x = 0.0, 0.025, 0.05 and 0.1) ferrites were screened to find out best ferrite composition using synthesis of 2-methyl-1,4-diphenyl-3-acetyl-1H-pyrrole (**5a**) as model reaction. The reaction was carried out with aniline **1** (1.0 mmol), benzaldehyde **2** (1.0 mmol), acetylacetone **3** (1.0 mmol), nitromethane **4** (1.0 ml) using $Pr_xCoFe_{2-x}O_4$ (x = 0.0, 0.025, 0.05 and 0.1) frites (20 mol %) as catalyst (Table 6.3). The title compound **5a** was isolated with 95 % yield in the presence of $Pr_xCoFe_{2-x}O_4$ (x= 0.05) in shorter reaction time (1.5 h) than with other ferrites i.e. $Pr_xCoFe_{2-x}O_4$

(x= 0.0, 0.025 and 0.1). Thus, $Pr_xCoFe_{2-x}O_4$ (x= 0.05) was best catalyst among screened Pr^{3+} doped $CoFe_2O_4$ ferrites in terms of yield and reaction kinetic.

After deciding the catalyst, the amount of $Pr_xCoFe_{2-x}O_4$ (x= 0.05) i.e. catalyst load was optimized for model reaction (**5a**). The catalyst was added in amounts of 30, 20, 15, 10, 5, and 0 mol %. The results indicate that increase in amount of catalyst from 20 mol % to 30 mol % did not show any change in yield and time of reaction (Table 6.3, Entry 5). Also, when catalyst load was decreased sequentially from 20 mol % to 5 mol %, the results indicate, there were no change in yield and time of the reaction (Table 6.3, Entries 6, 7 and 8). When no catalyst was added (Table 6.3, Entry 9) for model reaction (**5a**), there was only small amount (yield 15 %) of product obtained after 6 h. Therefore, 5 mol % of the $Pr_xCoFe_{2-x}O_4$ (x= 0.05) catalyst was assumed to ensure the best yield (95 %) in short reaction time (1.5 h). Thus, our results make the process under study more attractive and interesting from the viewpoint of economy and simplicity.

Following the optimized reaction conditions, a variety of multisubstituted pyrrole derivatives **5(a-k)** were synthesized (Scheme 3) in good yields (Table 6.4). As shown in Table 6.4, anilines bearing either electron-withdrawing or electron-releasing groups gave the corresponding pyrroles (**5a-5f**) in high yields (85-97 %). In addition, it was specifically considerable that anilines bearing electron-releasing groups such as $-CH_3$ (**5e**, yield 97 %) and -OH (**5f**, yield 96 %) reacted very smoothly and gave higher yields (Table 6.4, Entries 5 and 6) while electron-withdrawing substitutions such as -F (**5b**, yield 90 %), -Cl (**5c**, yield 88 %) and $–NO_2$ (**5d**, yield 85%) showed less reactivity in this cyclization reaction (Table 6.4, Entries 2, 3 and 4). Similarly, benzaldehydes bearing electron-withdrawing substituents such as -F (**5g**, yield 85 %), -Cl (**5h**, yield 87 %) and NO_2 (**5i**, yield 83) gave less yields when compared with electron-donating substituents such as $-CH_3$ (**5j**, yield 93 %) and -OH (**5k**, yield 95 %) (Table 6.4, Entries 7-11). Thus, these successful results greatly proved that this procedure was extendable to various substrates in four-component reactions, generating moderate to high yields of the multisubstituted pyrrole derivatives **5(a-k)**.

Catalyst reusability is of major concern in heterogeneous catalysis. The recovery and reusability of the catalyst was investigated in this reaction for model reaction **5a**. The reaction mixture of aniline **1** (1.0 mmol), benzaldehyde **2** (1.0 mmol), acetylacetone **3** (1.0 mmol), nitromethane **4** (1.0 ml) and 5 mol % of

$Pr_xCoFe_{2-x}O_4$ (x= 0.05) as catalyst was refluxed at 90^oC. After completion of reaction (monitored by TLC), the reaction mixture was cooled to room temperature. The compound was dissolved in 10 ml ethyl acetate and catalyst recycling was achieved by fixing the catalyst magnetically at the bottom of the flask with a strong magnet, after which the solution was taken off with a pipette. The solid i.e. catalyst was washed twice with ethyl acetate and dried to remove residual solvents, and then reused directly in the model reaction for next round without further purification. The catalyst was consecutively reused five times without any noticeable loss of its catalytic activity (Cycle number and yield of **5a**: 1, 95 %; 2, 95 %; 3, 94 %; 4, 94 %; 5, 93 %). $Pr_xCoFe_{2-x}O_4$ (x= 0.05) is highly magnetic and their saturation magnetization values are found to be 59.25 emu/g [194], which are much higher than other reported magnetic catalysts. Therefore, they could be easily and almost completely separated by an external magnet which is of a great advantage for a heterogeneous catalyst.

The work-up of these reactions was very clean as there were no tedious steps were involved for obtaining the desired compounds in pure form and in good yields. After recrystallization, compounds have been obtained in high purity, thus no chromatographic techniques were used for purification of the compounds. The catalysts were also easily separated from reaction mixture with the help of magnet. To the best of our knowledge, the synthesis of multisubstituted pyrrole derivatives **5(a-k)** using Pr^{3+} doped $CoFe_2O_4$ as catalyst has not been reported previously. The catalyst is not only efficient but also mild and easy to handle.

A plausible mechanism for the formation of pyrrole derivatives is proposed in Scheme 4. The intermediates (Z)-4-(phenylamino) pent-3-en-2-one (**A**) from aniline **1** and acetylacetone **3** and (E)-(2-nitrovinyl) benzene (**B**) from benzaldehyde **2** and nitromethane **4** could be generated in the presence of a $Pr_xCoFe_{2-x}O_4$ (x= 0.05). These two intermediates reacted via Michael addition, followed by intramolecular cyclization with the elimination of nitroxyl (HNO) and water to lead to the final product **5** [192-194].

Table 6.1 Optimization of reaction conditions and catalyst load (mol %) of Ho^{3+} doped $CoFe_2O_4$ nanoparticles for the synthesis of 2,4,5-triphenyl-1*H*-imidazole (**4a**).

Entry	Catalyst (nanoparticles)	Catalyst loading (mol %)	Time (min)	Yield of 4a, [a]%
1	$Ho_xCoFe_{2-x}O_4$ (x = 0.0)	20	30	78
2	$Ho_xCoFe_{2-x}O_4$ (x = 0. 05)	20	10	98
3	$Ho_xCoFe_{2-x}O_4$ (x =0.1)	20	45	85
4	$Ho_xCoFe_{2-x}O_4$ (x = 0. 05)	30	10	98
5	$Ho_xCoFe_{2-x}O_4$ (x = 0. 05)	15	10	97
6	$Ho_xCoFe_{2-x}O_4$ (x = 0. 05)	10	10	98
7	$Ho_xCoFe_{2-x}O_4$ (x = 0. 05)	5	10	98
8	$Ho_xCoFe_{2-x}O_4$ (x = 0. 05)	0 (No catalyst)	180	25

[a] Hereinafter, isolated yield of pure product.

Table 6. 2. Synthesis 2,4,5-triaryl-1*H*-imidazoles **4(a-n)** using benzil or benzoin, aromatic aldehydes and ammonium acetate using 5 mol % $Ho_xCoFe_{2-x}O_4$ (x = 0. 05) nanoparticles in ethanol.

Entry	Aromatic aldehydes	Reaction temp (^oC)	Time (min)		[a] % Yield	
			Benzil	Benzoin	Benzil	Benzoin
4a	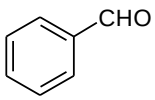	80	10	15	98	93
4b	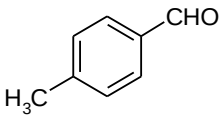	80	15	20	95	90
4c	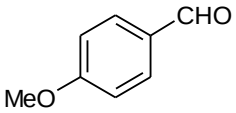	80	10	15	98	92
4d	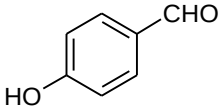	80	10	20	96	90
4e	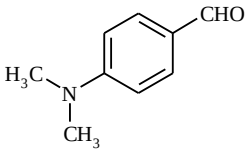	80	15	15	98	95
4f	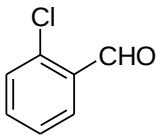	80	20	25	92	85

4g	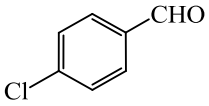	80	20	25	90	88
4h	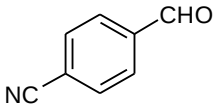	80	25	25	88	84
4i	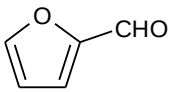	80	20	25	98	92
4j	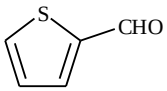	80	20	20	95	90
4k	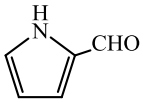	80	20	25	90	86
4l	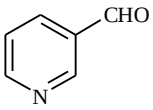	80	20	25	95	92
4m	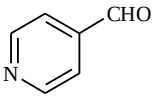	80	20	25	96	90
4n	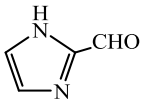	80	20	30	92	88

[a] Hereinafter, isolated yield of pure product.

Table 6.3 Optimization of reaction conditions and catalyst load (mol %) of Pr^{3+} doped $CoFe_2O_4$ for the synthesis of compound **5a**.

Entry	Catalyst	Catalyst (mol %)	Time (h)	*% Yield of 5a
1	$Pr_xCoFe_{2-x}O_4$ (x = 0.0)	20	4	70
2	$Pr_xCoFe_{2-x}O_4$ (x = 0.025)	20	5	72
3	$Pr_xCoFe_{2-x}O_4$ (x = 0. 05)	20	1.5	95
4	$Pr_xCoFe_{2-x}O_4$ (x =0.1)	20	4.5	78
5	$Pr_xCoFe_{2-x}O_4$ (x = 0. 05)	30	1.5	95
6	$Pr_xCoFe_{2-x}O_4$ (x = 0. 05)	15	1.5	95
7	$Pr_xCoFe_{2-x}O_4$ (x = 0. 05)	10	1.5	95
8	$Pr_xCoFe_{2-x}O_4$ (x = 0. 05)	5	1.5	95
9	No catalyst	-	6	15

* Hereinafter, isolated yield of pure product.

Table 6.4 One-pot four-component synthesis of multisubstituted pyrroles **5(a-k)**.

Entry	R^1	R^2	Product	Time (h)	*% Yield	Melting Point (°C)	
						Observed	Literature
1	C_6H_5	C_6H_5	**5a**	1.5	95	104-106	106-107 [30]
2	4-*F*-C_6H_4	C_6H_5	**5b**	2	90	132-124	130-131 [30]
3	4-*Cl*-C_6H_4	C_6H_5	**5c**	2.5	88	126-128	127-128 [30]
4	4-NO_2-C_6H_4	C_6H_5	**5d**	2.5	85	170-172	171-172 [30]
5	4-CH_3-C_6H_4	C_6H_5	**5e**	1	97	106-108	109-111 [30]
6	4-*OH*-C_6H_4	C_6H_5	**5f**	1.5	96	150-152	155-158 [31]
7	C_6H_5	4-*F*-C_6H_4	**5g**	2	85	128-130	127-128 [32]
8	C_6H_5	4-*Cl*-C_6H_4	**5h**	2	87	148-150	146-147 [32]
9	C_6H_5	4-NO_2-C_6H_4	**5i**	2.5	83	Oil	Oil [30]
10	C_6H_5	4-CH_3-C_6H_4	**5j**	1	93	Oil	Oil [32]
11	C_6H_5	4-*OH*-C_6H_4	**5k**	1.5	95	174-176	170-171 [31]

* Hereinafter, isolated yield of pure product.

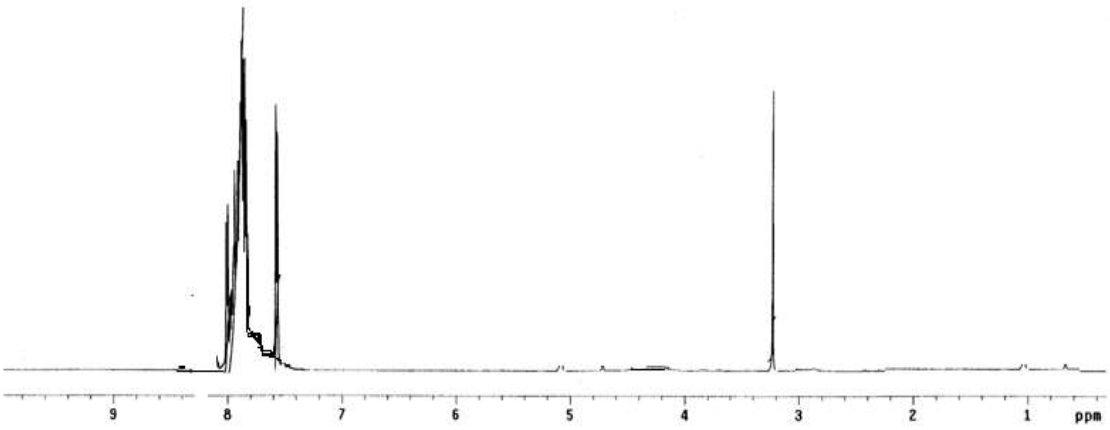

Fig. 6.1: ^{1}H NMR spectrum of 2-(4-methyl phenyl)-4,5-diphenyl-1*H*-imidazole (4b)

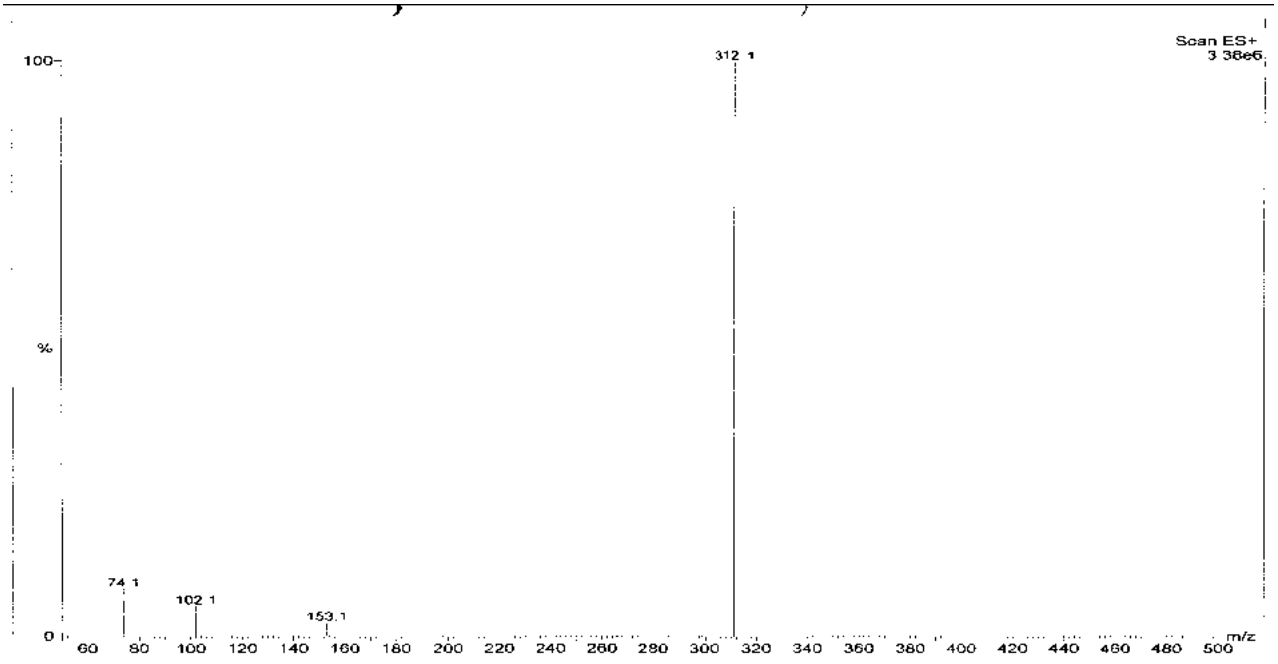

Fig. 6.2: Mass spectrum of 2-(4-methyl phenyl)-4,5-diphenyl-1*H*-imidazole (4b)

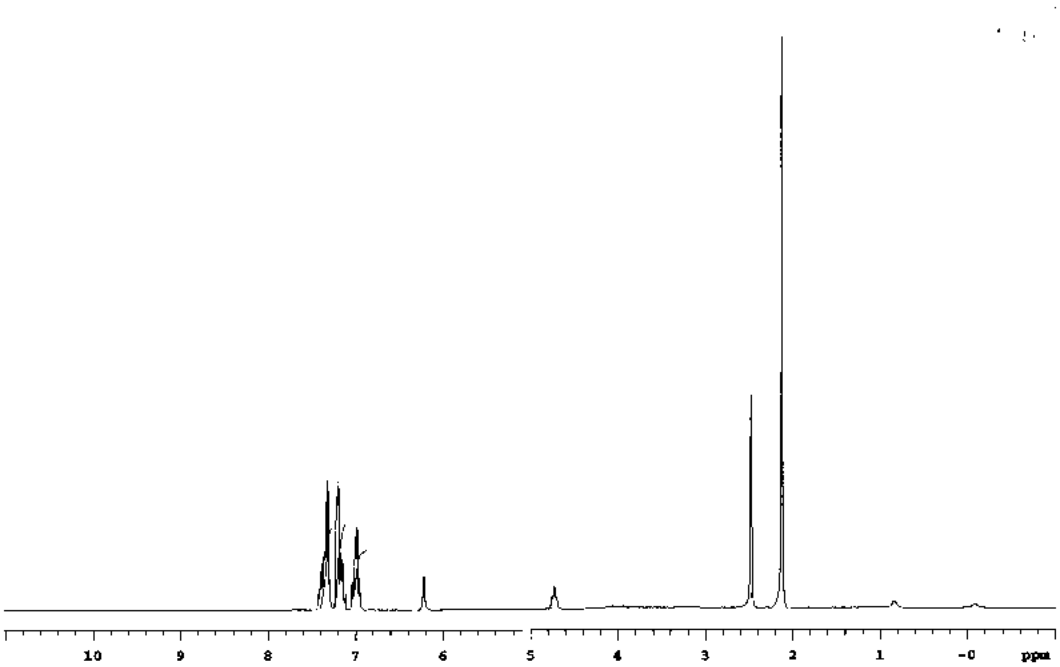

Fig.6.3: ^{1}H NMR spectrum of 1-(4-hydroxyphenyl)-2-methyl-4-phenyl-3-acetyl-1H-pyrrole (5f)

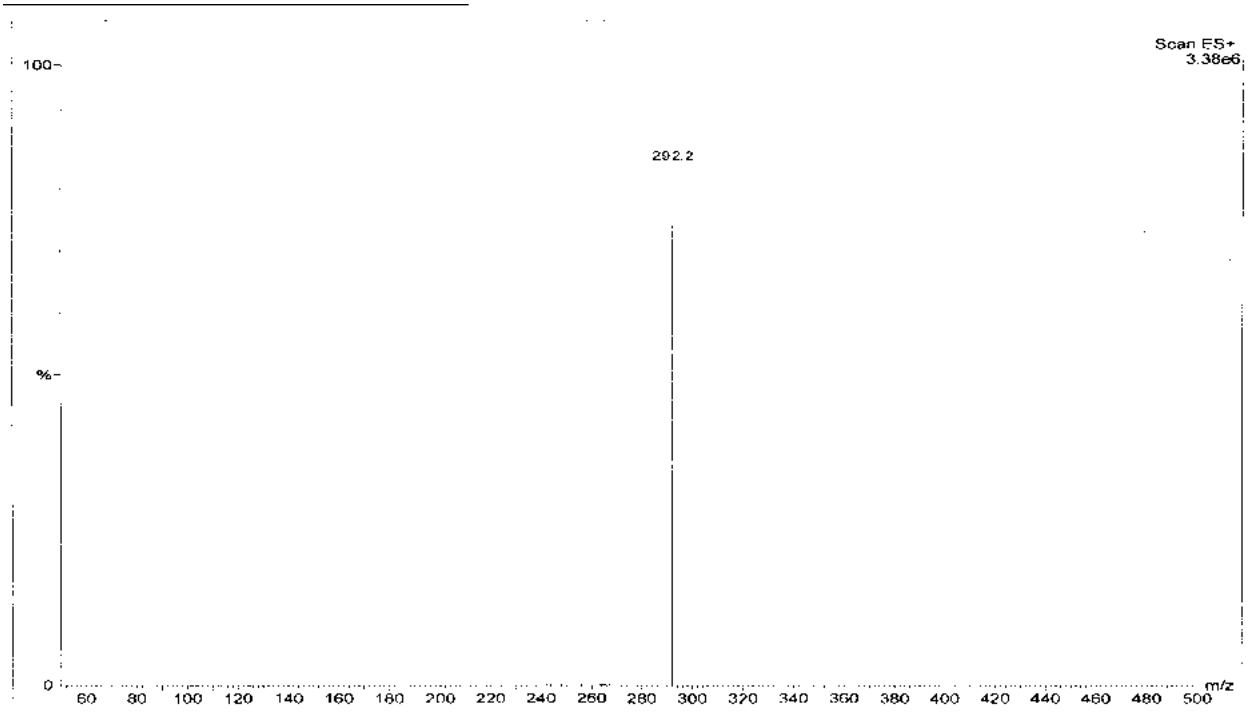

Fig.6.4: Mass spectrum of 1-(4-hydroxyphenyl)-2-methyl-4-phenyl-3-acetyl-1H-pyrrole (5f)

Chapter # 7

Conclusion

We conclude that Ho^{3+} is a potential candidate to be substituted in $CoFe_2O_4$ nanoparticles material systems, which certainly helps to modified structural and enhance magnetic properties. The XRD pattern of $x \geq 0.075$ sample consists of superposition of the cubic spinel and ortho ferrite patterns indicating the two-phase co-existing region. With the addition of Ho^{3+} contents for Fe^{3+} in $Ho_xCoFe_{2-x}O_4$ compound grain size decreased with the substitution degree of Ho^{3+}. Thus the rare earth element holmium acts as a grain growth inhibitor. Due to the larger bond energy of Ho^{3+}-O^{2-} as compared to Fe^{3+}-O^{2-}, more energy is needed to force Ho^{3+}ions enter into the lattices and form the bond of Ho^{3+}-O^{2-}. The present work to tailor the magnetic properties of the $CoFe_2O_4$, Fe^{3+} ions are partially substituted by trivalent ions of rare earth element Ho^{3+}, aiming to occupy the spin down sites and, consequently, to increase the net magnetization. The effect of rare earth element Ho^{3+} substitution on the magnetic properties of the material is in general a positive one. With the substitution of Ho^{3+} ions in $CoFe_2O_4$, saturation magnetization increased from 61.06 to 74.05 emu/g, remanent magnetization increased from 28.5 to 34.6 emu/g, this may be probably due to the larger magnetic moment of Ho^{3+} ions and enhanced exchange interaction. Coercivity of $CoFe_2O_4$ increased from 1269 to 1591Oe with Ho^{3+} substitution. Coercivity follows $Hc \propto 1/r$ behavior.

We have developed a highly efficient one-pot three-component method for the synthesis of 2,4,5-triaryl-1*H*-imidazole derivatives from benzil or benzoin, aromatic aldehydes and ammonium acetate in ethanol using Ho^{3+} doped $CoFe_2O_4$ nanoparticles. Advantages of the proposed procedure include simplicity, high yield, short reaction time, ease of separation and reusability of the magnetic catalyst. The method overcomes the earlier disadvantages and therefore will be of general use and interest to synthetic chemists.

It can be concluded from this research; the sol–gel combustion method has

been justified to be a simple and powerful procedure for synthesizing rare earth Pr^{3+} substituted $CoFe_2O_4$ nanoparticles from metal nitrates using citric acid as the fuel with reduction of time consumption. Sintered $Pr_xCoFe_{2-x}O_4$ nano-sized crystallite ferrite samples show the formation of spinel cubic crystal structure with appearance of small peaks represented a secondary phase due to the presence of rare earth Pr^{3+}ions.The unit cell parameter increases linearly with the increase of Pr^{3+}substitution due to its larger ionic radii as compared to Fe^{3+} ions. The structural characterization of the powders using XRD and TEM confirmed the formation of nanosize particles. The occupation number of individual atoms over the A and B sites are affected by the variation of the Pr^{3+} substitution. Pr^{3+} ions enter into the B site which increases almost linearly with x. Co^{2+} ions shows preference towards B site, whereas Fe^{3+} ions are distributed over both A- and B- sites for the whole compositional range. The variation of the theoretical and experimental lattice parameter is in a good agreement with each other. The system maintains ferrimagnetic ordering at room temperature for the whole range of the composition studied. Substitution of Pr^{3+} ions into the cobalt ferrite system can be utilized for enhancement of both saturation magnetization (Ms) and coercive field (Hc). Substitution of Pr^{3+} ions in the spin-down states (4e, 4f1 and 4f2) may lead to an increase in the net magnetization. Pr^{3+} substituted cobalt ferrite samples exhibit higher coercivities than that of pure cobalt ferrite due to higher magnetocrystalline anisotropy.

We have developed a highly efficient one-pot four-component method for the synthesis of multisubstituted pyrrole derivatives from amines, aldehydes, acetylacetone and nitro methane using $Pr_xCoFe_{2-x}O_4$ (x= 0.05) as heterogenous catalyst. A wide range of amines and aldehydes can be tolerated, giving the structural diversity of pyrrole derivatives in good to excellent yields. Also, method overcomes the earlier disadvantages and therefore will be of general use and interest to synthetic chemists. Moreover, the catalysts could be easily recovered and reused five times without significant loss of activity, showing good potential for industrial application.

Chapter # 8

References

1. Berkovsky, B. M., Medvedev, V. F., and Krakov, M. S. (1993). Magnetic fluids. Oxford Univ. Press.
2. Charles, S.W., Popplewell, J. (1986). Properties and applications of magnetic liquids Hand Book of Magnetic Materials (vol 2), ed K H J Buschow
3. De Teresa, J. M., Ibarra, M., Algarabel, P., Ritter, C., Marquina, C., Blasco, J., ... and Arnold, Z. (1997). Evidence for magnetic polarons in the magnetoresistive perovskites. Nature, 386(6622), 256-259.
4. Alonso, J. A., Martinez, J. L., Martínez-Lope, M. J., Casais, M. T., & Fernandez-Diaz, M. T. (1999). Room Temperature Magnetoresistance and Cluster-Glass Behavior in the $Tl_{2-x}Bi_xMn_2O_7$ ($0 \leq x \leq 0.5$) Pyrochlore Series. Physical review letters, 82(1), 189-192.
5. Philip, J., & Kutty, T. R. N. (1999). Colossal magnetoresistance of oxide spinels, $Co_xMn_{3-x}O_4$. Materials Letters, 39(6), 311-317.
6. Belayachi, A., Dormann, J. L., and Nogues, M. (1998). Critical analysis of magnetically semi-disordered systems: critical exponents at various transitions. Journal of Physics: Condensed Matter, 10(7), 1599.
7. Dormann, J. L., and Nogues, M. (1990). Magnetic structures in substituted ferrites. Journal of Physics: Condensed Matter, 2(5), 1223.
8. Gabay, M., and Toulouse, G. (1981). Coexistence of spin-glass and ferromagnetic orderings. Physical Review Letters, 47(3), 201.
9. Dho, J., Kim, W. S., and Hur, N. H. (2002). Reentrant spin glass behavior in Cr-doped perovskite manganite. Physical review letters, 89(2), 027202.
10. Mydosh, J. A. (1993). Spin glasses: An experimental introduction (125).London: Taylor and Francis.
11. Rezlescu, N., Rezlescu, E., Pasnicu, C., and Craus, M. L. (1994). Effects of the rare-earth ions on some properties of a nickel-zinc ferrite. Journal of Physics: Condensed Matter, 6(29), 5707.

12. Yan, C., Cheng, F., Peng, Z., Xu, Z., and Liao, C. (1998). Fabrication and magnetic investigation of Y or Gd containing $CoFe_2O_4$ nanocrystalline films.Journal of applied physics, 84, 5703-5708.
13. Bhowmik, R. N., and Ranganathan, R. (2002). Anomaly in cluster glass behaviour of $Co_{0.2}Zn_{0.8}Fe_2O_4$ spinel oxide. Journal of magnetism and magnetic materials, 248(1), 101-111.
14. Bhowmik, R. N., Ranganathan, R., and Nagarajan, R. (2006). Coexistence of spin glass and superparamagnetism with ferrimagnetic order in polycrystalline spinel $Co_{0.2}Zn_{0.8}Fe_{1.95}Ho_{0.05}O_4$. Journal of magnetism and magnetic materials, 299(2), 327-337.
15. Thant, A. A., Srimala, S., Kaung, P., Itoh, M., Radzali, O., and Fauzi, M. A. (2010). Low temperature synthesis of $MgFe_2O_4$ soft ferrite nanocrystallites. Journal of the Australian Ceramic Society, 46(1), 11-14.
16. Abbas, T., Khan, Y., Ahmad, M., and Anwar, S. (1992). X-ray diffraction study of the cation distribution in the Mn-Zn-ferrites. Solid state communications, 82(9), 701-703.
17. Hussain, A., Abbas, T., and Niazi, S. B. (2013). Preparation of $Ni_{1-x}Mn_xFe_2O_4$ ferrites by sol–gel method and study of their cation distribution.Ceramics International, 39(2), 1221-1225.
18. Goldman, A. (2006). Modern ferrite technology (2nd ed), New York: Springer Science & Business Media.
19. Peng, Z., Fu, X., Ge, H., Fu, Z., Wang, C., Qi, L., and Miao, H. (2011). Effect of Pr^{3+} doping on magnetic and dielectric properties of Ni–Zn ferrites by "one-step synthesis". Journal of Magnetism and Magnetic Materials, 323(20), 2513-2518.
20. Bhandare, M. R., Jamadar, H. V., Pathan, A. T., Chougule, B. K., and Shaikh, A. M. (2011). Dielectric properties of Cu substituted $Ni_{0.5-x}Zn_{0.3}Mg_{0.2}Fe_2O_4$ ferrites. Journal of Alloys and Compounds, 509(6), L113-L118.
21. Charles, S. W., and Popplewell, J. (1982). Properties and applications of magnetic liquids. Endeavour, 6(4), 153-161.
22. Merbach, A. E., and Tóth, É. (Eds.). (2001). The chemistry of contrast agents in medical magnetic resonance imaging (Vol. 46). Chichester (W. Sx.) etc.: Wiley.

23. Hilger, I., Andra, W., Bahring, R., Daum, A., Hergt, R., and Kaiser, W. A. (1997). Evaluation of temperature increase with different amounts of magnetite in liver tissue samples. Investigative radiology, 32(11), 705-712.
24. Pardavi-Horvath, M. (2000). Microwave applications of soft ferrites. Journal of Magnetism and Magnetic Materials, 215, 171-183.
25. Stojanovic, G., Damnjanovic, M., Desnica, V., Zivanov, L., Raghavendra, R., Bellew, P., and Mcloughlin, N. (2006). High-performance zig-zag and meander inductors embedded in ferrite material. Journal of Magnetism and Magnetic Materials, 297(2), 76-83.
26. Li, Z. W., Guoqing, L., Chen, L., Yuping, W., and Ong, C. K. (2006). Co^{2+} Ti^{4+} substituted Z-type barium ferrite with enhanced imaginary permeability and resonance frequency. Journal of applied Physics, 99(6), 3905.
27. Feng, Y. B., Qiu, T., Shen, C. Y., and Li, X. Y. (2006). Electromagnetic and absorption properties of carbonyl iron/rubber radar absorbing materials. Magnetics, IEEE Transactions on, 42(3), 363-368.
28. Li, B. W., Shen, Y., Yue, Z. X., and Nan, C. W. (2006). Enhanced microwave absorption in nickel/hexagonal-ferrite/polymer composites. Applied physics letters, 89(13), 2504.
29. Che, R. C., Zhi, C. Y., Liang, C. Y., and Zhou, X. G. (2006). Fabrication and microwave absorption of carbon nanotubes /$CoFe_2O_4$ spinel nanocomposite. Applied Physics Letters, 88(3), 33105-33105.
30. Xiang, C., Pan, Y., Liu, X., Sun, X., Shi, X., and Guo, J. (2005). Microwave attenuation of multiwalled carbon nanotube-fused silica composites. Applied physics letters, 87(12), 123103.
31. Al-Hilli, M. F., Li, S., and Kassim, K. S. (2009). Microstructure, electrical properties and Hall coefficient of europium-doped Li–Ni ferrites. Materials Science and Engineering: B, 158(1), 1-6.
32. Ravinder, D., and Kumar, K. V. (2001). Dielectric behaviour of erbium substituted Mn-Zn ferrites. Bulletin of Materials Science, 24(5), 505-509.
33. Rezlescu, N., Rezlescu, E., Tudorache, F. and Popa, P. D. (2004). MgCu nanocrystalline ceramic with La^{3+} and Y^{3+} ionic substitutions used as humidity sensor. J. Optoelectron. Adv. Mater, 6, 695.

34. Jiang, J., Li, L., Xu, F. and Xie, Y. (2007). Preparation and magnetic properties of Zn–Cu–Cr–Sm ferrite via a rheological phase reaction method. Materials Science and Engineering: B, 137(1), 166-169.
35. Sattar, A. A., El-Sayed, H. M., Agami, W. R. and Ghani, A. A. (2007). Magnetic properties and electrical resistivity of Zr^{4+} substituted Li-Zn Ferrite. Am. J. Appl. Sci, 4(2), 89-93.
36. Jalli, J., Hong, Y. K., Gee, S. H., Bae, S., Lee, J., Sur, J. C., ... and Mewes, T. (2008). Magnetic and Microwave Properties of Sm-Doped SrFe O Single Crystals. Magnetics, IEEE Transactions on, 44(11), 2978-2981.
37. Dwevedi, S., Bharathi, K. K., & Markandeyulu, G. (2009). Magnetoreactance studies in rare earth-doped Ni ferrite. Magnetics, IEEE Transactions on, 45(10), 4253-4256.
38. Roy, P. K. and Bera, J. (2007). Enhancement of the magnetic properties of Ni–Cu–Zn ferrites with the substitution of a small fraction of lanthanum for iron. Materials research bulletin, 42(1), 77-83.
39. Jing, J., Liangchao, L. and Feng, X. (2007). Structural analysis and magnetic properties of Gd-doped Li-Ni ferrites prepared using rheological phase reaction method. Journal of Rare Earths, 25(1), 79-83.
40. Fayek, M. K., Ata-Allah, S. S., Zayed, H. A., Kaiser, M. and Ismail, S. M. (2009). Effect of Zn substitution on relaxation characteristics and dielectric properties of $Cu_{1-x}Zn_xGa_{0.5}Fe_{1.5}O_4$ spinel. Journal of Alloys and Compounds, 469(1), 9-14.
41. Sivakumar, N., Narayanasamy, A., Greneche, J. M., Murugaraj, R. and Lee, Y. S. (2010). Electrical and magnetic behaviour of nanostructured $MgFe_2O_4$ spinel ferrite. Journal of Alloys and Compounds, 504(2), 395-402.
42. Kaiser, M. (2009). Effect of nickel substitutions on some properties of Cu–Zn ferrites. Journal of Alloys and Compounds, 468(1), 15-21.
43. Reddy, M. P., Madhuri, W., Reddy, N. R., Kumar, K. S., Murthy, V. R. K. and Reddy, R. R. (2010). Influence of copper substitution on magnetic and electrical properties of MgCuZn ferrite prepared by microwave sintering method. Materials Science and Engineering: C, 30(8), 1094-1099.

44. Ahmed, M. A., El Nimr, M. K., Tawfik, A. and El Hasab, A. M. (1991). Dielectric behaviour in Ni-Al ferrites at low frequencies. Journal of magnetism and magnetic materials, 98(1), 33-36.
45. Ata-Allah, S. S. and Fayek, M. K. (2000). Mössbauer effect study of $Ni_{1-x}Cu_xMn_yFe_{2-y}O_4$ system. Hyperfine Interactions, 128(4), 467-479.
46. Mazen, S. A., Mansour, S. F., Dhahri, E., Zaki, H. M. and Elmosalami, T. A. (2009). The infrared absorption and dielectric properties of Li–Ga ferrite. Journal of Alloys and Compounds, 470(1), 294-300.
47. Hashim, M., Kumar, S., Koo, B. H., Shirsath, S. E., Mohammed, E. M., Shah, J., ... and Kumar, R. (2012). Structural, electrical and magnetic properties of Co–Cu ferrite nanoparticles. Journal of Alloys and Compounds, 518, 11-18.
48. Gabal, M. A. (2010). Structural and magnetic properties of nano-sized Cu–Cr ferrites prepared through a simple method using egg white. Materials Letters, 64(17), 1887-1890.
49. Hsu, J. Y., Lin, H. C., Shen, H. D. and Chen, C. J. (1997). High frequency multilayer chip inductors. Magnetics, IEEE Transactions on, 33(5), 3325-3327.
50. Miao, C., Zhou, J., Cui, X., Wang, X., Yue, Z. and Li, L. (2006). Cofiring behavior and interfacial structure of NiCuZn ferrite/PMN ferroelectrics composites for multilayer LC filters. Materials Science and Engineering: B, 127(1), 1-5.
51. Yan, M. and Hu, J. (2006). Microwave sintering of high-permeability ($Ni_{0.20}Zn_{0.60}Cu_{0.20}$) $Fe_{1.98}O_4$ ferrite at low sintering temperatures. Journal of magnetism and magnetic materials, 305(1), 171-176.
52. Costa, A. C. F., Morelli, M. R. and Kiminami, R. H. (2004). Combustion synthesis, sintering and magnetical properties of nanocristalline Ni-Zn ferrites doped with samarium. Journal of materials science, 39(5), 1773-1778.
53. Sattar, A. A., Wafik, A. H., El-Shokrofy, K. M. and El-Tabby, M. M. (1999). Magnetic properties of Cu–Zn ferrites doped with rare earth oxides. physica status solidi (a), 171(2), 563-569.
54. Sun, J., Li, J. and Sun, G. (2002). Effects of La_2O_3 and Gd_2O_3 on some properties of Ni–Zn ferrite. Journal of magnetism and magnetic materials, 250, 20-24.

55. Lee, D., Kim, M. G., Ryu, S., Jang, H. M. and Lee, S. G. (2005). Epitaxially grown La-modified $BiFeO_3$ magnetoferroelectric thin films. Applied Physics Letters, 86(22), 222903.
56. Ederer, C. and Spaldin, N. A. (2005). Weak ferromagnetism and magnetoelectric coupling in bismuth ferrite. Physical Review B, 71(6), 060401.
57. Zhong, Y., Hu, G. and Tang, T. A. (2003). Preparation and ferroelectric properties of lanthanum modified $Sr_{0.8}Bi_{2.2}Ta_2O_9$ thin films. Japanese journal of applied physics, 42(12R), 7424.
58. Sosnowska, I., Schäfer, W., Kockelmann, W., Andersen, K. H. and Troyanchuk, I. O. (2002). Crystal structure and spiral magnetic ordering of BiFeO3 doped with manganese. Applied Physics A, 74(1), s1040-s1042.
59. Shenker, H. (1957). Magnetic anisotropy of cobalt ferrite ($Co_{1.01}Fe_{2.00}O_{3.62}$) and nickel cobalt ferrite ($Ni_{0.72}Fe_{0.20}Co_{0.08}Fe_2O_4$). Physical Review, 107(5), 1246.
60. Walker, M., Mayo, P. I., O'Grady, K., Charles, S. W. and Chantrell, R. W. (1993). The magnetic properties of single-domain particles with cubic anisotropy. I. Hysteresis loops. Journal of Physics: Condensed Matter, 5(17), 2779-2792.
61. Chikazumi, S. (1997). Physics of Ferromagnetism (Vol. 94). New York: Oxford University Press.
62. Zhang, X., Sui, Y., Wang, X., Mao, J., Zhu, R., Wang, Y., ... and Liu, W. (2011). Multiferroic and magnetoelectric properties of single-phase $Bi_{0.85}La_{0.1}Ho_{0.05}FeO_3$ ceramics. Journal of Alloys and Compounds, 509(19), 5908-5912.
63. Bhowmik, R. N. and Ranganathan, R. (2001). Magnetic properties in rare-earth substituted spinel $Co_{0.2}Zn_{0.8}Fe_{2-x}RE_xO_4$ (RE= Dy, Ho and Er, x= 0.05). Journal of alloys and compounds, 326(1), 128-131.
64. Upadhyay, R. V., Gupta, A., Sudakar, C., Rao, K. V., Parekh, K., Desai, R. and Mehta, R. V. (2006). Effect of rare-earth Ho ion substitution on magnetic properties of Fe3O4 magnetic fluids. Journal of Applied Physics, 99(8), 08M906.

65. Stange, M., Lindén, J., Kjekshus, A., Binsted, N., Weller, M. T., Hauback, B. C. and Fjellvåg, H. (2003). Structural aspects of $Pr_{1-x}Sr_xFeO^{3-}$ w.Journal of Solid State Chemistry, 173(1), 148-163.
66. Wu, Y., Huang, Y., Niu, L., Zhang, Y., Li, Y. and Wang, X. (2012). Pr^{3+} substituted W-type barium ferrite: Preparation and electromagnetic properties. Journal of Magnetism and Magnetic Materials, 324(4), 616-621.
67. Costa, A. C. F. M., Tortella, E., Morelli, M. R. and Kiminami, R. H. G. A. (2003). Synthesis, microstructure and magnetic properties of Ni–Zn ferrites.Journal of magnetism and magnetic materials, 256(1), 174-182.
68. Fu, Y. P. and Lin, C. H. (2002). Microwave-induced combustion synthesis of Ni–Zn ferrite powder and its characterization. Journal of magnetism and magnetic materials, 251(1), 74-79.
69. Lee, J. H., Kim, C. K., Katoh, S. and Murakami, R. (2001). Microwave-hydrothermal versus conventional hydrothermal preparation of Ni-and Zn-ferrite powders. Journal of Alloys and Compounds, 325(1), 276-280.
70. Jiang, J., Yang, Y. M. and Li, L. C. (2007). Synthesis and magnetic properties of lanthanum-substituted lithium–nickel ferrites via a soft chemistry route. Physica B: Condensed Matter, 399(2), 105-108.
71. Verma, A., Goel, T. C., Mendiratta, R. G. and Alam, M. I. (1999). Dielectric properties of NiZn ferrites prepared by the citrate precursor method. Materials Science and Engineering: B, 60(2), 156-162.
72. Adams, D. M. (1974). An introduction to concepts in solid-state structural chemistry. Inorganic Solids, John Wiley & Sons, London.
73. Smyth, D. M. (2000). The defect chemistry of metal oxides. New York: Oxford University Press.
74. King, R. J. (2004). Minerals explained 40: The spinels. Geology Today, 20(5), 194-200.
75. Sickafus, K. E., Wills, J. M. and Grimes, N. W. (1999). Structure of spinel. Journal of the American Ceramic Society, 82(12), 3279-3292.
76. Viswanathan, B. and Murty,V.R.K.(1990).; Ferrite Material Science and Technology. New Delhi: Narosa Publishing House

77. Weiss, P. (1907). L'hypothèse du champ moléculaire et la propriété ferromagnétique. J. Phys. Theor. Appl., 6(1), 661-690.
78. Néel, L. (1955). Some theoretical aspects of rock-magnetism. Advances in physics, 4(14), 191-243.
79. Srivastava, C. M., Patni, M. J. and Srinivasan, T. T. (1982). Effect of a Jahn-Teller ion on the ground states of Fe^{2+} and Ni^{2+} ions in spinel ferrites. Journal of Applied Physics, 53(3), 2107-2109.
80. Alpr, A.M. (1971).High temperature oxides (25). New York: Academic press.
81. Standley,K, J,(1962). Oxide Magnetic Materials. London: Oxford University Press,
82. Craik, D. J. (Eds). (1975). Magnetic oxides. New York: John Wiley and Sons
83. Gorter, E.W. (1954). Philips Res. Rep..9, 295
84. Waldron, R. D. (1955). Infrared spectra of ferrites. Physical Review, 99(6), 1727.
85. Foner, S. (1959). Versatile and Sensitive Vibrating-Sample Magnetometer. Review of Scientific Instruments, 30(7), 548-557.
86. Shirsath, S. E., Kadam, R., Mane, M., Ghasemi, A., Yasukawa, Y., Liu, X. and Morisako, A. (2013). Permeability and magnetic interactions in Co^{2+} substituted $Li_{0.5}Fe_{2.5}O_4$ alloys. Journal of Alloys and Compounds, 575, 145-151.
87. Rezlescu, N. and Rezlescu, E. (1993). The influence of Fe substitutions by R ions in a Ni□ Zn Ferrite. Solid state communications, 88(2), 139-141.
88. Kahn, M. L. and Zhang, Z. J. (2001). Synthesis and magnetic properties of $CoFe_2O_4$ spinel ferrite nanoparticles doped with lanthanide ions. Applied Physics Letters, 78(23), 3651-3653. doi: doi:http://dx.doi.org/10.1063/1.1377621
89. Panda, R. N., Shih, J. C. and Chin, T. S. (2003). Magnetic properties of nano-crystalline Gd-or Pr-substituted $CoFe_2O_4$ synthesized by the citrate precursor technique. Journal of magnetism and magnetic materials, 257(1), 79-86.
90. Zhao, L., Cui, Y., Yang, H., Yu, L., Jin, W. and Feng, S. (2006). The magnetic properties of $Ni_{0.7}Mn_{0.3}Gd_xFe_{2-x}O_4$ ferrite. Materials Letters, 60(1), 104-108.

91. Shirsath, S. E., Kadam, R. H., Patange, S. M., Mane, M. L., Ghasemi, A. and Morisako, A. (2012). Enhanced magnetic properties of Dy^{3+} substituted Ni-Cu-Zn ferrite nanoparticles. Applied Physics Letters, 100(4), 042407.
92. Tahar, L. B., Artus, M., Ammar, S., Smiri, L. S., Herbst, F., Vaulay, M. J., ... and Fievet, F. (2008). Magnetic properties of $CoFe_{1.9}RE_{0.1}O_4$ nanoparticles (RE= La, Ce, Nd, Sm, Eu, Gd, Tb, Ho) prepared in polyol. Journal of Magnetism and Magnetic Materials, 320(23), 3242-3250.
93. Toniolo, J. C., Lima, M. D., Takimi, A. S. and Bergmann, C. P. (2005). Synthesis of alumina powders by the glycine–nitrate combustion process. Materials research bulletin, 40(3), 561-571.
94. Vasanthi, V., Shanmugavani, A., Sanjeeviraja, C. and Selvan, R. K. (2012). Microwave assisted combustion synthesis of $CdFe_2O_4$: Magnetic and electrical properties. Journal of Magnetism and Magnetic Materials, 324(13), 2100-2107.
95. Lohar, K. S., Patange, S. M., Mane, M. L. and Shirsath, S. E. (2013). Cation distribution investigation and characterizations of $Ni_{1-x}Cd_xFe_2O_4$ nanoparticles synthesized by citrate gel process. Journal of Molecular Structure, 1032, 105-110.
96. Mane, D. R., Patil, S., Birajdar, D. D., Kadam, A. B., Shirsath, S. E. and Kadam, R. H. (2011). Sol–gel synthesis of Cr^{3+} substituted $Li_{0.5}Fe_{2.5}O_4$: Cation distribution, structural and magnetic properties. Materials Chemistry and Physics, 126(3), 755-760.
97. Ateia, E., Ahmed, M. A. and El-Aziz, A. K. (2007). Effect of rare earth radius and concentration on the structural and transport properties of doped Mn–Zn ferrite. Journal of magnetism and magnetic materials, 311(2), 545-554.
98. Bharathi, K. K., Markandeyulu, G. and Ramana, C. V. (2010). Structural, magnetic, electrical, and magnetoelectric properties of Sm-and Ho-substituted nickel ferrites. The Journal of Physical Chemistry C, 115(2), 554-560.
99. Cullity, B. D. (1959). Elements of X-Ray Diffraction. London: Addison-Wesley Publishing Company.
100. Chaudhari, V., Shirsath, S. E., Mane, M. L., Kadam, R. H., Shelke, S. B. and Mane, D. R. (2013). Crystallographic, magnetic and electrical properties of

$Ni_{0.5}Cu_{0.25}Zn_{0.25}La_xFe_{2-x}O_4$ nanoparticles fabricated by sol–gel method. Journal of Alloys and Compounds, 549, 213-220.

101. Weil, L., Bertaut, F. and Bochirol, L. (1950). Propriétés magnétiques et structure de la phase quadratique du ferrite de cuivre. Journal de Physique et le Radium, 11(5), 208-212.

102. Kumar, L. and Kar, M. (2012). Effect of La 3+ substitution on the structural and magnetocrystalline anisotropy of nanocrystalline cobalt ferrite ($CoFe_{2-x}La_xO_4$). Ceramics International, 38(6), 4771-4782.

103. Standley, K. J. (1972). Oxide magnetic materials: Clarendon Press.

104. Fagherazzi, G. and Garbassi, F. (1972). X-ray diffraction measurements of the cation distributions in spinel structures. Journal of Applied Crystallography, 5(1), 18-23.

105. Valenzuela, R. (1994).Magnetic ceramics. New York: Cambridge university press.

106. Hemeda, O. (2004). Structural and Magnetic Properties of $Co_{0.6}ZnN_{0.4}Mn_xFe_{2-x}O_4$. Turkish Journal of Physics, 28(2), 121-132.

107. Néel, L. (1948). Ann. Phys. Paris, (3).137.

108. Ounnunkad, S. (2006). Improving magnetic properties of barium hexaferrites by La or Pr substitution. Solid state communications, 138(9), 472-475.

109. Muthuselvam, I. P. and Bhowmik, R. N. (2010). Mechanical alloyed Ho^{3+} doping in $CoFe_2O_4$ spinel ferrite and understanding of magnetic nanodomains. Journal of Magnetism and Magnetic Materials, 322(7), 767-776.

110. Maaz, K., Mumtaz, A., Hasanain, S. K. and Ceylan, A. (2007). Synthesis and magnetic properties of cobalt ferrite ($CoFe_2O_4$) nanoparticles prepared by wet chemical route. Journal of Magnetism and Magnetic Materials, 308(2), 289-295.

111. Ali, I., Islam, M. U., Ishaque, M., Khan, H. M., Ashiq, M. N. and Rana, M. U. (2012). Structural and magnetic properties of holmium substituted cobalt ferrites synthesized by chemical co-precipitation method. Journal of Magnetism and Magnetic Materials, 324(22), 3773-3777.

112. Aen, F., Niazi, S. B., Islam, M. U., Ahmad, M. and Rana, M. U. (2011). Effect of holmium on the magnetic and electrical properties of barium based W-type hexagonal ferrites. Ceramics International, 37(6), 1725-1729.

113. Roy, P. K., Nayak, B. B. and Bera, J. (2008). Study on electro-magnetic properties of La substituted Ni–Cu–Zn ferrite synthesized by auto-combustion method. Journal of Magnetism and Magnetic Materials, 320(6), 1128-1132.

114. Shirsath, S. E., Kadam, R. H., Gaikwad, A. S., Ghasemi, A. and Morisako, A. (2011). Effect of sintering temperature and the particle size on the structural and magnetic properties of nanocrystalline $Li_{0.5}Fe_{2.5}O_4$. Journal of Magnetism and Magnetic Materials, 323(23), 3104-3108.

115. Cheng, F.-X., Jia, J.-T., Xu, Z.-G., Zhou, B., Liao, C.-S., Yan, C.-H., . . . Zhao, H.-B. (1999). Microstructure, magnetic, and magneto-optical properties of chemical synthesized Co–RE (RE=Ho, Er, Tm, Yb, Lu) ferrite nanocrystalline films. Journal of Applied Physics, (5), 2727-2732.

116. Sodaee, T., Ghasemi, A., Paimozd, E., Paesano, A. and Morisako, A. (2013). The role of terbium cation substitution on the magnetic properties of cobalt ferrite nanoparticles. Journal of Magnetism and Magnetic Materials, 330, 169-173.

117. Mathew, D. S. and Juang, R. S. (2007). An overview of the structure and magnetism of spinel ferrite nanoparticles and their synthesis in microemulsions. Chemical Engineering Journal, 129(1), 51-65.

118. Liu, X., Zhong, W., Yang, S., Yu, Z., Gu, B. and Du, Y. (2002). Influences of La^{3+} substitution on the structure and magnetic properties of M-type strontium ferrites. Journal of Magnetism and Magnetic Materials, 238(2), 207-214.

119. Lechevallier, L., Le Breton, J. M., Wang, J. F. and Harris, I. R. (2004). Structural analysis of hydrothermally synthesized $Sr_{1-x}Sm_xFe_{12}O_{19}$ hexagonal ferrites. Journal of magnetism and magnetic materials, 269(2), 192-196.

120. Shirsath, S. E., Kadam, R. H., Patange, S. M., Mane, M. L., Ghasemi, A. and Morisako, A. (2012). Enhanced magnetic properties of Dy^{3+} substituted Ni-Cu-Zn ferrite nanoparticles. Applied Physics Letters, 100(4), 042407.

121. Šepelák, V., Schultze, D., Krumeich, F., Steinike, U. and Becker, K. D. (2001). Mechanically induced cation redistribution in magnesium ferrite and its thermal stability. Solid State Ionics, 141, 677-682.

122. Köseoğlu, Y., Baykal, A., Gözüak, F. and Kavas, H. (2009). Structural and magnetic properties of $Co_xZn_{1-x}Fe_2O_4$ nanocrystals synthesized by microwave method. Polyhedron, 28(14), 2887-2892.

123. Wu, Y., Huang, Y., Niu, L., Zhang, Y., Li, Y. and Wang, X. (2012). Pr^{3+}-substituted W-type barium ferrite: Preparation and electromagnetic properties. Journal of Magnetism and Magnetic Materials, 324(4), 616-621.

124. Wang, J. F., Ponton, C. B. and Harris, I. R. (2005). A study of Pr-substituted strontium hexaferrite by hydrothermal synthesis. Journal of alloys and compounds, 403(1), 104-109.

125. Iqbal, M. J. and Farooq, S. (2010). Impact of Pr–Ni substitution on the electrical and magnetic properties of chemically derived nanosized strontium–barium hexaferrites. Journal of Alloys and Compounds, 505(2), 560-567.

126. Cullity,B.D. and Stock, S.R.(2001).Elements of X-ray diffraction.(3rd Ed.).New Jersey: Prentice Hall.

127. Smallman, R. E. (1985). Modern Physical Metallurgy.(4th Ed.).84. London: Butterworth

128. Shirsath, S. E., Kadam, R. H., Mane, M. L., Ghasemi, A., Yasukawa, Y., Liu, X. and Morisako, A. (2013). Permeability and magnetic interactions in Co^{2+} substituted $Li_{0.5}Fe_{2.5}O_4$ alloys. Journal of Alloys and Compounds, 575, 145-151.

129. Standley, K. J. (1972). Oxide magnetic materials. Oxford University Press.

130. Potakova, V. A., Zverev, N. D. and Romanov, V. P. (1972). On the cation distribution in $Ni_{1-x-y}Fe_x^{2+}Zn_yFe_2^{3+}O_4$ spinel ferrites. physica status solidi (a), 12(2), 623-627.

131. Singh, C., Narang, S. B., Hudiara, I. S., Bai, Y. and Tabatabaei, F. (2008). Static magnetic properties of Co and Ru substituted Ba–Sr ferrite. Materials Research Bulletin, 43(1), 176-184.

132. Neel, L. (1948). Magnetic properties of ferrites: ferrimagnetism and anti ferromagnetism. Ann. Phys, 3, 137-198.

133. Shirsath, S. E., Jadhav, S. S., Toksha, B. G., Patange, S. M. and Jadhav, K. M. (2011). Influence of Ce^{4+} ions on the structural and magnetic properties of $NiFe_2O_4$. Journal of Applied Physics, 110(1), 013914.

134. Wang, Y., Li, L., Liu, H., Qiu, H. and Xu, F. (2008). Magnetic properties and microstructure of La-substituted BaCr-ferrite powders. Materials Letters, 62(14), 2060-2062.

135. Banfi, L., Basso, A., Giardini, L., Riva, R., Rocca, V. and Guanti, G. (2011). Tandem Ugi MCR/Mitsunobu Cyclization as a Short, Protecting-Group-Free Route to Benzoxazinones with Four Diversity Points. European Journal of Organic Chemistry, 2011(1), 100-109.

136. Ma, N., Jiang, B., Zhang, G., Tu, S. J., Wever, W. and Li, G. (2010). New multicomponent domino reactions (MDRs) in water: highly chemo-, regio-and stereoselective synthesis of spiro {[1, 3] dioxanopyridine}-4, 6-diones and pyrazolo [3, 4-b] pyridines. Green Chemistry, 12(8), 1357-1361.

137. Le Floch, C., Le Gall, E., Léonel, E., Koubaa, J., Martens, T. and Retailleau, P. (2010). A Cobalt-Catalyzed Multicomponent Approach to Novel 2, 3-Di-and 2, 2, 3-Trisubstituted 3-Methoxycarbonyl-γ-butyrolactones. European Journal of Organic Chemistry, 2010(27), 5279-5286.

138. Haurena, C., Le Gall, E., Sengmany, S., Martens, T. and Troupel, M. (2010). A Straightforward three-component synthesis of α-amino esters containing a phenylalanine or a phenylglycine scaffold. The Journal of organic chemistry, 75(8), 2645-2650.

139. Adib, M., Sheikhi, E., Kavoosi, A. and Bijanzadeh, H. R. (2010). Synthesis of 2-(alkylamino)-5-{alkyl [(2-oxo-2H-chromen-3-yl) carbonyl] amino}-3, 4-furandicarboxylates using a multi-component reaction in water. Tetrahedron,66(47), 9263-9269.

140. Chen, W. B., Wu, Z. J., Pei, Q. L., Cun, L. F., Zhang, X. M. and Yuan, W. C. (2010). Highly enantioselective construction of spiro [4H-pyran-3, 3′-oxindoles] through a domino knoevenagel/Michael/Cyclization sequence catalyzed by cupreine. Organic letters, 12(14), 3132-3135.

141. Singh, M. S. and Chowdhury, S. (2012). Recent developments in solvent-free multicomponent reactions: a perfect synergy for eco-compatible organic synthesis. RSC Advances, 2(11), 4547-4592.

142. Heeres, J., Backx, L. J. J., Mostmans, J. H. and Van Cutsem, J. (1979). Antimycotic imidazoles. Part 4. Synthesis and antifungal activity of ketoconazole, a new potent orally active broad-spectrum antifungal agent.Journal of medicinal chemistry, 22(8), 1003-1005.

143. Hunkeler, W. (1981). Selective antagonists of benzodiazepines. Nature, 290, 514-516.

144. Brimblecombe, R. W., Duncan, W. A. M., Durant, G. J., Emmett, J. C., Ganellin, C. R. and Parsons, M. E. (1975). Cimetidine—a non-thiourea H2-receptor antagonist. Journal of International Medical Research, 3(2), 86-92.

145. Tanigawara, Y., Aoyama, N., Kita, T., Shirakawa, K., Komada, F., Kasuga, M., & Okumura, K. (1999). CYP2C19 genotype–related efficacy of omeprazole for the treatment of infection caused by Helicobacter pylori. Clinical Pharmacology & Therapeutics, 66(5), 528-534.

146. Wauquier, A., Van Den Broeck, W. A. E., Verheyen, J. L. and Janssen, P. A. J. (1978). Electroencephalographic study of the short-acting hypnotics etomidate and methohexital in dogs. European journal of pharmacology, 47(4), 367-377.

147. Bourissou, D. Guerret, O. Ggabbai, F.T. and Bertrand, G. (2000). Chem. Rev. 100.

148. Liebl, R. Randte, R. Mildenberger, H. Bauer, K. and Bieringer, H. (1987) Chem. Abstr. (108)6018.

149. Pozherskii, A.F. Soldatenkov, A.T. and Katritzky, A.Y. (1997). Heterocycles in Life and Society.(p.179). New York: Wiley.

150. Lombardino, J. G., & Wiseman, E. H. (1974). Preparation and antiinflammatory activity of some nonacidic trisubstituted imidazoles.Journal of medicinal chemistry, 17(11), 1182-1188.

151. Phillips, A.P.White, H.L. and Rosen, S. (1983). Chem. Abstr. (Vol.98 P. 53894z.).

152. Satoru, Chem. Abstr. (1989). Vol.111 P. 214482.

153. Katritzky, A.R. Rees, C.W. (Eds). (1984). In Comprehensive Heterocyclic Chemistry. (5)p. 457. New York: Pergamon.

154. Katritzky, A.R. Rees, C.W. (Eds). (1996). In Comprehensive Heterocyclic Chemistry. (3) p. 77. New York: Pergamon.

155. Balalaie, S., Arabanian, A. and Hashtroudi, M. S. (2000). Zeolite HY and Silica Gel as New and Efficient Heterogenous Catalysts for the Synthesis of Triarylimidazoles under Microwave Irradiation. Monatshefte für Chemie / Chemical Monthly, 131(9), 945-948. doi: 10.1007/s007060070049

156. Radziszewski, B. (1882). Ueber die Constitution des Lophins und verwandter Verbindungen. Berichte der deutschen chemischen Gesellschaft, 15(2), 1493-1496.

157. Japp, F. R. and Robinson, H. H. (1882). Constitution des Lophins und des Amarins. Berichte der deutschen chemischen Gesellschaft, 15(1), 1268-1270.

158. Li, B., Chiu, C. K. F., Hank, R. F., Murry, J., Roth, J. and Tobiassen, H. (2002). An optimized process for formation of 2, 4-disubstituted imidazoles from condensation of amidines and α-haloketones. Organic process research & development, 6(5), 682-683.

159. Zhang, P. F. and Chen, Z. C. (2001). Hypervalent Iodine in Synthesis 81: A One-Pot Procedure for the Synthesis of 1H-Imidazole Derivatives by Cyclocondensation of Ketones with [Hydroxy (tosyloxy) iodo] benzene and Amidines. Synthesis, 2001(14), 2075-2077.

160. Nagarapu, L., Apuri, S. and Kantevari, S. (2007). Potassium dodecatugstocobaltate trihydrate (K5CoW12O40·3H2O): A mild and efficient reusable catalyst for the one-pot synthesis of 1,2,4,5-tetrasubstituted imidazoles under conventional heating and microwave irradiation. Journal of Molecular Catalysis A: Chemical, 266(1–2), 104-108.

161. DAVIDSON, D., WEISS, M. and JELLING, M. (1937). The action of ammonia on benzil. The Journal of Organic Chemistry, 2(4), 319-327.

162. Roth, M., Damm, W. and Giese, B. (1996). The Curtin-Hammett principle: Stereoselective radical additions to alkenes. Tetrahedron Letters, 37(3), 351-354.

163. . Usyatinsky, A. Y. and Khmelnitsky, Y. L. (2000). Microwave-assisted synthesis of substituted imidazoles on a solid support under solvent-free conditions. Tetrahedron Letters, 41(26), 5031-5034.

164. Wasserman, H. H., Long, Y. O., Zhang, R. and Parr, J. (2002). Alkenyl tricarbonyl derivatives of α-amino acids as trielectrophiles. Formation of heterocyclic-substituted products. Tetrahedron letters, 43(18), 3351-3353.

165. Deprez, P., Guillaume, J., Becker, R., Corbier, A., Didierlaurent, S., Fortin, M., ... and Heckmann, B. (1995). Sulfonylureas and sulfonylcarbamates as new non-tetrazole angiotensin II receptor antagonists. Discovery of a highly potent orally active (Imidazolylbiphenylyl) sulfonylurea (HR 720). Journal of medicinal chemistry, 38(13), 2357-2377.

166. Jammi, S., Sakthivel, S., Rout, L., Mukherjee, T., Mandal, S., Mitra, R., . . . Punniyamurthy, T. (2009). CuO Nanoparticles Catalyzed C−N, C−O, and C−S Cross-Coupling Reactions: Scope and Mechanism. The Journal of Organic Chemistry, 74(5), 1971-1976.

167. a) Pacchioni, G. (2000). Quantum chemistry of oxide surfaces: from CO chemisorption to the identification of the structure and nature of point defects on MgO. Surface Review and Letters, 7(03), 277-306. b) Pachón, L. D., van Maarseveen, J. H., & Rothenberg, G. (2005). Click chemistry: Copper clusters catalyse the cycloaddition of azides with terminal alkynes. Advanced Synthesis & Catalysis, 347(6), 811-815.

168. a) Sangshetti, J. N., Khan, F. A. K., Kute, C. S., Zaheer, Z. and Ahmed, R. Z. (2015). One-pot three-component synthesis of 3-(α-aminobenzyl)-4-hydroxycoumarin derivatives using nanocrystalline TiO2 as reusable catalyst. Russian Journal of Organic Chemistry, 51(1), 69-73. b) Sangshetti, J. N., Khan, F. A. K., Chouthe, R. S., Zaheer, Z. and Ahmed, R. Z. (2015). Water-mediated oxalic acid catalysed one-pot synthesis of 2-(substituted phenyl) phthalazin-1 (2H)-ones. Journal of Taibah University for Science.c) Nikalje, A. P. G., Ghodke, M. S., Khan, F. A. K., & Sangshetti, J. N. (2015). CAN catalyzed one-pot synthesis and docking study of some novel substituted imidazole coupled 1, 2, 4-triazole-5-carboxylic acids as antifungal agents. Chinese Chemical Letters, 26(1), 108-112. d) Sangshetti, J. N., Khan, F. A. K., Chouthe, R. S., Damale, M. G. and Shinde, D. B. (2014).

Synthesis, docking and ADMET prediction of novel 5-((5-substituted-1-H-1, 2, 4-triazol-3-yl) methyl)-4, 5, 6, 7-tetrahydrothieno [3, 2-c] pyridine as antifungal agents. Chinese Chemical Letters, 25(7), 1033-1038.

169. A) Sangshetti, J. N., Kokare, N. D., Kotharkar, S. A. and Shinde, D. B. (2008). ZrOCl 2· 8H 2 O catalyzed one-pot synthesis of 2, 4, 5-triaryl-1H-imidazoles and substituted 1, 4-di (4, 5-diphenylimidazol-yl) benzene. Chinese Chemical Letters, 19(7), 762-766. B) Sangshetti, J. N., Ansari, S. A. M. and Shinde, D. B. (2011). ZrOCl 2· 8H 2 O catalyzed solvent-free synthesis of isobenzofuran-1 (3H)-ones. Chinese Chemical Letters, 22(2), 163-166. C) Sangshetti, J. N., Kokare, N. D. and Shinde, D. B. (2007). Sulfanilic acid catalyzed solvent-free synthesis of 1, 5-benzodiazepine derivatives. Chinese Chemical Letters, 18(11), 1305-1308.

170. A) Weiss, M. and Appel, M. (1948). The catalytic oxidation of benzoin to benzil. Journal of the American Chemical Society, 70(11), 3666-3667. B) McKillop, A., Swann, B. P., Ford, M. E. and Taylor, E. C. (1973). Thallium in organic synthesis. XXXVIII. Oxidation of chalcones, deoxybenzoins, and benzoins with thallium (III) nitrate (TTN). Journal of the American Chemical Society, 95(11), 3641-3645. C) Zhang, G. S., Shi, Q. Z., Chen, M. F. and Cai, K. (1997). Ammonium chlorochromate adsorbed on alumina: a new reagent for the oxidation of alcohols and benzoins to the corresponding carbonyl compounds. Synthetic communications, 27(6), 953-956.

171. Rosien, J. R., Seichter, W. and Mazik, M. (2013). Trimethoxybenzene-and trimethylbenzene-based compounds bearing imidazole, indole and pyrrole groups as recognition units: synthesis and evaluation of the binding properties towards carbohydrates. Organic & biomolecular chemistry, 11(38), 6569-6579.

172. Manka, J. T., Rodriguez, A. L., Morrison, R. D., Venable, D. F., Cho, H. P., Blobaum, A. L., ... and Emmitte, K. A. (2013). Octahydropyrrolo [3, 4-c] pyrrole negative allosteric modulators of mGlu 1. Bioorganic & medicinal chemistry letters, 23(18), 5091-5096.

173. Wang, M. Z., Xu, H., Liu, T. W., Feng, Q., Yu, S. J., Wang, S. H. and Li, Z. M. (2011). Design, synthesis and antifungal activities of novel pyrrole alkaloid analogs. European journal of medicinal chemistry, 46(5), 1463-1472.

174. Yang, Y., Zhang, Q., Zheng, J. and Zhang, S. (2013). Synthesis and characterization of pyrrole-containing microporous polymeric networks.Polymer, 54(13), 3254-3260.

175. Bandyopadhyay, D., Mukherjee, S., Granados, J. C., Short, J. D. and Banik, B. K. (2012). Ultrasound-assisted bismuth nitrate-induced green synthesis of novel pyrrole derivatives and their biological evaluation as anticancer agents. European journal of medicinal chemistry, 50, 209-215.

176. Ma, F. P., Li, P. H., Li, B. L., Mo, L. P., Liu, N., Kang, H. J., ... and Zhang, Z. H. (2013). A recyclable magnetic nanoparticles supported antimony catalyst for the synthesis of N-substituted pyrroles in water. Applied Catalysis A: General, 457, 34-41.

177. Bharate, J. B., Sharma, R., Aravinda, S., Gupta, V. K., Singh, B., Bharate, S. B. and Vishwakarma, R. A. (2013). Montmorillonite clay catalyzed synthesis of functionalized pyrroles through domino four-component coupling of amines, aldehydes, 1, 3-dicarbonyl compounds and nitroalkanes. RSC Advances, 3(44), 21736-21742.

178. Madabhushi, S., Vangipuram, V. S., Mallu, K. K. R., Chinthala, N. and Beeram, C. R. (2012). Europium (III) Triflate- Catalyzed Trofimov Synthesis of Polyfunctionalized Pyrroles. Advanced Synthesis & Catalysis, 354(8), 1413-1416.

179. Pacchioni, G. (2000). Quantum chemistry of oxide surfaces: from CO chemisorption to the identification of the structure and nature of point defects on MgO. Surface Review and Letters, 7(03), 277-306.

180. Pachón, L. D., van Maarseveen, J. H. and Rothenberg, G. (2005). Click chemistry: Copper clusters catalyse the cycloaddition of azides with terminal alkynes. Advanced Synthesis & Catalysis, 347(6), 811-815.

181. Sangshetti, J. N., Khan, F. A. K., Kute, C. S., Zaheer, Z. and Ahmed, R. Z. (2015). One-pot three-component synthesis of 3-(α-aminobenzyl)-4-hydroxycoumarin derivatives using nanocrystalline TiO2 as reusable catalyst. Russian Journal of Organic Chemistry, 51(1), 69-73. doi: 10.1134/s107042801501011x

182. Sangshetti, J. N., Kalam Khan, F. A., Chouthe, R. S., Zaheer, Z. and Ahmed, R. Z. (2015). Water-mediated oxalic acid catalysed one-pot synthesis

of 2-(substituted phenyl) phthalazin-1(2H)-ones. Journal of Taibah University for Science, 9(4), 548-554. doi: http://dx.doi.org/10.1016/j.jtusci.2014.12.002

183. Nikalje, A. P. G., Ghodke, M. S., Khan, F. A. K. and Sangshetti, J. N. (2015). CAN catalyzed one-pot synthesis and docking study of some novel substituted imidazole coupled 1, 2, 4-triazole-5-carboxylic acids as antifungal agents. Chinese Chemical Letters, 26(1), 108-112.

184. Zaheer, Z., Khan, F. A. K., Sangshetti, J. N. and Patil, R. H.(2015) Expeditious synthesis, antileishmanial and antioxidant activities of novel 3-substituted-4-hydroxycoumarin derivatives. EXCLI Journal.(Vol.14 pp.935-947).

185. Sangshetti, J. N., Kokare, N. D., Kotharkar, S. A. and Shinde, D. B. (2008). ZrOCl 2· 8H 2 O catalyzed one-pot synthesis of 2, 4, 5-triaryl-1H-imidazoles and substituted 1, 4-di (4, 5-diphenylimidazol-yl) benzene. Chinese Chemical Letters, 19(7), 762-766.

186. Sangshetti, J. N., Kokare, N. D. and Shinde, D. B. (2007). Sulfanilic acid catalyzed solvent-free synthesis of 1, 5-benzodiazepine derivatives. Chinese Chemical Letters, 18(11), 1305-1308.

187. Sangshetti, J. N., Kokare, N. D. and Shinde, D. B. (2009). Efficient one-pot synthesis of quinoxalines in the presence of zinc iodide as catalyst. Russian journal of organic chemistry, 45(7), 1116-1118.

188. Sangshetti, J. N. and Shinde, D. B. (2010). One pot synthesis and SAR of some novel 3-substituted 5, 6-diphenyl-1, 2, 4-triazines as antifungal agents.Bioorganic & medicinal chemistry letters, 20(2), 742-745.

189. Sangshetti, J. N., Ansari, S. A. M. and Shinde, D. B. (2011). $ZrOCl_{2\cdot 8}H_2O$ catalyzed solvent-free synthesis of isobenzofuran-1 (3H)-ones. Chinese Chemical Letters, 22(2), 163-166.

190. Sangshetti, J. N., Khan, F. A. K., Chouthe, R. S., Damale, M. G. and Shinde, D. B. (2014). Synthesis, docking and ADMET prediction of novel 5-((5-substituted-1-H-1, 2, 4-triazol-3-yl) methyl)-4, 5, 6, 7-tetrahydrothieno [3, 2-c] pyridine as antifungal agents. Chinese Chemical Letters, 25(7), 1033-1038.

191. Sangshetti, J. N., Dharmadhikari, P. P., Chouthe, R. S., Fatema, B., Lad, V., Karande, V., ... and Shinde, D. B. (2013). Microwave assisted nano (ZnO–

TiO_2) catalyzed synthesis of some new 4, 5, 6, 7-tetrahydro-6-((5-substituted-1, 3, 4-oxadiazol-2-yl) methyl) thieno [2, 3-c] pyridine as antimicrobial agents. Bioorganic & medicinal chemistry letters, 23(7), 2250-2253.

192. Li, B. L., Zhang, M., Hu, H. C., Du, X. and Zhang, Z. H. (2014). Nano-$CoFe_2O_4$ supported molybdenum as an efficient and magnetically recoverable catalyst for a one-pot, four-component synthesis of functionalized pyrroles. New Journal of Chemistry, 38(6), 2435-2442.

193. Gupta, N., Singh, K. N. and Singh, J. (2014). Ionic liquid catalyzed one pot four-component coupling reaction for the synthesis of functionalized pyrroles.Journal of Molecular Liquids, 199, 470-473.

194. Li, B. L., Hu, H. C., Mo, L. P. and Zhang, Z. H. (2014). Nano $CoFe_2O_4$ supported antimony (iii) as an efficient and recyclable catalyst for one-pot three-component synthesis of multisubstituted pyrroles. RSC Advances,4(25), 12929-12943.